

COMPLIANT INTERFACES FOR WRINKLE CONTROL AND STRAIN ATTENUATION

BY

KUO-KANG HUNG

DISSERTATION

Submitted in partial fulfillment of the requirements  
for the degree of Doctor of Philosophy in Aerospace Engineering  
in the Graduate College of the  
University of Illinois Urbana-Champaign, 2021

Urbana, Illinois

Doctoral Committee:

Professor Ioannis Chasiotis, Chair and Director of Research  
Professor Huck Beng Chew  
Professor John Lambros  
Professor SungWoo Nam

## ABSTRACT

Microscale interfaces play an important role in the mechanics of material systems with dissimilar properties. In particular, compliant interfaces have been shown to provide resistance to crack propagation or accommodate the differential thermal expansion between dissimilar materials. In this dissertation research, compliant interfaces were taken advantage to address two problems in mechanics: (a) Control the details of surface wrinkling of soft substrates with hard coatings subjected to uniaxial compression, and (b) attenuate or completely eliminate the strain transfer from a load bearing substrate to an attached film.

The first objective of this dissertation research was to investigate the geometry and material properties of a compliant interface that was employed to modify the wrinkle behavior of a material system comprised of a stiff film deposited onto a compliant substrate. In a conventional two-layer system, the wrinkle patterns, as described by their wavelength, amplitude and orientation are determined solely by the material properties and thickness of the two layers and the direction of the applied load. A compliant interface layer can provide the means for further control of wrinkling. Towards this goal, thin films were deposited via Glancing Angle Deposition (GLAD) between an elastomeric substrate of polydimethylsiloxane (PDMS) and a Cu thin film. The process parameters of GLAD were studied and calibrated to fabricate films comprised of uniform isotropic (nanosprings) and orthotropic (nanochevrons) Cu nanostructures with different geometrical parameters that controlled the effective in-plane compressive modulus of the GLAD films. The highly compliant Cu nanospring films served as novel means to reduce the physical length scale of wrinkle patterns, i.e. concurrently reduce the wrinkle wavelength and amplitude while maintaining the wrinkle amplitude-to-wavelength aspect ratio for a given applied strain. On the other hand, anisotropic Cu films comprised of nanochevrons with 0.5- $\mu\text{m}$  pitch were shown to exhibit an anisotropy ratio of 9.3 which modified the wrinkle direction with respect to the principal stress direction by almost  $10^\circ$ . Thus, contrary to isotropic films in which the direction of applied stress exclusively dictates the wrinkle direction, this unique class of anisotropic films allowed modifying, for the first time, the wrinkle direction independently of the direction of the applied load.

Thus, a compliant interface could be used quite effectively to control the geometrical details of wrinkle patterns without modifying the original material system or the type of loading. Finally, the mechanics of surface wrinkling was taken advantage to obtain for the first time the effective in-plane compressive modulus of GLAD films, as their discrete nature prevented such measurements in the past. The in-plane compressive modulus of GLAD Cu films comprised of nanosprings with 0.25- $\mu\text{m}$  and 0.5- $\mu\text{m}$  pitch was measured as  $500\pm 21$  MPa and  $830\pm 20$  MPa, respectively, which is more than two orders of magnitude smaller than the Young's modulus of a solid Cu film (120 MPa). Similarly, the effective in-plane compressive modulus of nanochevron Cu films with 0.5- $\mu\text{m}$  pitch was measured as  $710\pm 10$  MPa and  $75.1\pm 2$  MPa along the principal material axis and its normal, respectively.

The second objective of this dissertation research focused on the attenuation or complete elimination of strain transfer from a load bearing substrate to an attached film via a compliant interface. Brittle films such as thin film photovoltaics (PV) that are integrated with load-bearing structures can fragment and suffer from performance degradation while subjected to strains larger than 0.3%. A properly designed interface can shield a brittle PV film from structural loads while also maintaining its functional performance. The design of effective (reaching 100% strain attenuation) and efficient (minimum layer thickness to attain 100% strain attenuation) interface layers depends on the dimensions and mechanical properties of the substrate, the PV film and the interface layer. An analytical elasticity model captured the coupled effects of shear modulus and thickness of a compliant interface on the attenuation of strain transferred from a Carbon Fiber Reinforced Polymer (CFRP) laminate to a bonded PV film. Based on the results of this model, a series of experiments were designed and carried out by using PDMS interface layers with effective shear stiffness values (shear modulus over thickness) in the range of 0.6-48 MPa/mm, leading to 36-100% strain attenuation. After accounting for manufacturing effects on the effective modulus of the PDMS interface layers, a very good agreement emerged between the experimental measurements and the model predictions. Importantly, the strain attenuation achieved by the interface layer preserved the original fill factor of the PV film until CFRP laminate failure at 1.8% strain, whereas,

in the absence of a PDMS interface, the fill factor gradually decreased when the CFRP laminate strain exceeded 0.8%. Based on the experimentally validated analytical model, general strain attenuation maps were drawn to capture the coupled effects of the effective shear stiffness of an interface layer, and the Young's modulus, thickness and length of an attached film.

## ACKNOWLEDGEMENTS

The work in this dissertation would not have been possible without the support and encouragement of my coworkers, my adviser and finally my family. Their constant support and encouragement provided me with the necessary tools for the completion of my doctorate program and I will be always grateful to their kindness.

I would like to express my sincere gratitude to my advisor, Prof. Ioannis Chasiotis, for his constant support and guidance in the successful completion of this dissertation. I cannot express the gratitude I have for him for giving me the very first appointment at the University of Illinois and providing me the opportunity to conduct research in such a unique field. He helped me develop the skill-sets in academic and professional matters. He showed extreme patience and helped me through difficult times during the completion of this dissertation research. I will always be grateful of everything he has done for me. I would also like to acknowledge the Air Force Office of Scientific Research (AFOSR) through grants FA2386-13-1-3015 DURIP, FA9550-15-1-0470, and FA9550-18-1-0258 with Dr. B.L. Lee as the program manager for supporting my research.

I sincerely thank Prof. Huck Beng Chew, Prof. John Lambros, and Prof. SungWoo Nam for agreeing to serve on my doctoral committee and providing invaluable feedback during my preliminary examination that was important to improving this dissertation.

Many thanks are due to all my present and past lab mates from Prof. Chasiotis's research group, especially Dr. Fan Yang, Dr. Debashish Das, Mr. Sean Lee and Mr. Aldo Montagner for their invaluable discussions which have always helped bring in a fresh perspective to the challenges at hand, and Dr. Dimitrios Antartis for training me on the experimental tools and for his insightful discussions.

I would like to thank the Aerospace Department staff for their constant support, especially the machine shop members Mr. Greg Milner and Mr. Lee Booher for their valuable suggestions to improve the design of parts, and Ms. Staci McDannel, Ms.

Kristen Reifsteck, and Mr. Scott Dalbey for help with administrative issues. I extend my thanks to the staff at Material Research Laboratory for training me on several necessary instruments, primarily to Dr. Honghui Zhou for FIB and SEM training, Dr. Julio Soares for confocal microscope training. I also extend my thanks to Dr. Glennys Mensing and Mr. Joe Maduzia at Micro-Nano Mechanical System Cleanroom for training me on several cleanroom instruments, including fabrication and characterization tools. Special thanks to Mr. Scott Dalbey and Mr. Greg Milner for providing me the immediate assistance in all different kinds of emergencies happened in the lab. They not only helped protecting the instruments in the lab but also providing me the sense of security for the operation of the lab.

Finally I am forever grateful to my parents, sister, brother and my relatives for the unconditional love, constant encouragement, support and for believing in me.

# TABLE OF CONTENTS

<b>Introduction.....</b>	<b>1</b>
1.1 Control of Surface Wrinkling .....	2
1.1.1 Background in Glancing Angle Deposition (GLAD).....	5
1.2 Control of Strain Attenuation in Integrated Thin Film Photovoltaics .....	8
1.3 Research Objectives and Approach .....	11
1.3.1 Research Tasks.....	12
1.4 Dissertation Outline .....	13
<b>Experimental Methods .....</b>	<b>15</b>
2.1 Fabrication of Interface Layers for Wrinkle Control.....	15
2.2 Mechanical Testing.....	19
2.3 Measurement of PV Fill Factor.....	21
2.4 Summary .....	23
<b>Control of Wrinkling through Interface Engineering.....</b>	<b>24</b>
3.1 Experimental Methods .....	24
3.1.1 Process Parameters for GLAD Nanostructures.....	24
3.1.2 Deposition of Solid and Nanostructured Interface Layers.....	30
3.2 Analytical Problem Formulation.....	34
3.2.1 Wrinkling of Isotropic Two- and Three-layer Material Systems.....	34
3.2.2 Modeling the Wrinkling Behavior with an Orthotropic Layer .....	38
3.3 Effect of Isotropic Interface Material on Wrinkle Pattern .....	43
3.4 Control of Wrinkling through an Anisotropic Interface .....	50
3.5 Conclusions.....	58
<b>Strain Attenuation via Interface Engineering.....</b>	<b>59</b>
4.1 Analysis and Experimental Methods .....	59
4.1.1 Material Selection and Fabrication .....	59
4.1.2 Analytical Problem Formulation.....	61
4.2 Determination of Layer Properties.....	64

4.3 Determination of Parameter Space for Interface Layer Properties .....	66
4.4 Experimental Evaluation of Strain Attenuation .....	72
4.5 Experimental Results vs. Analytical Model Predictions.....	75
4.6 I-V Characteristic Curves vs. CFRP Laminate Strain.....	77
4.7 Evaluation of Strain Attenuation Methodology .....	80
4.8 Conclusions .....	81
<b>Conclusions.....</b>	<b>82</b>
5.1 Assessment of Dissertation Outcomes.....	82
5.1.1 Control of Wrinkle Pattern through Interface Layers .....	83
5.1.2 Strain Attenuation through an Interface Layer .....	84
5.2 Future Directions.....	85
5.2.1 Control of GLAD Film through Seeding.....	85
5.2.2 Seed Design for GLAD Deposition .....	89
<b>APPENDIX A: Wrinkle Control.....</b>	<b>94</b>
A.1 Mechanical Properties of PDMS Substrate.....	94
A.2 Details of the Wrinkle Problem Formulation.....	95
A.3 Wrinkle Wavelength vs. Applied Strain .....	98
<b>APPENDIX B: Strain Attenuation.....</b>	<b>100</b>
B.1 Derivation of Plane Strain Modulus of the CFRP Laminate.....	100
B.2 Parameters in Stress and Strain Field Solution of Three-layer System.....	103
B.3 Effect of Material System Parameters on Strain Attenuation .....	106
<b>References.....</b>	<b>114</b>

# CHAPTER 1

## Introduction

Interfaces layers play an important role in mechanical, thermal and electrical applications [1-3] by providing enhanced compliance and functional properties such as reduced electrical and thermal contact resistance. From a mechanical viewpoint, compliant interface layers improve the resistance to interfacial cracks and accommodate the differential thermal expansion between materials with different coefficients of thermal expansion. Sumigawa et al. [4,5] employed a 560-nm Ta<sub>2</sub>O<sub>5</sub> nanospring film as a compliant interface layer between two solid bodies. This nanospring interface layer with Young's modulus of 0.37 GPa removed the stress singularity at the interface crack tip. In cases where there was no interface layer, the normal stress was 3.5 times higher near an interface crack tip than the far field. Similarly, carbon nanotubes (CNTs) have been proposed as a thermal interface due to high intrinsic thermal conductivity [3,6]. For instance, compliant interface layers of CNTs with 280- $\mu$ m hair-like structure were grown by Ge et al. [7] with effective modulus of 0.5 MPa. Antartis et al. [1] developed films of 10- $\mu$ m long Cu nanosprings, fabricated by Glancing Angle Deposition (GLAD), as a thermal interface layer with a 500 MPa normal stiffness that accommodated the significantly different coefficients of thermal expansion of Si and Cu while achieving an effective thermal resistance of 0.01 cm<sup>2</sup>K/W.

The classes of compliant interface layers fabricated by GLAD in [1,4,5] were taken advantage of in this dissertation to control wrinkle patterns induced by the mechanical instability taking place in a material system comprised of a stiff film on a compliant substrate. Wrinkle patterns determine the surface morphology that can be important in a variety of applications, such as energy harvesting and surface

hydrophilicity [8,9]. Control of wrinkling can be facilitated by compliant interface layers that modify the wrinkle response of a multi-layer material system subjected to the in-plane compression. In general, compliant interface layers control strain transfer which is utilized in this dissertation to control strain transfer between a brittle functional film that is susceptible to fragmentation [10] and a load-bearing substrate. Attenuation and complete elimination of strain transfer requires a systematic approach to determine the material and thickness of an effective and efficient interface layer, which are discussed in the next Sections of this Chapter. Major fraction of the content of this Chapter and the subsequent Chapter is derived from two publications by this author [11,12].

## 1.1 Control of Surface Wrinkling

Mechanical instabilities take place when a stiff thin film is deposited onto a flexible substrate that is subjected to in-plane compression, forming surface wrinkle patterns to accommodate the elastic strain energy [13-16]. An early study by Bowden et al. [14] demonstrated a variety of wrinkle patterns induced during cyclic heating and cooling of a material system comprised of a metal film on an elastomeric substrate. Following the same rationale, wrinkle patterns, such as stripes and herringbones, have been demonstrated in literature [17-21]. For instance, Lin and Yang [17] reported on one- and two-dimensional (stripes and herringbones) wrinkle patterns by controlling the biaxial loading applied to an oxidized thin surface layer on a polydimethylsiloxane (PDMS) substrate.

Although wrinkle patterns can be undesirable, a variety of applications have taken advantage of the periodic nature of the wrinkling and utilized the aspect ratio of wrinkle amplitude over wavelength in stiff film-flexible substrate systems [8,22-29]. Controlling the wrinkle amplitude-to-wavelength aspect ratio has enabled several applications, such as tunable phase gratings to control light diffraction, modified surface wetting, improved solar cell efficiency and luminous efficiency of organic light emitting diodes (OLEDs), enhanced adhesion of bacteria on surfaces, new classes of flexible electronics, etc. [8,24-32]. For example, Harrison et al. [25] controlled the wrinkle amplitude of a glassy

polymer film on a PDMS substrate for applications to phase gratings. The wrinkle amplitude made the material system act as a tunable phase grating for different light diffraction intensities. In a different study, Zhang et al. [26] demonstrated a transition from surface hydrophilicity to hydrophobicity by increasing the wrinkle amplitude-to-wavelength aspect ratio through the applied strain. Likewise, wrinkling increased the energy harvesting efficiency of solar cells [8,22] and luminous efficiency of organic light emitting diodes (OLEDs) by increasing the aspect ratio of wrinkle amplitude-to-wavelength [29]. Nguyen et al. [27] demonstrated different attachment responses of bacteria on microscale and nanoscale wrinkle patterns by controlling the thickness of a wrinkled film. Kim et al. [32] utilized the wrinkling behavior of CMOS circuits on a PDMS substrate to protect the CMOS circuits from large applied strains which were accommodated by wrinkling. These applications highlight the importance of controlling the parameters of wrinkle patterns, including the wrinkle wavelength, amplitude and orientation. Wrinkle patterns are controlled by the thickness and in-plane elastic moduli of the materials comprising a compliant substrate-stiff film system, as well as the direction and amplitude of the applied compressive strain: It has been shown that the wrinkle wavelength is determined by the thickness and the in-plane modulus of the stiff film, and the in-plane modulus of the compliant substrate [33]. Then, for a given material system, the wrinkle amplitude and orientation can be only controlled by the direction and amplitude of the applied compressive strain. Hence, the physical length scale of a wrinkle pattern, i.e. the scale of the wrinkle wavelength and amplitude, is constrained by a given flexible material system.

To date, only a few works have attempted to control wrinkle patterns [22,34] without varying the applied load. Among them, Guo et al. [22] controlled wrinkling by the effective Poisson's ratio of discontinuous mesh-type films in the range 1-4.5, which resulted in lateral contraction that was much larger than that of the PDMS substrate. By virtue of mesh-type films with different Poisson's ratios, film wrinkling can be initiated at various applied strains leading to a variety of wrinkle patterns. Auguste et al. [34] increased the substrate confinement by making the substrate thickness close to the film thickness, which led to higher wrinkle amplitude-to-wavelength aspect ratios because it delayed the period doubling that occurs when every second wrinkle deepens at the

expense of its neighbors at high applied strains, Figures 1.1(c,d). However, in many applications it may not be possible to modify the material and/or the thickness of the compliant substrate or the top stiff film to control the wrinkle wavelength and/or its direction.

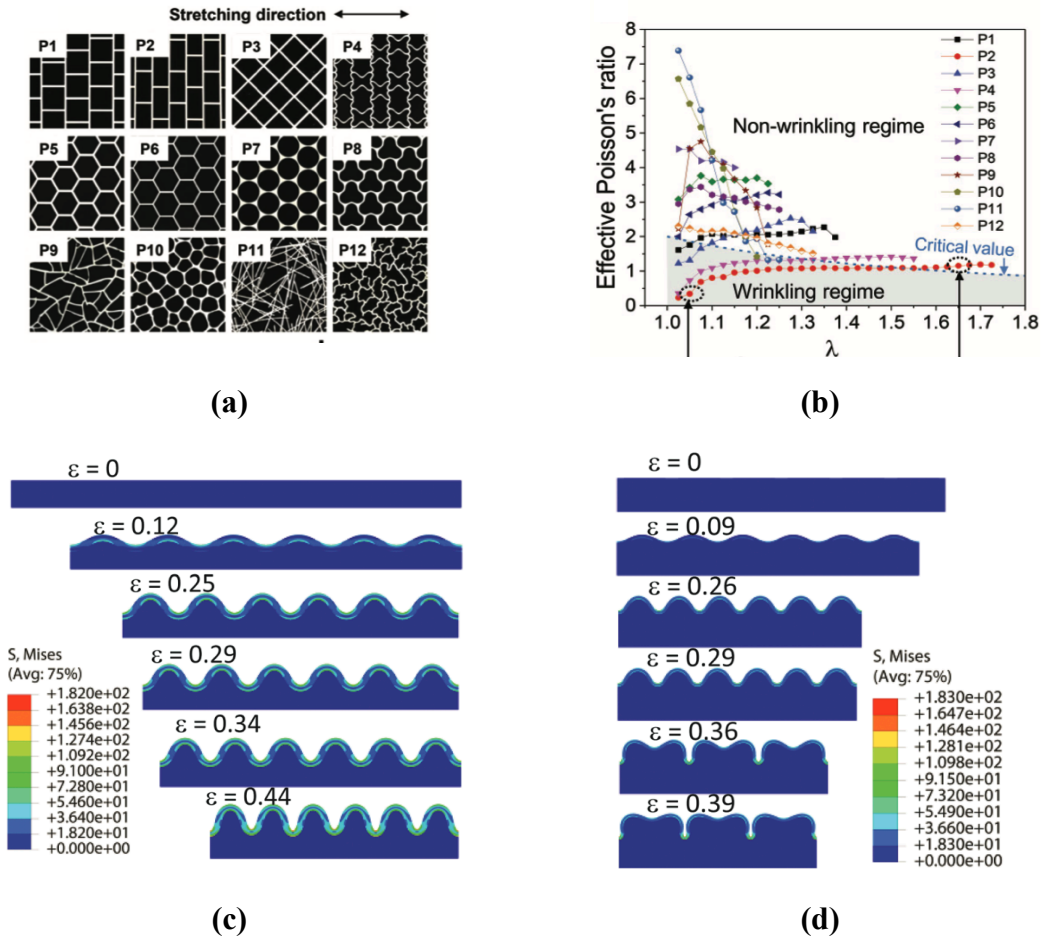


**Figure 1.1** (a) Mesh structures of Au films on PDMS. (b) Effective Poisson's ratio ( $\epsilon_x/\epsilon_y$ ) vs. applied strain with wrinkling regime highlighted [22]. Reprinted with permission from John Wiley and Sons. Cross-sectional views of the evolution of wrinkling to period doubling at different applied strains with substrate/film thickness ratios of (c) 3 and (d) 9 [34]. Reprinted with permission from Royal Society of Chemistry.

To the best of the authors' knowledge, there is no proven approach to control the wrinkle amplitude, wavelength and orientation without modifying the composition or structure of the compliant substrate/stiff film system, and without the application of multiaxial loading. Therefore, viable solutions must be sought in the properties of the interface between the elastomeric substrate and the stiff film. In this dissertation, the geometric characteristics of wrinkling were modified by incorporating a compliant interface layer that reduces the effective stiffness of the top stiff film, while maintaining the electrical and thermal properties of a metal or ceramic top film. Compliant interface layers with different geometrical and mechanical characteristics were fabricated by GLAD, which is discussed in the next Subsection.

### **1.1.1 Background in Glancing Angle Deposition (GLAD)**

GLAD is a technique that extends Oblique Angle Deposition by further controlling the movement of a substrate to control ballistic shadowing [1,2,35-38], Figure 1.2(a). GLAD takes place at the shallow angle of  $\sim 85^\circ$  with respect to the direction of the incident vapor. Atoms arriving at the target surface form small nuclei whose density and size depend on the wetting properties of the vapor with respect to the substrate surface. Once stable nuclei of a finite size form, they have a shadowing effect due to the high incident angle of the vapor, thus halting the growth of small nuclei in their "shadow region", while the larger nuclei continue to grow, Figure 1.2(b). GLAD films have the advantages of low deposition temperature, direct growth onto a substrate, multimaterial deposition and easy integration to the next layer via a continuous capping layer [1,37]. The area coverage is also outstanding, depending on the substrate size that can be accommodated by the deposition system. Through the combination of process parameters, including the deposition angle,  $\alpha$ , the rotation speed,  $\omega$ , and the deposition rate, Figure 1.2(a), a variety of nanostructures, such as nanochevrons, nanosprings, and nanocolumns, can be realized [35], Figure 1.3. The geometrical details of GLAD engineered nanostructures provide control of the film properties: mechanical, optical, thermal, and electrical [2,13,35-42].

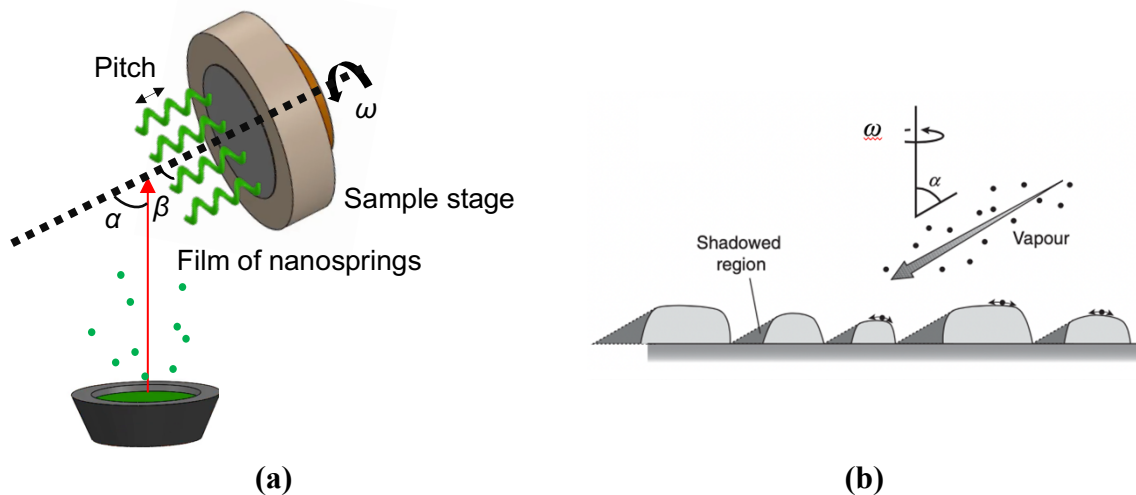


**Figure 1.2** (a) Concept of GLAD showing the deposition angle,  $\alpha$ , and rotation speed,  $w$ , and (b) shadowing effect in GLAD [43]. Reprinted with permission from IEEE.

In terms of optical properties [44,45], Merket et al. fabricated films of Si columns to increase energy harvesting in photovoltaic films. The higher porosity of Si columns increased their surface area for oxidation and led to a smaller open circuit voltage, which, in turn, increased energy harvesting [45]. The higher surface area of GLAD films has been also harnessed for sensing applications. Liu et al. fabricated Pt/WO<sub>3</sub> nanorod films with high sensitivity to NO<sub>2</sub> (80 ppb NO<sub>2</sub> with a response of 1.23), which can potentially be used in NO<sub>2</sub> MEMS sensors [46]. In addition, GLAD films were used in energy storage applications [47]. Broughton and Brett [47] reported Mn nanochevron structures as an electrochemical capacitor with improved specific capacitance, owing to greater porosity.

GLAD films have also been employed as a mechanical material in thermal interfaces [1], compliant films for Li<sup>+</sup> anodes [39,42,48], and layers to avert stress singularity [4,5]. Specifically, Antartis et al. [1] utilized 10- $\mu$ m thick Cu nanospring films as a thermal interface to accommodate the thermal stress due to the mismatch of the coefficients of thermal expansion between a Cu heatsink and a Si substrate. The compliant Cu nanospring film also provided an effective thermal resistance of 0.01 cm<sup>2</sup>K/W. Furthermore, due to their high compliance, individual 10- $\mu$ m long Si GLAD

nanosprings showed no fragmentation during volumetric expansion due to lithiation [39]. Solid Si anodes suffer from fragmentation and delamination due to volumetric expansion [49]. The nanospring structure of GLAD Si anodes also resulted in higher lithiation rates (3.4 nm/s) that were attributed to the nanowire structure of Si nanosprings. Finally, by introducing a Ta<sub>2</sub>O<sub>5</sub> nanospring film between two dissimilar materials, the stress singularity near the crack tip was diminished due to the compliant nanosprings [4,5].

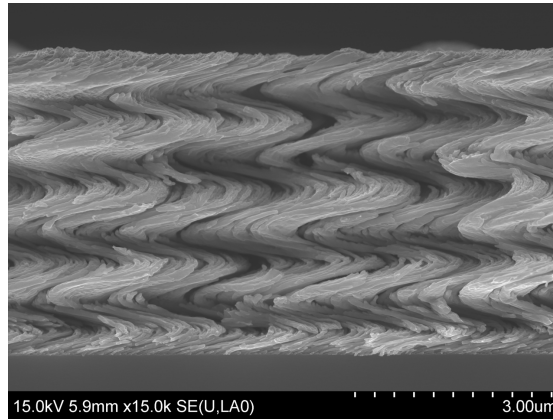


**Figure 1.3** Film of Cu nanosprings with 4-turn coils deposited on a Si substrate.

To employ mechanical GLAD films, it is necessary to understand their mechanical properties. Prior studies on the mechanical properties of nanoarchitected GLAD films focused on the out-of-plane compressive and shear moduli [1,5,50,51]. Using an Atomic Force Microscope (AFM), Sumigawa et al. reported the apparent Young's and shear moduli of Ta<sub>2</sub>O<sub>5</sub> films, comprised of 560 nm thick springs, as 375 MPa and 60 MPa, respectively, [5]. Similarly, by utilizing a nanoindenter, Pique et al. reported the Young's modulus of 10 GPa for TiO<sub>2</sub> films comprised of 1.5 μm tall columns [50]. Antartis et al. [1] studied 10 μm thick Cu nanospring films as a thermal interface material with 250 MPa and 500 MPa shear and normal stiffness, respectively. Antartis et al. [37] also isolated single Si nanosprings and showed that the wire cross-section is elliptical with major and minor axes ~400 μm and 200 μm, respectively. With the aid of MEMS devices, the stiffness of single Si nanosprings was measured to be of

the order of 10 N/m [37]. Kaneko et al. [51] used a nanoprobe to measure the stiffness of 500-nm single Si nanosprings as 4.1 N/m.

Yet, the in-plane compressive modulus of GLAD films, controlled by the interactions between individual nanostructures, is still unknown. The discontinuous nature of GLAD films prevents their removal from the growth substrate and mechanical testing to determine the compressive in-plane modulus. The in-plane film stiffness controls among others the film buckling response and is discussed in the context of surface wrinkling in Chapter 3 of this dissertation.

## **1.2 Control of Strain Attenuation in Integrated Thin Film Photovoltaics**

Flexible thin film photovoltaics (PV) are comprised of brittle thin films such as amorphous Si (aSi). When integrated onto load-bearing systems, such as building structures, aerospace vehicles, satellites, and portable devices [52-58], are subjected to significant mechanical loads [10] as the substrate strain is fully transferred to the brittle film because the effective stiffness of the substrate is orders of magnitude larger than the stiffness of the brittle PV film. In the case of brittle aSi thin film PVs, the mechanical strain imposed through a composite laminate substrate has been shown to lead to progressive damage beyond a threshold strain. Performance has also been shown to degrade when PV films are subjected to relatively small strains [52,59,60], as quantified by the reduction of the fill factor (FF) which is the ratio of maximum power of the PV film to the product of the open circuit voltage with the short circuit current. In this context, Jones et al. [61] reported the onset of the decline of the FF at 0.75% tensile strain, by subjecting a PV film to bending. Antartis and Chasiotis [59] integrated aSi PV films with Carbon Fiber Reinforced Polymer (CFRP) laminates, and showed that a decay of the FF begins at substrate tensile strain of 0.8% for both cross-ply ( $[0^\circ/90^\circ]_n$ ) and  $\pm 45^\circ$  laminates. Progressive fragmentation of the aSi layer was identified as the root cause of the performance degradation of the thin film PV. Notably, the ZnO Transparent Conducting Oxide (TCO) layer was shown to begin fragmenting at CFRP laminate

strains as low as 0.3%, albeit without reduction in FF but with potentially detrimental effects on the environmental stability of the aSi PV modules, Figure 1.4.

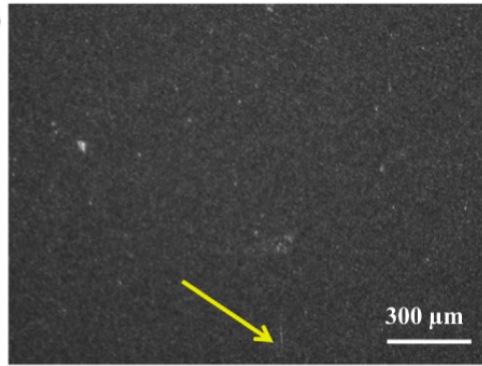


**Figure 1.4** Cracking of TCO ZnO on a PV film, co-cured on a 0° laminate, at a strain of 0.3% [59]. Reprinted with permission from Elsevier.

While several studies have focused on improving the efficiency of PV films [62,63], there has been no systematic study to reduce or eliminate the degradation of the functional performance of aSi PV films due to substrate-induced strain. Recently, Dai et al. [64] studied the effect of adhesive bonding of PV modules onto Glass Fiber Reinforced Polymer (GFRP) laminates by comparing an epoxy with a silicone adhesive. The authors reported no performance degradation up to 0.7% GFRP strain for 0.5-mm and 2.0-mm thick silicone adhesive layers, contrary to an epoxy adhesive of the same thickness that resulted in performance degradation of the PV module at strains equal to 0.62% and 0.23%, respectively. Using a shear lag model and their experimental results the authors in [64] concluded that, for a given PV module, the shear modulus and the thickness of the adhesive control the transfer of the GFRP substrate strain to the PV module. However, the adhesive layer thicknesses utilized by Dai et al. [64] are excessive compared to the thickness of an unencapsulated PV module, therefore a systematic approach is required to determine the minimum required adhesive (interface) layer thickness to isolate a PV module from the substrate strain. Furthermore, Dai et al. [64] tested their aSi PV modules in a very limited range of substrate strains (up to 0.7%) while

prior reports [59,61] have shown almost no performance degradation of aSi thin film PVs subjected to 0.7% strain.

In order to address these gaps in our current capabilities to effectively and efficiently integrate thin film PVs onto load-bearing structures, this dissertation investigated the effects of thickness and mechanical properties of an interface layer on the strain attenuation (reduction) between a thick and stiff substrate and a brittle PV film. The strain isolation concept has been applied before [65-67], by taking advantage of the mechanics of shear lag. Lacour et al. [65] and Lu et al. [67] used a diamond-like-carbon (DLC) island on a PDMS substrate to provide strain isolation to a device from its compliant PDMS substrate. They showed that this approach works well for sub-millimeter size islands. Likewise, Sun et al. [66] used a SiN island on a PDMS substrate to demonstrate strain isolation at the top of a SiN island from its deformable PDMS substrate.

In the case of PV films that are integrated onto load-bearing structures, the underlying structure has a high stiffness [10,52-57,59,64] with elastic modulus values in the range 70-130 GPa [68], therefore, strain isolation may be possible with the aid of a compliant interface material. Towards this goal, CNTs have been deposited [69,70] as a compliant interphase on different substrates [71,72] in the past. Daraio et al. [73] developed a 100- $\mu\text{m}$  foam-like forest of coiled CNTs, Figure 1.5(a), and Ge et al. [7] fabricated hair-like CNT films with a modulus of 0.5 MPa and thickness of 280  $\mu\text{m}$ , Figure 1.5(b). However, the high temperature growth of CNTs ( $>500\text{ }^\circ\text{C}$ ) [72,74] and the constraints on the type of appropriate substrates [75,76] limit the potential applications of this approach. Furthermore, the weak adhesion of the CNTs to a functional layer is a source of early failure [7]. More recently, thin compliant multifunctional interfaces, deposited at room temperature via GLAD, have been demonstrated by Antartis et al. [1,37]. In their approach, thin films of metals or ceramics were grown in the form of coil or chevron type nanostructures with low shear and normal stiffness as described in Section 1.1.1. From a practical viewpoint the GLAD film thickness is limited to  $\sim 10\text{ }\mu\text{m}$ , which limits the smallest effective stiffness of an interface layer that could be achieved by this method. The aforementioned approaches to introduce interfacial compliance must

be put in the context of the mechanics of the overall system. An effective compliant interface layer should be able to achieve a broad range of effective stiffness values. Moreover, candidate interface materials must facilitate direct process integration, large area coverage, rapid curing, low process temperature, and strong adhesion without interfering with the functionality of the brittle film. In this dissertation research an analytical model was adopted to evaluate the requirements for an effective and efficient interface for strain transfer control.

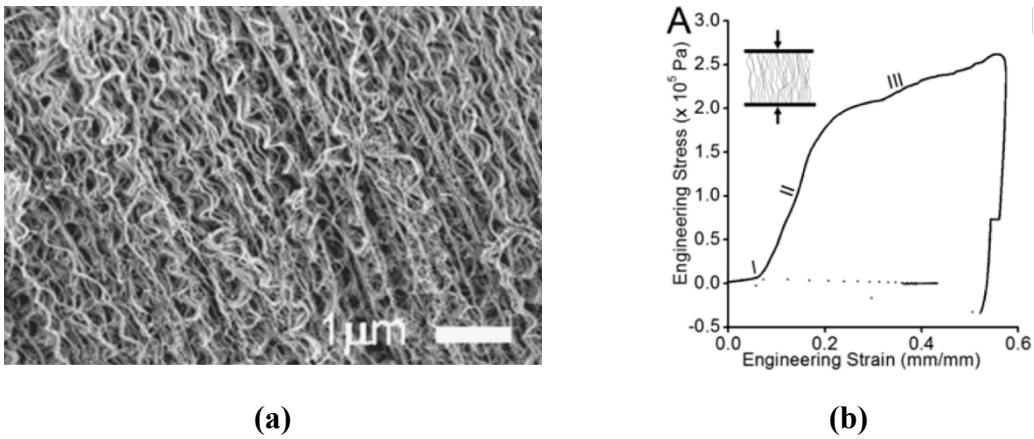


**Figure 1.5 (a)** Forest of coil-shaped carbon nanotubes [73]. Reprinted with permission from Elsevier AIP Publishing. **(b)** Stress-strain measurements of the 280-μm tall carbon nanotubes [7]. Reprinted with permission from American Chemical Society.

### 1.3 Research Objectives and Approach

Based on the two problems discussed in the last two Sections, involving interface mechanics, this Ph.D. dissertation research aimed at:

**(a)** Controlling the wrinkle pattern of a continuous stiff film on a flexible substrate via a compliant interface layer, Figure 1.6(a). The analytical models described in [13,33,77] were utilized to calculate the wrinkle wavelength, direction, and amplitude. GLAD interface layers comprised of coil or chevron-type Cu nanostructures were deposited, by

controlling the motion of the substrate during deposition, the deposition rate, and the deposition angle. The mechanical stiffness of the compliant interface layers was evaluated as a function of the process parameters. The resulting wrinkle patterns were evaluated, and predictions from analytical models were compared to the experimental results.

**(b)** Imparting strain attenuation through an interface layer between a stiff substrate (CFRP laminate) and a brittle (PV) film, therefore to extend the maximum strain that can be applied to the underlying substrate before mechanical and functional damage is induced to the brittle film, Figure 1.6(b). An analytical model [78] was employed to quantify the strain attenuation as a function of the geometric and material properties of the interface. Polydimethylsiloxane (PDMS) was selected as the interface layer due to the wide range of tunable elastic moduli and thicknesses. By adjusting the ratio of silicone elastomer to curing agent, the elastic modulus was varied in the range 0.1-2 MPa [79,80]. The broad range between 33:1 and 5:1 of elastomer-to-curing agent mixing ratios was used to control the viscosity of uncured PDMS, which, in turn, resulted in a large range of effective stiffnesses for the interface layer.

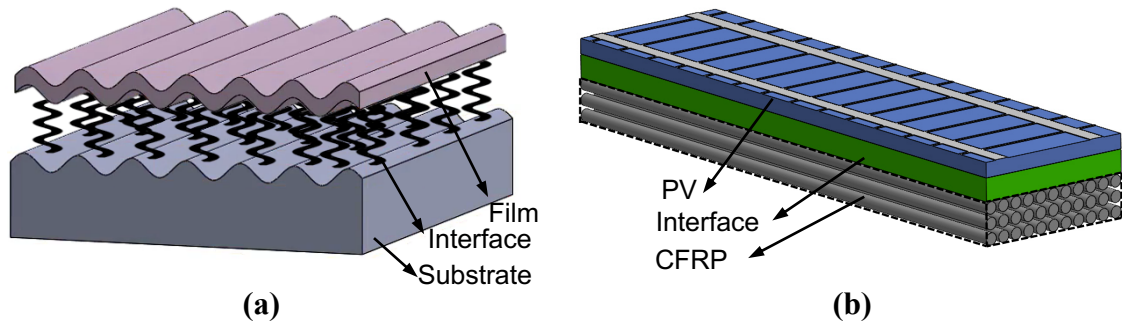


**Figure 1.6 (a)** Three-layer wrinkle system with interface layer of GLAD nanosprings. **(b)** Brittle film (PV film) - interface layer (PDMS) - substrate (CFRP laminate) system.

### 1.3.1 Research Tasks

The following tasks were carried out in this Ph.D. dissertation to achieve the aforementioned goals:

1. Study the effect of GLAD process parameters, such as deposition rate, angle, and rotation speed, on the morphology and precision of feature definition (nanosprings and nanochevrons) of nanoarchitected interface layers.
2. Calculate the effective in-plane modulus of the interface layers to control the wrinkling and employ films made of GLAD as the interface layers. Build a device to control the uniaxial strain applied to flexible PDMS substrates before and after deposition of GLAD films, and evaluate the effectiveness of GLAD interface layers in controlling the wrinkle behavior. Extend the analytical model to the case of an orthotropic interface layer to study anisotropic wrinkling and design appropriate experiments to demonstrate anisotropic wrinkling that is controlled by the interface.
3. Calculate the properties of an interface layer to achieve different degrees of strain attenuation. Utilize the model results to design, implement, and evaluate effective and efficient compliant interfaces to reduce or eliminate the strain transfer and loss of functional performance of a PV film bonded onto a CFRP laminate.

#### **1.4 Dissertation Outline**

This dissertation consists of five chapters describing the fabrication and experimental measurement methods, the data analysis, and the analytical models developed or utilized to study the problems of wrinkling and strain attenuation due to a compliant interface. Chapter 2 describes the application of GLAD, including an evaluation of process parameters, to fabricate isotropic and anisotropic interface layers. The experimental methods to evaluate the materials for wrinkling and strain attenuation are also presented in Chapter 2.

Chapter 3 discusses the results of the effort to control surface wrinkling. The effective in-plane modulus of the interface layers, and wrinkle wavelength, wrinkle direction, wrinkle amplitude, and the critical strain to initiate wrinkling are reported for two-layer and three-layer systems. The analytical model is extended for an orthotropic interface layer, whose stiffness matrix is experimentally parameterized and the predictions are compared to the experimental results.

Chapter 4 focuses on strain transfer between a load bearing CFRP laminate and an attached thin PV film. Strain attenuation, achieved by a PDMS compliant interface, is predicted by an analytical model and compared to the experimental results. The PDMS interface layer is shown to mitigate the strain transferred to the PV film and the degree the latter maintains its performance efficiency. Finally, Chapter 5 presents the conclusions of this work and an evaluation of the results of this dissertation research vis-à-vis the research objectives.

This dissertation builds on two journal publications by the author [11,12]. Chapter 3 includes material from Ref. [11]. Chapter 4 includes material from Ref. [12]. Some material from both journal publications is incorporated in Chapters 1 and 2.

## CHAPTER 2

### Experimental Methods

In this Chapter, the application of the GLAD method for the fabrication of the Cu compliant interface layers is described, including important process parameters, such as deposition angle, rate, and rotation speed that determine the morphology of GLAD nanostructures. The latter formed interface layers for the wrinkle control. Likewise, all mechanical testing methods employed in this study and the methodology to measure the electrical performance of PV films are described in this Chapter.

#### 2.1 Fabrication of Interface Layers for Wrinkle Control

The GLAD method was utilized to fabricate the interface layers in the two-layer system of a Cu thin film on a thick PDMS layer. The process parameters of GLAD, the deposition angle,  $\alpha$ , rotation speed,  $\omega$ , and deposition rate, shown in Figure 1.2(a), have a direct effect on the shape and dimensions of the fabricated nanostructures comprising the interface layers, and hence provide control of the structure and mechanical properties of the interface layers. Cu was selected for the thin film and the interface layers because of its high electrical and thermal conductivities that facilitate applications in flexible electronics, sensors and devices [81-84].

A custom e-beam evaporator system (AXXIS, Kurt J. Lesker), Figure 2.1, was used to fabricate the Cu GLAD films from Cu pellets (Mueller Industries) with a purity of 99.99% under  $5 \times 10^{-8}$  torr vacuum. A cryopump (CRYO-TORR 8, HELIX) achieved high vacuum by trapping gas molecules on its cold surface (12 K). The high vacuum ensures a large vapor mean free path that is longer than the chamber dimensions to permit

ballistic shadowing of the incoming vapor flux [35,36]. For a typical system with a source-substrate distance of  $\sim 45$  cm, an operating pressure of less than  $10^{-3}$  torr is required to achieve a sufficient mean free path [85]. Based on the material properties of Cu and the position of the gold quartz crystal relative to the graphite crucible, the tooling factor, Z-ratio, and material density were set as 46.2, 0.437 and  $8.93 \text{ g/cm}^3$  [86], respectively, in the system interface. The tooling factor stands for the ratio of the rates at which material is deposited on the quartz crystal and substrate, and is used to account for variation in thickness between the films deposited on the quartz crystal and on the substrate. The Z-ratio is a parameter that corrects for the acoustic-impedance mismatch between the quartz crystal and the deposited material.



**Figure 2.1** E-beam evaporator system (AXXIS, Kurt J. Lesker).

Compared to other physical vapor deposition methods such as sputtering, e-beam evaporation provides highly directional deposition and therefore repeatable and accurate definition of the geometry of GLAD nanostructures [85-88]. Dick et al. [88] reported that sputtering has a larger flux angle distribution along the wafer due to its reduced directionality, which can lead to non-uniform shadowing. A custom 6" sample stage was controlled by the instrument software to define the deposition angle and azimuthal

rotation of the substrate. The deposition temperature, which is defined as the temperature of the substrate was measured as  $35\pm 5$  °C for the entire duration of one deposition (~1.5 hr) by using temperature indicating labels (Omega Engineering, Inc.) A higher deposition temperature had a significant effect on the morphology of GLAD films due to higher diffusion of the Cu atoms [89], since higher atom mobility suppresses the shadowing effect. Sumigawa et al. [89] showed that GLAD nanostructures grown at progressively lower substrate temperatures suffered less from atomic diffusion, and resulted in well-defined shapes, Figure 2.2.

Herein, for the aforementioned pressure and temperature deposition conditions, we evaluated the effect of deposition angle, deposition rate, and substrate rotation speed, on the geometry and shape of grown GLAD nanostructures.

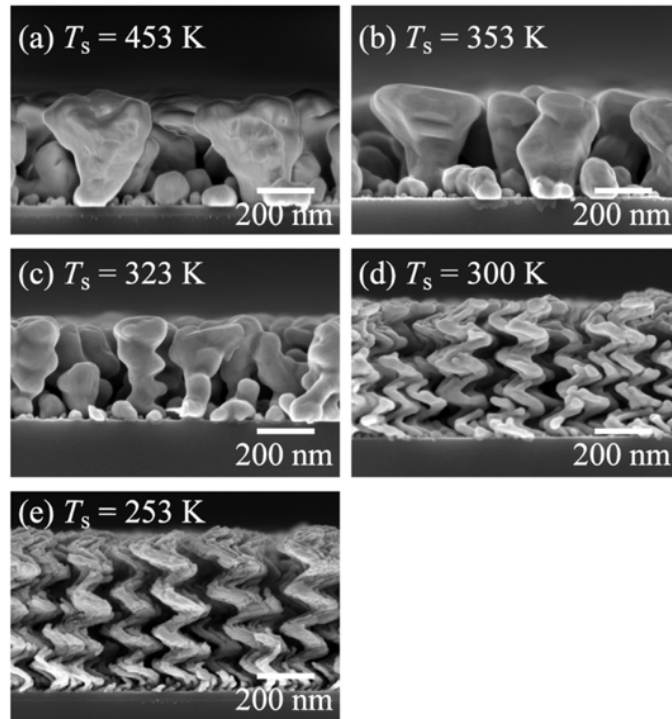


**Figure 2.2** Cu nanostructures deposited at substrate temperatures 253 - 453 K [89]. Reprinted with permission from American Vacuum Society.

The deposition angle,  $\alpha$ , i.e. the angle between the incident flux and the substrate normal, Figure 1.2(a), controls the growth angle,  $\beta$ , which is the angle between a growing nuclei and the substrate normal [35]. Based on experimental observations, Nieuwenhuizen and Haanstra [90] were the first to utilize the tangent rule model:

$$\tan\alpha = 2\tan\beta \quad (2.1).$$

Later, Tait et al. [91] reported on a ballistic model by using the shape of a disc to represent the average trajectory of a large number of atoms that have limited surface diffusion when arriving at the substrate:

$$\beta = \alpha - \arcsin\left(\frac{1 - \cos\alpha}{2}\right) \quad (2.2).$$

These simple geometrical models that were put forth in the past to relate  $\alpha$  and  $\beta$  [90,91], did not take into account the material properties and, therefore, often failed to capture the correct growth angle,  $\beta$  [92]. For instance, Lintymer et al. [92] compared the growth angle,  $\beta$ , of Cr nanocolumns with predictions by Equations (2.1) and (2.2). The value of  $\beta$  of Cr nanocolumns deposited on a Si substrate only fitted each model at certain range of the deposition angle. Because of the lack of a universally accurate model, an experimental campaign was launched in this dissertation research to evaluate the feature geometry for different values of  $\alpha$ . The growth angle,  $\beta$ , of Cu nanochevron was evaluated from SEM images as a function of the deposition angle,  $\alpha$ , and the results are presented and discussed in Chapter 3.

While columnar growth takes place at an angle  $\beta$ , a continuous slow substrate rotation produces nanosprings whose pitch is given by [35]:

$$P = \frac{R}{\omega} \quad (2.3),$$

where  $P$  is the pitch [ $\text{\AA}$ ],  $R$  is the actual deposition rate [ $\text{\AA}/\text{s}$ ], and  $\omega$  is the azimuthal rotation speed [revolutions/s]. The actual deposition rate, namely the deposition rate in the direction of the substrate normal, is much smaller than the vapor flux (nominal

deposition rate) measured by the quartz balance, installed  $\sim 10''$  above the crucible in the e-beam evaporator, and depends on  $\alpha$ . The actual deposition rate vs. deposition angle ( $85^\circ$ ,  $86^\circ$  and  $87^\circ$ ) was measured from SEM images of Cu nanochevrons for a nominal deposition rate of  $10 \text{ \AA}/\text{sec}$  and the results are provided in Chapter 3. Henceforth by deposition rate we refer to the nominal deposition rate. For all GLAD films, the highest deposition rate available in the AXXIS system of  $10 \text{ \AA}/\text{s}$  was selected, because slower deposition rates suffered from strong diffusion effects and resulted in fused nanostructures. By controlling  $\alpha$ ,  $P$ ,  $R$  and  $\omega$ , discrete films comprised of nanosprings and nanochevrons were fabricated. The geometric versatility of such nanostructures provided a large range of effective elastic properties for the interface layers used to control wrinkling in Chapter 3.

## 2.2 Mechanical Testing

Uniaxial tension tests were conducted to determine the elastic modulus of freestanding PV films, CFRP laminates, and PDMS films. The tests on PDMS and PV films were performed with the Bose ElectroForce 3200 Series III Test Instrument at the strain rate  $10^{-4} \text{ s}^{-1}$ . A speckle pattern was spray-painted with an airbrush on the PDMS and PV specimens, Figure 2.3(a), to calculate the strain fields via Digital Image Correlation (DIC) from optical images obtained during testing (Sony DFW-X10 CCD camera with Pentax C32500KP lens) at 1 fps. CFRP laminates were tested for their longitudinal elastic modulus, using an Instron 4483 mechanical testing machine at the strain rate  $10^{-4} \text{ s}^{-1}$ . A speckle pattern was deposited onto the CFRP laminates, to obtain the strain field via DIC and calculate the elastic modulus and Poisson's ratio. CFRP laminates with bonded PV films (with and without a PDMS interface) were also tested using the same methodology. For those test specimens, a speckle pattern was deposited on the side of the laminate to obtain the CFRP strain field via DIC, while a second CCD camera with a high magnification objective ( $30\times$ ) was used to take real-time images of the surface of the PV film that was co-cured with the CFRP laminate. The second CCD camera with a VZM<sup>TM</sup> 450i lens (Edmund Optics, Inc.) was integrated on a multi-axis

stage with a micrometer to accurately focus on the specimen surface. The inherent speckle pattern of the PV film, Figure 2.3(b), was used to calculate the uniaxial strain field via DIC. The same optical images provided real-time observation of the fragmentation of the ZnO and aSi layers of the PV film. To highlight the fragmentation lines, the PV film was also illuminated at a 30° angle with a 15-Watt light source, which was turned off when measuring the photovoltaic FF. The results of the strain measurements from the PV film and CFRP laminate were then used to calculate the strain attenuation.

To evaluate the effect of the interface layer on wrinkling, the PDMS substrate was pre-stretched by 10% via a screw-driven, unidirectional mechanical loading device, Figure 2.4, before depositing the nanostructured GLAD films and the solid Cu films. After deposition, the PDMS substrate was released in 0.25% strain increments via a fine screw on the loading frame. The easy integration of the loading stage device with the deposition chamber allowed for control of the loading direction with respect to the resulting orientation of the GLAD films, which enabled the study of the effect of GLAD film orientation on wrinkling, which is described in Chapter 3. The wavelength, angle, and amplitude of the wrinkle patterns were measured with a 3D Laser Scanning Confocal Microscope (Keyence VK-X1000).

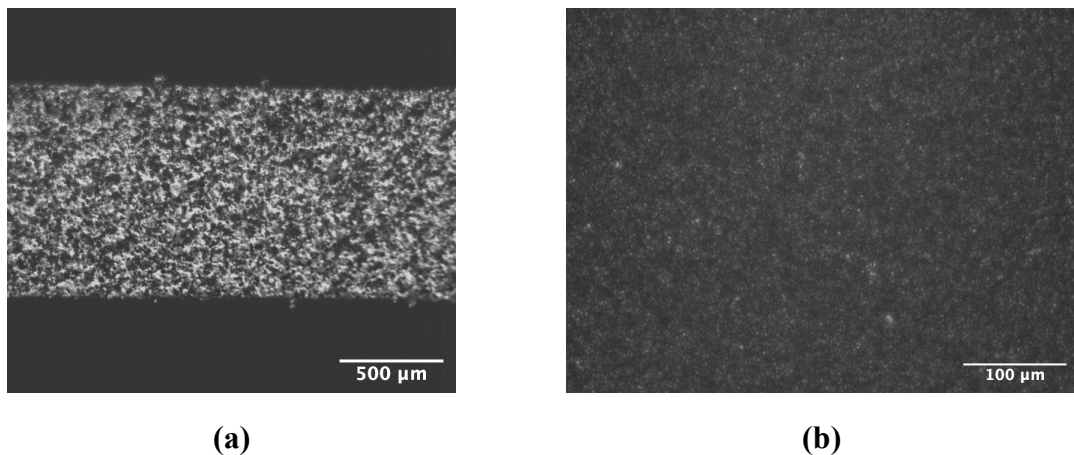


**Figure 2.3** Speckle pattern on the gauge section of (a) 52-μm thick PV film. (b) Inherent speckle pattern of PV film.

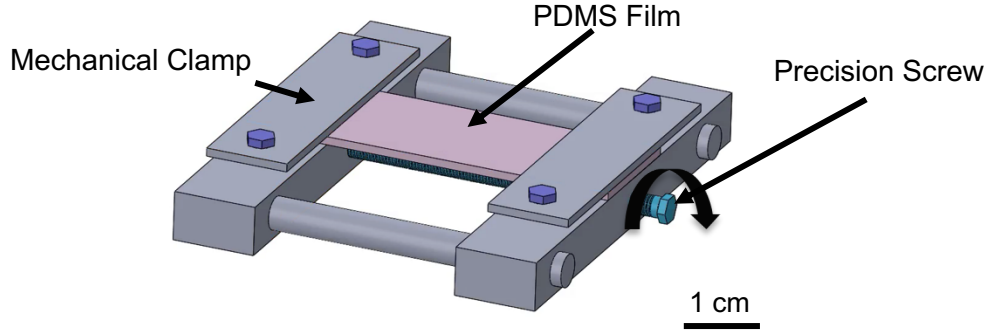


**Figure 2.4** Mechanical stage to pre-stretch PDMS films before GLAD deposition and release them after deposition.

### 2.3 Measurement of PV Fill Factor

The PV full modules (7.6-cm long) cured onto the CFRP laminate were wired to obtain the fill factor (FF) during mechanical loading. Two 30 W light sources served as a stable light source. The PV module was modeled as an ideal diode assuming no losses from bulk resistance and junction leakage, according to Morgan et al. [93]. The total current,  $I$ , and voltage,  $V$ , under a constant light source are related as:

$$\ln(I_{SC} - I) = \ln I_o + \frac{|e|V}{\gamma k_B T} \quad (2.4),$$

where  $I_L$ ,  $e$ ,  $T$ ,  $k_B$  are the short circuit current, the magnitude of the electronic charge, the absolute temperature, and the Boltzmann constant, respectively. The diode factor,  $\gamma$ , and the reverse diode saturation current,  $I_o$ , were obtained by a circuit of two multimeters and one resistance substitution box with  $\frac{|e|V}{\gamma k_B T} \gg 1$  [93], as shown in Figure 2.5.

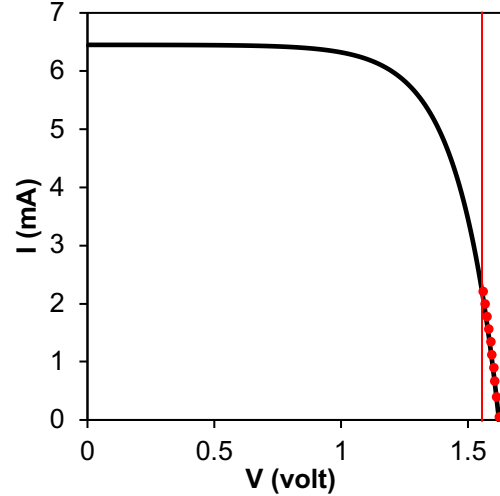


**Figure 2.5** Calculation of diode factor and reverse diode saturation current by fitting the voltage and current in the range  $\frac{|e|V}{\gamma k_B T} \gg 1$  as indicated by the red line above. The diode factor and the reverse diode saturation current were used to plot the I-V curves of a PV film module.

Following the methodology by Morgan et al. [93], the I-V characteristic curves were then plotted via:

$$I = I_o \left[ 1 - \exp\left(\frac{|e|V}{\gamma k_B T}\right) \right] + I_{sc} \quad (2.5).$$

where  $I_{sc}$  is the short circuit current.

Finally,  $FF$  was calculated as:

$$FF = \frac{I_{mp} V_{mp}}{I_{sc} V_{oc}} \quad (2.6),$$

where  $V_{oc}$  is the open circuit voltage, and  $I_{mp}$  and  $V_{mp}$  are the voltage and current on the I-V characteristic curve at the practical maximum power.  $V_{oc}$  and  $I_{sc}$  were measured for  $I \rightarrow 0$  and  $V \rightarrow 0$ , respectively. The FF of the PV modules was measured in their as-received form and after they were integrated onto CFRP laminates to confirm that no damage was induced during specimen preparation and curing.

## 2.4 Summary

The GLAD method, employed to fabricate compliant interface layers for wrinkle control was presented and discussed. The GLAD parameters utilized to control the geometry and dimensions of GLAD nanostructures, and therefore influence their mechanical properties of the resulting films were also presented. Uniaxial tension experiments performed to measure the elastic modulus of the materials in the wrinkle and the strain transfer problems were discussed. Uniaxial tension experiments were also used to measure the strain for the evaluation of strain attenuation. The methodology by Morgan et al. [93] to characterize the performance of PV films was described. Finally, a custom mechanical loading stage device was built to carry out the wrinkling experiments.

# CHAPTER 3

## Control of Wrinkling through Interface Engineering

A new approach is presented in this Chapter to control surface wrinkling without modifying the applied loading and the composition or the structure of a stiff film-compliant substrate system. Cu and PDMS are employed as the stiff film and compliant substrate, respectively. Herein we are taking advantage of nanoarchitected films fabricated by GLAD to deposit interface layers comprised of coiled or chevron-type Cu nanostructures, such as nanosprings or nanochevrons. The optimal process parameters of GLAD, including the deposition rate, deposition angle, and rotation speed, are identified in order to fabricate the isotropic and orthotropic compliant interface layers, which, in turn, are used to control the overall wrinkle behavior of a composite, comprised of a stiff top film and an elastomeric substrate. The experimental results are presented along with the formulation and the closed form solution of an analytical model adopted from literature and further modified for the purposes of this research. The isotropic wrinkle behavior is modeled with the aid of the analytical models by Allen [33] and Lejeune et al. [77]. In addition, the analytical model by Yin et al. [13] is extended and utilized to simulate the anisotropic wrinkle behavior. Importantly, as part of the experimental effort to characterize the wrinkle behavior of two- and three-layer systems, the effective in-plane compressive modulus of GLAD interface layers is quantified for the first time as a function of their geometric features.

### 3.1 Experimental Methods

#### 3.1.1 Process Parameters for GLAD Nanostructures

The effect of deposition angle,  $\alpha$ , deposition rate, and rotation speed,  $\omega$ , on the dimensions and geometry of GLAD nanostructures was studied under the fabrication conditions described in Section 2.1.

Cu nanochevrons fabricated on a seeded substrate with different values of deposition angle,  $\alpha$ , are shown in Figure 3.1. For a normal incidence deposition rate of  $10 \text{ \AA}/\text{sec}$ , the actual deposition rate was measured to be  $1.68 \text{ \AA}/\text{sec}$ ,  $1.58 \text{ \AA}/\text{sec}$ , and  $1.46 \text{ \AA}/\text{sec}$  for  $\alpha$  of  $85^\circ$ ,  $86^\circ$ , and  $87^\circ$ , respectively via SEM imaging of the resulting films. The growth angle,  $\beta$ , increased for higher values of  $\alpha$ . It was measured as  $81.4^\circ$ ,  $82.8^\circ$ , and  $83.6^\circ$  for  $\alpha$  of  $85^\circ$ ,  $86^\circ$ , and  $87^\circ$ , respectively, from SEM images. Moreover, the separation between nanochevrons increased with  $\alpha$  due to the increasing shadowing effect between nanochevrons. As described in the next Section,  $\alpha$  was selected to be  $86^\circ$  because it produced the finest nanostructures. Large deposition angles led to excessive shadowing which halted the growth of some GLAD nanostructures, Figure 3.1(c).

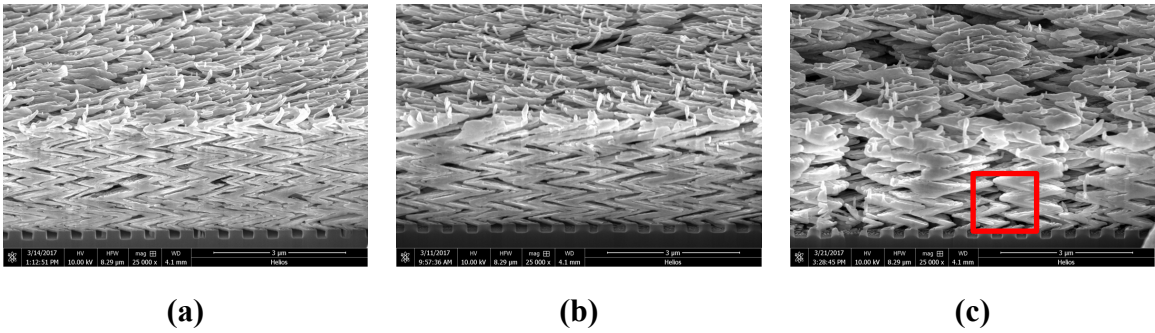


**Figure 3.1** Seeded Cu nanochevron films deposited at  $10 \text{ \AA}/\text{sec}$  and deposition angle,  $\alpha$ , (a)  $85^\circ$ , (b)  $86^\circ$ , and (c)  $87^\circ$ . The nanochevron structure in the red bod in (c), was terminated during deposition.

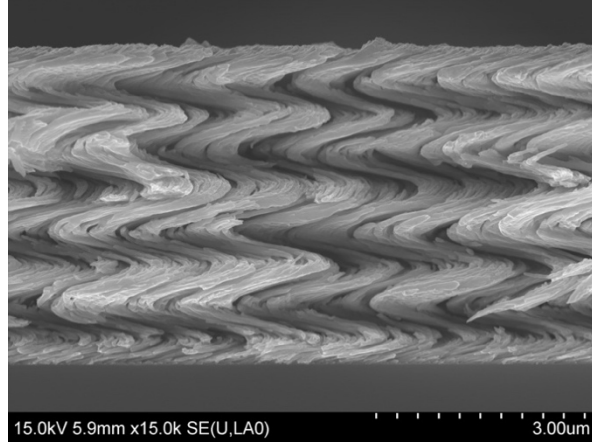
As shown by Equation (2.3), GLAD nanostructures with different geometries can be fabricated by controlling the pitch. To that effect, the deposition rate and speed,  $\omega$ , were used to control the pitch. For finite rotation speeds, the pitch of nanosprings decreased with increasing  $\omega$ . The resulting Cu films transitioned from nanosprings to nanocolumns when  $\omega$  changed from 0.025 to 20 rpm at the same deposition rate, Figure 3.2. For instance,  $\omega = 0.025 \text{ rpm}$  and  $\omega = 0.01 \text{ rpm}$  produced a pitch of  $0.38 \text{ \mu m}$  and  $0.95 \text{ \mu m}$ , respectively, Figures 3.2(a) and 3.2(b). The different structure resulted in compressive different stiffness for a given film thickness [38,94,95]. The coil diameter of

the same nanospring structures was measured to be  $0.76\ \mu\text{m}$  and  $1.8\ \mu\text{m}$  for  $\omega = 0.025$  rpm and  $\omega = 0.01$  rpm, respectively. Smaller coil diameter led to larger separation between nanostructures, which, in turn, influences the interaction between individual nanostructures. Finally, the nanosprings transitioned to nanocolumns, Figure 3.2(c), when the pitch became negligible for  $\omega = 20$  rpm.

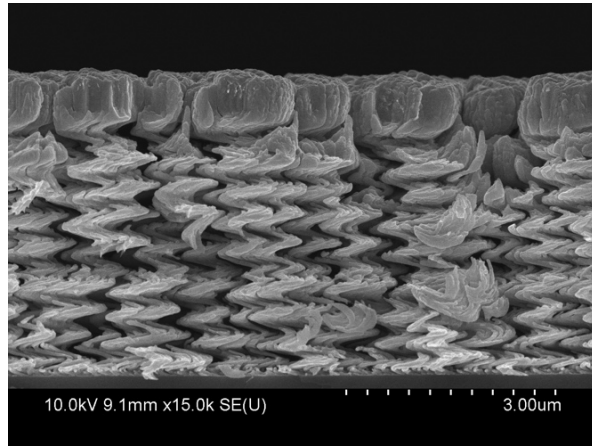
The same conclusion was drawn by increasing the deposition rate. As shown in Figure 3.3, under the same rotation speed,  $\omega$ , the pitch became twice as large when the deposition rate was doubled, as also expected from Equation (2.3), because the higher deposition rate reduced the amount of time for atoms to diffuse after arriving on the substrate. These nanospring films were employed as isotropic interface layers.

With zero rotation speed, slanted columns can be made, Figure 3.4(a), and the growth angle,  $\beta$ , was directly controlled by the deposition angle, as discussed in Section 2.1.1. Furthermore, nanochevron structures were fabricated by periodically applying  $180^\circ$  step rotations, e.g. Figures 3.4(b) and 3.4(c). The pitch can be controlled by the deposition rate or time (this dissertation). For the same deposition rate, the pitch increased from  $0.25\ \mu\text{m}$ , Figure 3.4(b), to  $0.5\ \mu\text{m}$ , Figure 3.4(c), by doubling the deposition time per segment. The nanochevron films are anisotropic, which was taken advantage of in this dissertation.

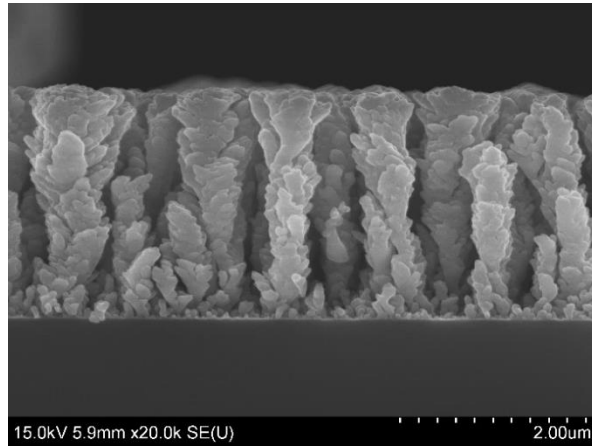
Alternatively, square nanospring structures comprised of slanted columns were fabricated by periodically rotating the sample stage by  $90^\circ$ , Figure 3.5. The pitch of square nanosprings was controlled by either the deposition rate or the deposition time (this dissertation).



(a)

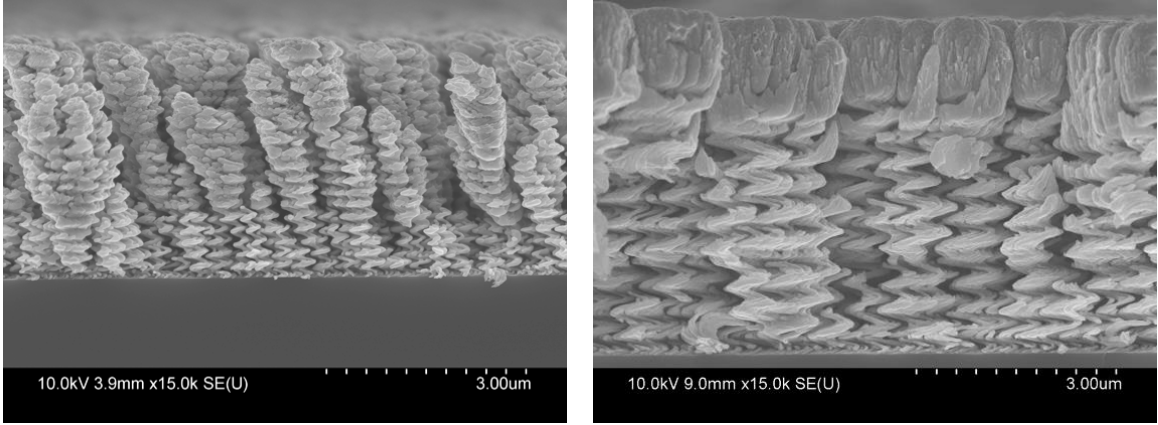


(b)



(c)

**Figure 3.2** Cu films deposited at  $\alpha = 86^\circ$ , deposition rate of  $10 \text{ \AA}/\text{sec}$  and  $\omega$  equal to (a) 0.01 rpm, (b) 0.025 rpm, and (c) 20 rpm.

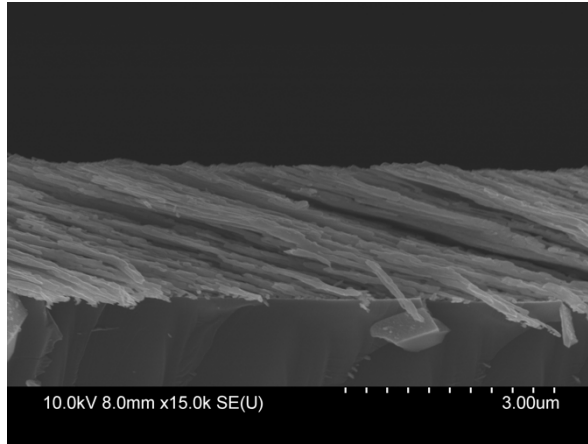


(a)

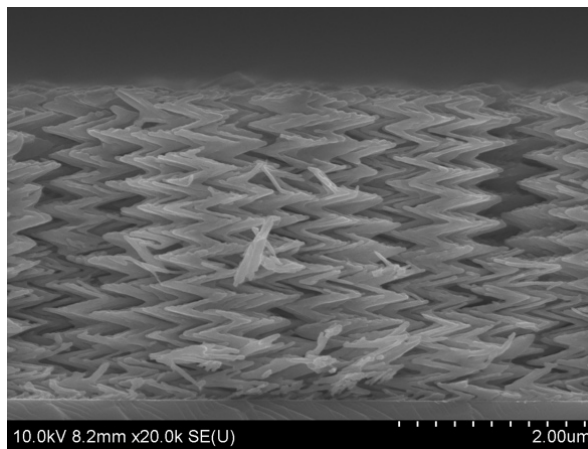
(b)

**Figure 3.3** Cu nanospring films deposited at  $\omega = 0.025$  rpm,  $\alpha = 86^\circ$  and deposition rate (a)  $5 \text{ \AA}/\text{sec}$ , and (b)  $10 \text{ \AA}/\text{sec}$ .

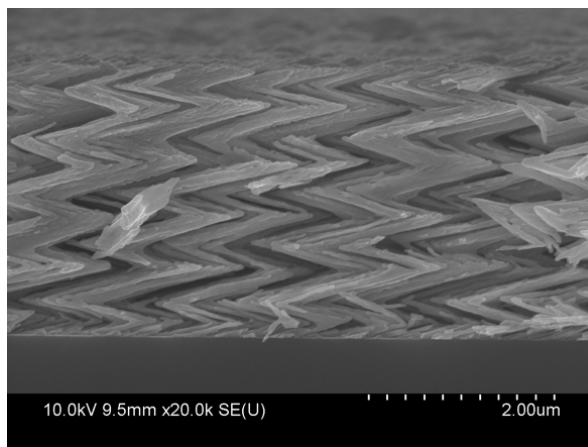
The deposition angle and deposition rate were calibrated and used in the next Section to fabricate isotropic and orthotropic interface layers for the wrinkle control.



(a)



(b)



(c)

**Figure 3.4** (a) Cu slanted columns deposited at  $10 \text{ \AA}/\text{sec}$ . Cu nanochevron films deposited at  $10 \text{ \AA}/\text{sec}$  with (b)  $0.25 \text{ }\mu\text{m}$  and (c)  $0.5 \text{ }\mu\text{m}$  pitch. The deposition angle,  $\alpha$ , was  $85^\circ$  in (a) and  $86^\circ$  in both (b) and (c).

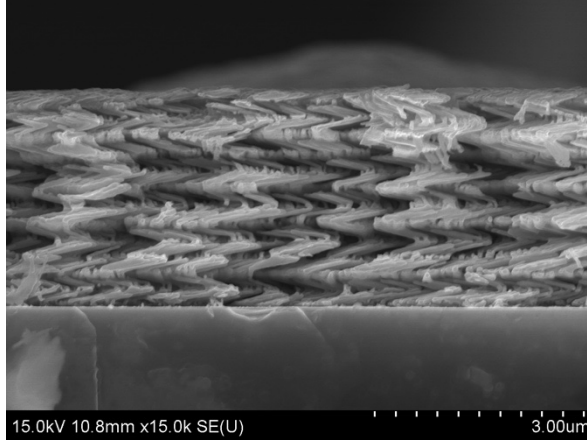


**Figure 3.5** Square Cu nanosprings deposited at  $\alpha = 86^\circ$ , deposition rate  $10 \text{ \AA}/\text{sec}$ , and  $0.5\text{-}\mu\text{m}$  pitch.

### 3.1.2 Deposition of Solid and Nanostructured Interface Layers

Uniaxial strain was applied to PDMS substrates in all experiments presented in this Chapter. A 2-mm thick PDMS film served as the substrate, synthesized by mixing a silicone elastomer with curing agent (SYLGARD 184, Dow Corning, Midland, MI) at 2:1 ratio and then degassing for 25 min. Upon mixing, PDMS was oven-cured at  $165^\circ\text{C}$  for 2 days to achieve maximum stiffness [80]. Solid Cu films and discrete Cu GLAD films were deposited via electron beam (e-beam) evaporation on the PDMS substrate. To ensure strong adhesion between PDMS and the Cu films, the PDMS surface was treated with oxygen plasma (Harrick Plasma PDC-32G) for 3 min (18 W, 700 mTorr) after the PDMS film was pre-stretched by the loading stage. Then, a 10-nm Ti layer, serving as an adhesion layer between PDMS and Cu, was deposited by an AJA DC Sputtering System.

A  $0.5\text{-}\mu\text{m}$  solid Cu cap layer, serving as the top solid film that induces wrinkling, was deposited at the deposition rate of  $10 \text{ \AA}/\text{sec}$ ,  $\omega = 20 \text{ rpm}$ , and  $\alpha = 20^\circ$ . The top solid cap layer thickness was kept the same in all test specimens, while nanosprings and nanochevrons with a pitch of  $0.25 \mu\text{m}$  or  $0.5 \mu\text{m}$  and total height of  $2.0 \mu\text{m}$  were deposited using the process parameters in Table 3.1. As described in Section 3.1.1, the deposition angle,  $\alpha$ , and normal deposition rate were selected to be  $86^\circ$  and  $10 \text{ \AA}/\text{s}$ ,

respectively. To study the effect of the interface layer with respect to the top film thickness as well as the entire Cu film thickness (top solid layer + interface), solid Cu films of  $0.5\ \mu\text{m}$  and  $2.5\ \mu\text{m}$  were also deposited at  $\alpha = 0^\circ$  and  $\alpha = 20^\circ$ . Shown in Figures 3.7(a,b), Cu nanospring films with small pitch ( $0.25\ \mu\text{m}$ ) and small coil diameter ( $0.46\ \mu\text{m}$ ), and large pitch ( $0.5\ \mu\text{m}$ ) and large coil diameter ( $0.89\ \mu\text{m}$ ) were fabricated for  $\omega = 0.038\ \text{rpm}$  and  $\omega = 0.019\ \text{rpm}$  and constant deposition rate, respectively. Increasing  $\omega$  resulted in smaller pitch, as expected from Equation (2.3). As deduced from Figures 3.7(a,b), larger coil pitch also resulted in increased intertwining between adjacent Cu coils, and, therefore, higher film cohesion and stiffness, as will be shown in a later Section. Cu nanosprings with helical coils resulted in roughly in-plane isotropic films. On the other hand, chevron-like nanostructures produced orthotropic films. The latter were grown by periodically applying a  $180^\circ$  step rotation to the substrate. The time interval between  $180^\circ$  step rotations controlled the chevron pitch, Figure 3.7(c-i). In nanochevron films, the principal stress direction,  $\theta_p$ , with respect to the principal material axis,  $x$ , of the interface layer, Figure 3.6, was controlled by positioning the unidirectional, screw-driven mechanical loading stage built for this study at an angle  $\theta_p$  with respect to the deposition direction, Figures 3.6 and 2.4. Then, the sample stage was periodically positioned at  $\theta_p$  and  $180^\circ + \theta_p$  to produce nanochevron structured films.

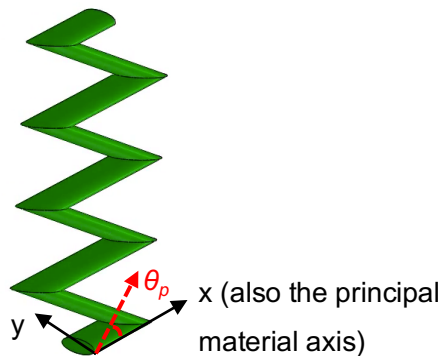
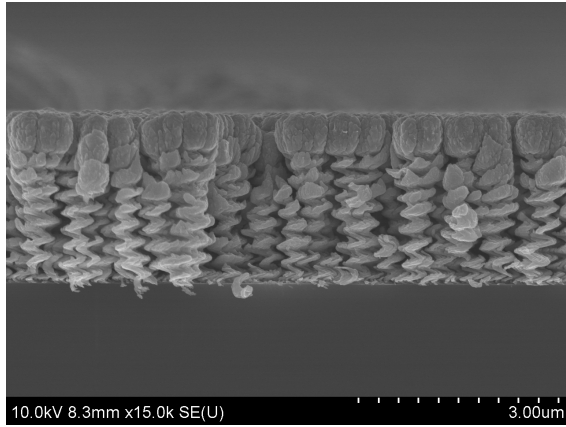
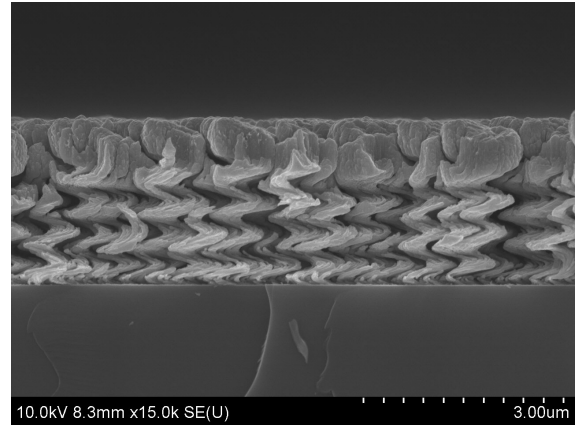


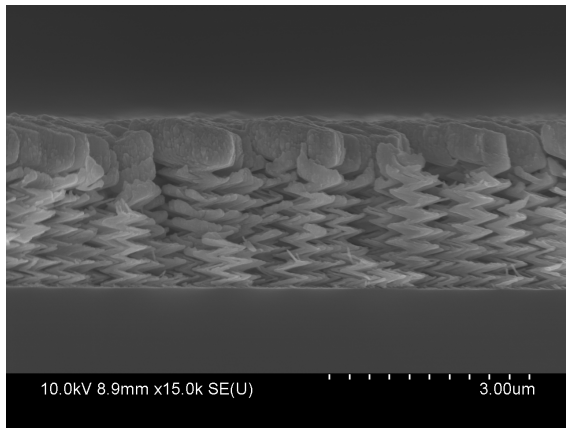
**Figure 3.6** A single nanochevron with its material axes aligned with the x and y axes. The principal material axis is aligned with the x axis.



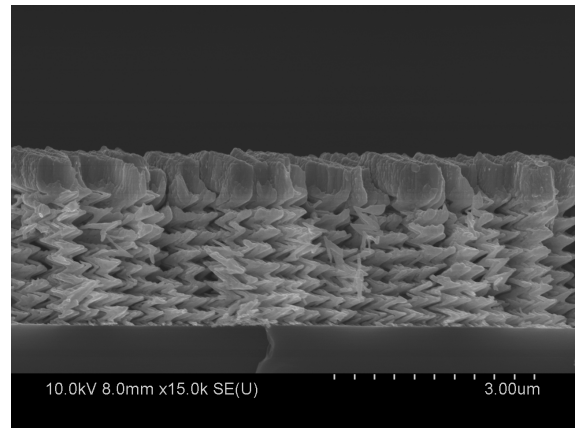
(a)



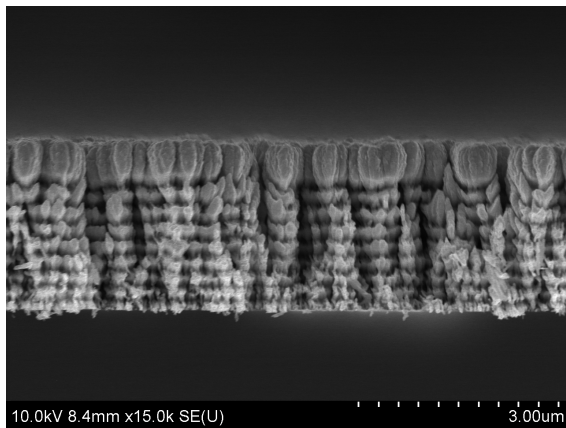
(b)



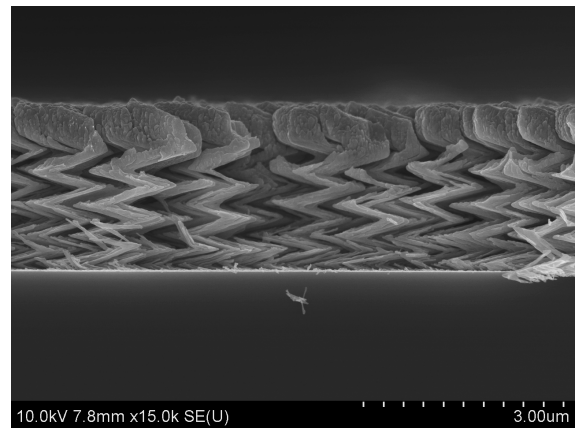
(c)



(d)



(e)



(f)

(Figure 3.7 continued)

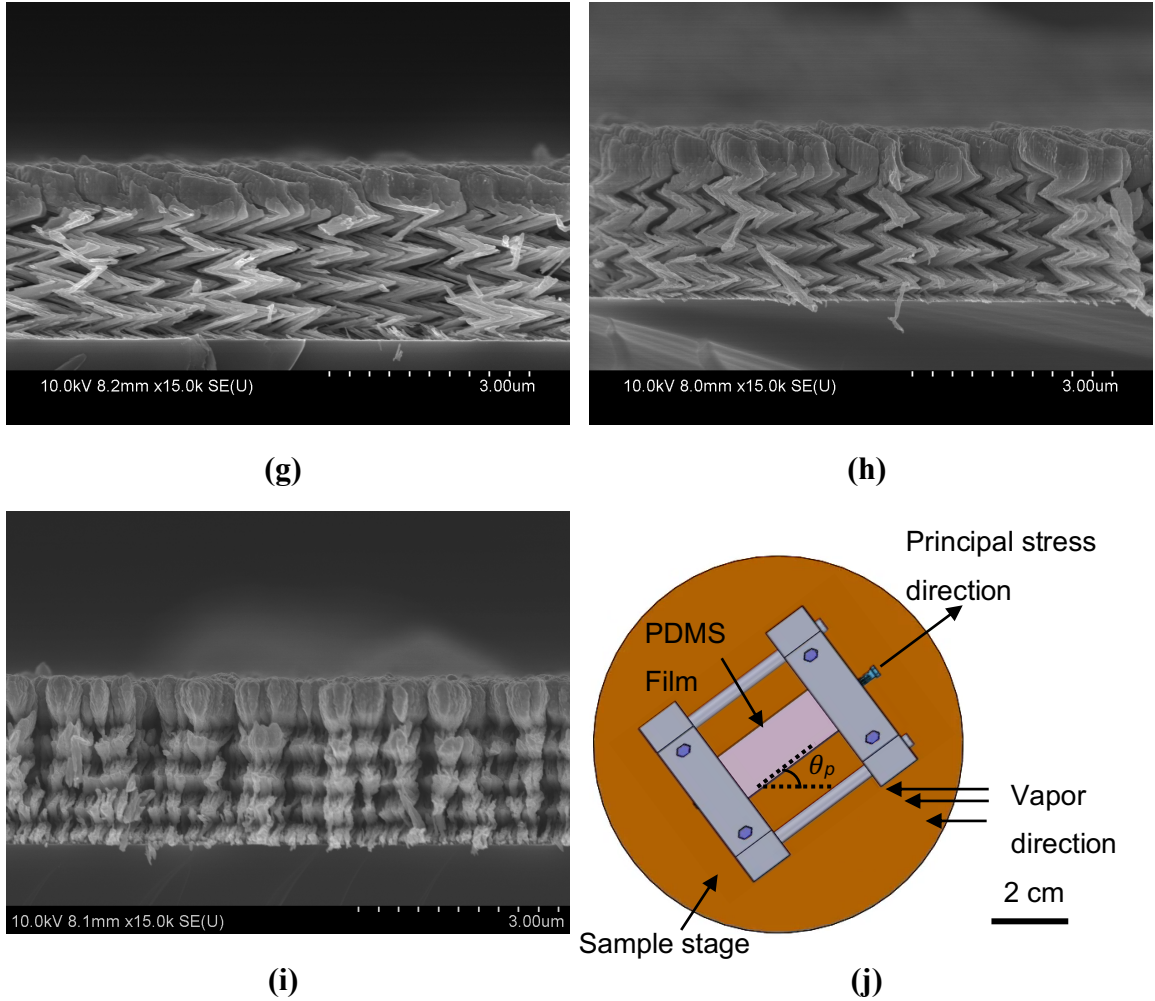


**Figure 3.7** Cu nanospring films with (a) 0.25- $\mu\text{m}$  and (b) 0.5- $\mu\text{m}$  pitch and a 0.5- $\mu\text{m}$  solid Cu cap layer. Cu nanochevron films with 0.25- $\mu\text{m}$  pitch and principal stress direction at: (c)  $0^\circ$ , (d)  $45^\circ$ , and (e)  $90^\circ$  with respect to the principal material axis. Cu nanochevron films with 0.5- $\mu\text{m}$  pitch and principal stress direction at: (f)  $0^\circ$ , (g)  $20^\circ$ , (h)  $45^\circ$ , and (i)  $90^\circ$  with respect to the principal material axis. All nanochevron films are terminated with a 0.5- $\mu\text{m}$  solid Cu cap layer. (j) Schematic of loading stage positioned on the sample stage of the e-beam evaporator.

**Table 3.1** Process parameters for solid and nanostructured Cu films.

<b>Film structure</b>	<b>Pitch height (μm)</b>	<b>Rotation speed (rpm)</b>	<b>Deposition angle (°)</b>	<b>Deposition rate (Å/s)</b>
<b>Solid</b>	N/A	20	0	10
<b>Solid</b>	N/A	20	20	10
<b>Springs</b>	0.25	0.038	86	10
<b>Springs</b>	0.5	0.019	86	10
<b>Chevrons</b>	0.25	0	86	10
<b>Chevrons</b>	0.5	0	86	10

## 3.2 Analytical Problem Formulation

### 3.2.1 Wrinkling of Isotropic Two- and Three-layer Material Systems

The wrinkle response of an isotropic two-layer system comprised of a thick substrate with modulus  $E_s$  and thickness  $t_s$ , covered with a thin film with modulus  $E_f$  and thickness  $t_f$ , such that  $t_s \gg t_f$ , and  $E_s \ll E_f$ , Figure 3.8(a), is governed by the Föppl–von Kármán equation that describes the deflection  $w$  of a thin flat plate attached to an infinite substrate under plane-stress conditions [96]:

$$\begin{aligned}
 D_1 \frac{d^4 w}{dx^4} + (2\nu_{12} D_1 + D_3) \frac{\partial^4 w}{\partial x^2 \partial y^2} + D_2 \frac{\partial^4 w}{\partial y^4} \\
 - hb \left[ \frac{\partial}{\partial x} \left( \sigma_{xx} \frac{\partial w}{\partial x} + \sigma_{xy} \frac{\partial w}{\partial y} \right) + \frac{\partial}{\partial y} \left( \sigma_{yy} \frac{\partial w}{\partial y} + \sigma_{xy} \frac{\partial w}{\partial x} \right) \right] \\
 = qb
 \end{aligned} \tag{3.1},$$

where  $w$  is the deflection of the film,  $b$  and  $h = t_f$  are the width and thickness of the film, respectively,  $D_1 = D_2 = E_f^* I_f = E_f^* \frac{bh^3}{12}$  are the flexural rigidities of the film in  $x$  and  $y$

directions, respectively,  $D_3 = \frac{bh^3}{3} G_{f,12}$  is the torsional rigidity and  $G_{f,12}$  the in-plane shear modulus of the film.  $I_f$  is moment of inertia of the film, Figure 3.8(a),  $q = -wK_s$  is the normal traction between the film and the substrate,  $K_s = \frac{E_s^* n}{2}$  is the transverse stiffness of the substrate as it responds to the sinusoidal deflection of the film [97],  $n$  is the wavenumber,  $\nu_{12}$  is the Poisson's ratio, and  $E^* = E/(1-\nu^2)$ . For isotropic films,  $D_1 = D_2$ .

In the case of uniaxial compression, Equation (3.1) is reduced to:

$$D_1 \frac{d^4 w}{dx^4} - hb\sigma_{xx} \frac{d^2 w}{dx^2} = qb \quad (3.2).$$

and wrinkling is controlled by the normal stress,  $\sigma_{xx}$ , which is also the principal stress. In this study, all experiments were carried out under uniaxial compression. Therefore, henceforth the direction of the applied force is referred to as the principal stress direction, see also Figure 3.8(c).

Herein, the problem formulation by Allen [33] for an isotropic two-layer system is adopted. In this formulation the in-plane shear tractions and displacements are not considered. As a result, any bending moments in the film caused by the in-plane shear traction at the interface are omitted because the film is much thinner than the substrate. When the critical strain for wrinkling is reached, the film deflection  $w$  is described by a sinusoidal function, Equation (A2). After  $w$  is entered into Equation (3.2), the critical wavenumber,  $n_{cr}$ , for which wrinkling initiates can be found by minimizing  $\sigma_{xx}$  with respect to  $n$ , which is then used to calculate the wrinkle wavelength,  $\lambda$ , from  $n_{cr} = 2\pi/\lambda$ . The solution of Equation (3.2), for the wrinkle wavelength,  $\lambda$ , critical strain,  $\varepsilon_c$ , and wrinkle amplitude,  $w_0$ , as reported by Allen [33], is provided in Appendix A2 by Equations (A3b), (A4), and (A6), respectively. In this problem formulation, the wrinkle wavelength is determined by the material properties and the thickness of the two layers. Namely, for a fixed two-layer material system, the wrinkle wavelength,  $\lambda$ , is also fixed, Equation (A3b), and only the wrinkle amplitude,  $w_0$ , can be varied by controlling the

applied compressive strain,  $\varepsilon$ , Equation (A6). From Equation (A6), the wrinkle amplitude,  $w_0$ , can be related to the critical strain,  $\varepsilon_c$ , as:

$$\varepsilon_c = \varepsilon - \frac{\pi^2 w_0^2}{\lambda^2} \quad (3.3).$$

The average value for  $\varepsilon_c$  for each sample type was calculated by using the experimental data for  $\lambda$  and  $w_0$  in Equation (3.3) for different values of the applied strain,  $\varepsilon$ .

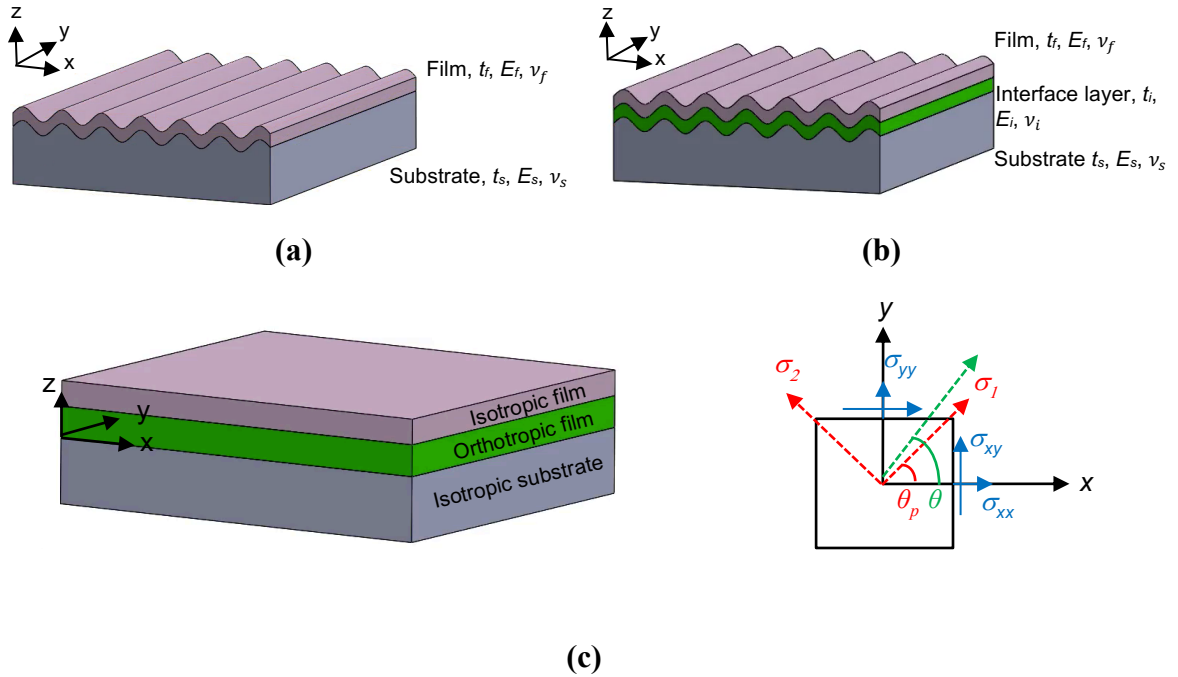


**Figure 3.8** (a) Bilayer and (b) trilayer wrinkling with isotropic constituent layers. (c) Trilayer material system with orthotropic interface layer between an isotropic substrate and an isotropic top solid film.  $\sigma_{xx}$ ,  $\sigma_{yy}$ , and  $\sigma_{xy}$  are in-plane stress components defined by the  $x$  and  $y$  axes,  $\sigma_1$  and  $\sigma_2$  are the principal stresses, and  $\theta_p$  and  $\theta$  are the principal stress direction and the wrinkle direction, respectively, with respect to the principal material axis,  $x$ .

Instead of modifying the top film material or thickness, as commonly done for a hard film-compliant substrate system to control the wrinkle pattern [22,34], a compliant

interface layer can provide an alternative means to modify the wrinkle wavelength, amplitude and orientation while maintaining the properties and thickness of the main material system constituents, namely the elastomeric substrate and the solid top film. This results in a three-layer system that includes an interface layer with thickness  $t_i$ , such that  $t_s \gg t_i \sim t_f$ , and modulus,  $E_i$ , Figure 3.8(b), where the subscript  $i$  corresponds to the interface material. The wrinkle behavior can still be described by the Föppl–von Kármán, Equation (3.1), with the same assumptions as in the case of a two-layer system. The problem formulation by Lejeune et al. for a three-layer system under uniaxial compression is adopted to obtain an analytical solution [77, 98]. For a three-layer system, Lejeune et al. [77] provided analytical solutions to Equation (3.1) by considering three simplified model cases that evaluate the role of the interface layer in the mode of wrinkling. Determination of the appropriate simplified model case is based on a comparison of  $E_i$  with  $E_s$ , followed a calculation of the smallest critical strain,  $\varepsilon_c$ , to initiate wrinkling. In this study, both the interface layer and the top solid film are stiffer than the substrate,  $E_s < (E_f, E_i)$ , therefore, the stiffness of the interface layer practically contributes to the stiffness of the top solid film and wrinkles together with the top film as a composite layer. For this reason, the interface layer and the top solid thin film are treated as a composite layer and are included in the problem solution with the effective stiffness of the composite layer. Following the solution by Lejeune et al [77] for an isotropic trilayer system under uniaxial compression, the governing differential Equation (3.1) can be solved by modeling the top two layers as a composite layer, namely the stiffness of the interface material contributes to the stiffness of the top solid film [77]:

$$D_{c,1} \frac{d^4 w}{dx^4} - hb\sigma_{xx} \frac{d^2 w}{dx^2} = qb \quad (3.4),$$

where  $h=t_i+t_f$  is the total thickness of the top film and the interface layer,  $D_{c,1}$  is the flexural rigidity of the composite layer, calculated as the sum of the individual flexural rigidities of the top film and the interface layer as:

$$D_{c,1} = E_i^* I_i + E_f^* I_f = \frac{bh^3}{12} E_c \quad (3.5),$$

where  $I_i$  and  $I_f$  are the moment of inertia of interface layer and the top film, respectively, calculated after finding the bending neutral axis of the composite layer,  $Z$ , as:

$$I_i = b \int_0^{t_i} (z - Z)^2 dz \quad (3.6a).$$

and

$$I_f = b \int_{t_i}^{t_i+t_f} (z - Z)^2 dz \quad (3.6b).$$

and  $E_c$  is the effective bending modulus of the composite layer, which can be calculated via the second equality in Equation (3.5). Similarly, the critical wavenumber,  $n_{cr}$ , for which wrinkling is initiated can be found by minimizing  $\sigma_{xx}$  with respect to  $n$  in Equation (3.4). The solution for  $\varepsilon_c$ ,  $\lambda$ , and  $w_0$ , is given by Equations (A8), (A9), and (A6), respectively. Similarly to a two-layer system,  $\varepsilon_c$  is related to the applied strain,  $\varepsilon$ , through Equation (3.3). In this solution, all three layers wrinkle, as determined by the simplified model selection procedure described in Lejeune et al. [77] for  $E_s < E_f$ ,  $E_i$  and the smallest critical strain for wrinkling initiation,  $\varepsilon_c$ , calculated by Equation (A9).

### 3.2.2 Modeling the Wrinkling Behavior with an Orthotropic Layer

The solution for wrinkling of a three-layer system described in the previous Section was developed for isotropic materials. GLAD can also be used to fabricate orthotropic films comprised of nanochevrons. A wrinkle model for an orthotropic solid layer on an isotropic substrate has been derived for a two-layer system by Yin et al. [13] through the Föppl–von Kármán governing equation, Equation (3.1). Based on their work, Equation (3.1) could be used to describe the deflection of a two-layer system comprised of an isotropic substrate and an orthotropic top film under plane stress conditions. In this

case, the flexural rigidities,  $D_1$  and  $D_2$ , of the orthotropic layer in  $x$  and  $y$  directions, respectively, are given by:

$$D_1 = E_{f,1}^* I_{f,1} \quad (3.7),$$

and

$$D_2 = E_{f,2}^* I_{f,2} \quad (3.7b),$$

where  $E_{f,1}$  and  $E_{f,2}$  are the elastic moduli of the top film in  $x$  and  $y$  directions,  $I_{f,1}$  and  $I_{f,2}$  are the moment of inertia of the top film in  $x$  and  $y$  directions. Using Equations (3.8), and later Equations (3.9) and (3.13), Yin et al. [13] derived a solution, Equations (3.14)-(3.15), for a two-layer system comprised of an orthotropic film on an isotropic substrate. In this formulation, similarly to the Föppl–von Kármán theory for an isotropic material system described by Equation (3.1), the in-plane shear traction, in-plane displacement, and the bending moment caused by the in-plane shear traction are neglected.

In the present work, Equation (3.1) was utilized to describe the three-layer system in Figure 3.8(c) by treating the orthotropic interface layer and the isotropic top solid layer as one composite layer. This composite layer is not orthotropic, because it lacks symmetry along the  $z$ -axis. The lack of an  $x$ - $y$  plane of symmetry would lead to an out-of-plane curvature during compression, which is mediated by the large thickness of the PDMS film and does not affect the formation of wrinkling. Hence, to simplify the analysis, the composite layer was assumed to be “in-plane orthotropic”. The approach by Lejeune et al. [77] was adopted to calculate the stiffness and the flexural rigidity of the composite layer,  $C_{ij}$  and  $D_{ci}$ , respectively. In this approach, for example,  $D_{c,1}$  replaces  $D_1$  in Equation (3.1). In the three-layer system, both the orthotropic interface layer and the isotropic top film contribute to the wrinkle behavior since both layers are stiffer than the substrate. Therefore, a 2D stiffness matrix is used to represent the composite of the two layers:

$$\begin{bmatrix} \sigma_{xx} \\ \sigma_{yy} \\ \sigma_{xy} \end{bmatrix} = \begin{bmatrix} C_{11} & C_{12} & 0 \\ C_{21} & C_{22} & 0 \\ 0 & 0 & 2C_{66} \end{bmatrix} \begin{bmatrix} \varepsilon_{xx} \\ \varepsilon_{yy} \\ \varepsilon_{xy} \end{bmatrix} \quad (3.8),$$

where  $C_{12} = C_{21} = \nu_{c,12}C_{11}$  and  $\sigma_{ij}$  and  $\varepsilon_{ij}$  are the in-plane stress and strain in the composite layer.  $C_{11}$  and  $C_{22}$  are the stiffness of the composite layer under uniaxial tension/compression in  $x$  and  $y$  direction, respectively, and  $\nu_{c,12}$  and  $C_{66}$  are the Poisson's ratio and the shear modulus of the composite layer. We identify the material axes of the interface layer with the  $x$  and  $y$  axes, namely the principal material axis of the nanochvron interface layer is aligned with the  $x$ -axis, Figure 3.8(c).  $C_{11}$ ,  $C_{22}$ , and  $\nu_{12}$  can be calculated by using the rule of mixtures and considering isostrain condition for the top film and the interface layer [77]:

$$C_{11} = E_f^* \frac{t_f}{t_f + t_i} + E_{i,1}^* \frac{t_i}{t_f + t_i} \quad (3.9a),$$

$$C_{22} = E_f^* \frac{t_f}{t_f + t_i} + E_{i,2}^* \frac{t_i}{t_f + t_i} \quad (3.9b),$$

$$\nu_{c,12} = \nu_{f,12} \frac{t_f}{t_f + t_i} + \nu_{i,12} \frac{t_i}{t_f + t_i} \quad (3.9c),$$

where  $E^* = E/1-\nu^2$ , e.g.  $E_{i,1}^* = E_{i,1}/1-\nu_{i,12}^2$ .  $E_{i,1}$  and  $E_{i,2}$  are the effective elastic moduli of the interface layer in  $x$  and  $y$  directions, respectively, and  $\nu_{f,12}$  and  $\nu_{i,12}$  are Poisson's ratios of top film and the interface layer, respectively. Both  $E_{i,1}$  and  $E_{i,2}$  are unknown and will be obtained from the experimental wrinkle patterns. Towards this goal, the solution approach by Lejeune et al. [77], as described in Section 3.2.1, was utilized to find  $E_{i,1}$  and  $E_{i,2}$ , which then can be used to calculate  $C_{11}$  and  $C_{22}$  since both the interface layer and the top solid film are stiffer than the substrate. When the composite layer is subjected to uniaxial compression in  $x$  or  $y$  direction, only its stiffness  $C_{11}$  or  $C_{22}$ , and the flexural rigidity  $D_{c,1}$  or  $D_{c,2}$ , respectively, have an effect on the material response, because the material axes are aligned with the  $x$  and  $y$  coordinates. Hence, the solution approach by Lejeune et al. [77] could be used to calculate the flexural rigidity of the composite layer

in  $x$  and  $y$  directions,  $D_{c,1}$  and  $D_{c,2}$ , respectively. In this solution approach, the flexural rigidity of the composite layer is the sum of the individual flexural rigidities of the top film and the interface layer:

$$D_{c,1} = E_{i,1}^* I_{i,1} + E_f^* I_{f,1} = \frac{bh^3}{12} E_{c,1} \quad (3.10a),$$

$$D_{c,2} = E_{i,2}^* I_{i,2} + E_f^* I_{f,2} = \frac{bh^3}{12} E_{c,2} \quad (3.10b),$$

where the subscripts 1 and 2 correspond to the  $x$  and  $y$  axes,  $I_i$  and  $I_f$  are the moment of inertia of the interface layer and the top film, respectively, which can be calculated through Equations (3.6a) and (3.6b), and  $E_{c,1}$  and  $E_{c,2}$  are the effective bending moduli of the composite layer in  $x$  and  $y$  direction, respectively. In addition, the torsional rigidity of the composite layer,  $D_{c,3}$ , is given by: [96]:

$$D_{c,3} = \frac{bh^3}{3} G_{c,12} \quad (3.11),$$

where  $G_{c,12}$  is effective in-plane shear modulus of the composite layer. After calibrating  $E_{i,1}$ , and  $E_{i,2}$  experimentally,  $C_{11}$ ,  $C_{22}$ , and  $\nu_{c,12}$  can be calculated via Equations (3.9a)-(3.9c) and  $C_{12}$  via the condition  $C_{12} = C_{21} = \nu_{c,12} C_{11}$ . Finally,  $G_{c,12}$  and  $C_{66}$  can be calibrated experimentally after  $D_{c,1}$ ,  $D_{c,2}$ ,  $C_{11}$ ,  $C_{22}$ , and  $C_{12}$  are known, as described at the end of this Section.

The material axes and the directions of  $\sigma_{ij}$  and  $\varepsilon_{ij}$  in Equation (3.8) are aligned with the  $x$  and  $y$  axes. If the principal stresses,  $\sigma_1$  and  $\sigma_2$  do not align with the material axes,  $\sigma_{ij}$  can be transformed via [99]:

$$\begin{bmatrix} \sigma_{xx} \\ \sigma_{yy} \\ \sigma_{xy} \end{bmatrix} = \begin{bmatrix} \cos^2 \theta_p & \sin^2 \theta_p & -\sin 2\theta_p \\ \sin^2 \theta_p & \cos^2 \theta_p & \sin 2\theta_p \\ \sin \theta_p \cos \theta_p & -\sin \theta_p \cos \theta_p & \cos 2\theta_p \end{bmatrix} \begin{bmatrix} \sigma_1 \\ \sigma_2 \\ 0 \end{bmatrix} \quad (3.12),$$

where  $\theta_p$  is the principal stress direction with respect to the principal material axis that is identified with the  $x$ -axis in Figure 3.8(c). A uniaxial stress results in a wrinkle pattern in the form of stripes, and the deflection  $w(x,y)$  can be described by [13]:

$$w(x, y) = w_o \cos[n(x\cos\theta + y\sin\theta)] \quad (3.13),$$

where  $\theta$  is the wrinkle direction that is defined to be perpendicular to the stripes of the wrinkle pattern and is measured relative to the  $x$ -axis, Figure 3.8(c). By inserting Equations (3.10)-(3.13) into Equation (3.1), the principal stress can be written as [13]:

$$\sigma_1 = -\frac{\frac{E_s^*}{2} + \frac{(nh)^3 E_\theta}{12}}{(1 - (1 - \zeta) \sin^2(\theta - \theta_p))nh} \quad (3.14),$$

where  $\zeta = \sigma_1/\sigma_2$  is the stress biaxiality and  $E_\theta$  is given by:

$$E_\theta = 12(D_{c,1} \cos^4 \theta + D_{c,2} \sin^4 \theta + (2D_{c,1} + D_{c,3}/4) \sin^2 \theta \cos^2 \theta)/b/h^3 \quad (3.15),$$

$E_\theta$  can be understood as the effective bending modulus at angle  $\theta$ , since  $E_\theta = E_{c,1}$  when  $\theta = 0^\circ$ .

The critical wavenumber,  $n_{cr}$ , and the corresponding wrinkle wavelength,  $\lambda$ , can be found by minimizing  $\sigma_1$  with respect to  $n$  as:

$$n_{cr} = \frac{1}{h} \left( \frac{3E_s^*}{E_\theta} \right)^{\frac{1}{3}} \quad (3.16a),$$

$$\lambda = \frac{2\pi}{n_{cr}} \quad (3.16b).$$

Likewise, the critical wrinkle direction,  $\theta_{cr}$ , can be found numerically by minimizing  $\sigma_1$  with respect to  $\theta$ , namely  $\theta = \theta_{cr}$  when wrinkling begins. From Equations

(3.15) and (3.16), it can be shown that the flexural and torsional rigidities of the composite layer determine the wrinkle wavelength and wrinkle direction. The principal stress  $\sigma_l$  can be related to the applied strain,  $\varepsilon$ , via Equations (3.8) and (3.12) [100]:

$$\sigma_1 = (\cos^4 \theta_p C_{11} + \sin^4 \theta_p C_{22} + 2 \cos^2 \theta_p \sin^2 \theta_p C_{12} + 4 \cos^2 \theta_p \sin^2 \theta_p (C_{66})) \varepsilon \quad (3.17).$$

The critical strain,  $\varepsilon_c$ , can be found by inserting Equation (3.16a) and Equation (3.17) into Equation (3.14). According to Equation (3.15), the torsional rigidity of the composite layer,  $D_{c,3}$ , has an effect on the material response when the principal stress is not aligned with a material axis. In this case,  $G_{c,12}$  can be found through Equations (3.11) and (3.14)-(3.16) by measuring the wrinkle wavelength and angle. Similarly, once  $G_{c,12}$ ,  $C_{11}$ ,  $C_{12}$ , and  $C_{22}$  have been determined,  $C_{66}$  can be calculated through Equations (3.14)-(3.17) by using the experimentally obtained value of  $\varepsilon_c$ , and the measured wrinkle wavelength and angle. Furthermore, by using Equation (A12),  $\varepsilon_c$  can be related to  $\varepsilon$  through the wrinkle wavelength along the principal stress direction,  $\lambda_l$ , and the wrinkle amplitude, similarly to Equation (3.3), as:

$$\varepsilon_c = \varepsilon - \frac{\pi^2 w_0^2}{\lambda_1^2} \quad (3.18).$$

### 3.3 Effect of Isotropic Interface Material on Wrinkle Pattern

In the case of an all-isotropic material system, Figure 3.8(b), solid Cu films with 0.5  $\mu\text{m}$  and 2.5  $\mu\text{m}$  thickness were deposited at 0° and 20° e-beam incidence, as well as 2.0- $\mu\text{m}$  nanospring films with circular coils and 250-nm or 500-nm pitch, which were capped with a 0.5- $\mu\text{m}$  thick solid layer deposited at 20° e-beam incidence. The Young's modulus of PDMS serving as the substrate was measured as 8±0.02 MPa (Figure A.1).

The Poisson's ratios of Cu and PDMS were assumed as 0.35 and 0.499, respectively [101-104]. The Poisson's ratio of the Cu nanospring and the nanochevron films was assumed to be zero due to the discrete nature of the nanostructures comprising the films.

All PDMS films listed in Tables 3.2 and 3.3 were first subjected to 10% uniaxial tensile strain with the aid of the device shown in Figure 2.4, before deposition or surface treatment took place. After completion of the deposition process, the applied tensile strain was gradually reduced in 0.25% increments to induce compressive strain to the top Cu layer. The PDMS specimens with solid Cu films deposited at 0° e-beam incidence served as reference specimens to validate the experimental approach by calculating the modulus of bulk Cu from the geometric parameters of the wrinkle pattern, which were obtained via a 3D laser scanning confocal microscope, e.g. 3.10(a). Consecutive confocal microscopy images similar to Figure 3.9(a) were obtained while unloading the PDMS substrate in 0.25% strain increments and cross-sections along the direction of the applied force in Figure 3.9(a) were extracted to measure the wrinkle wavelength and amplitude. A sequence of such cross-sections is shown in Figure 3.9(b) for Specimen #1 in Table 3.2. For two-layer specimens comprised of a PDMS substrate and a solid Cu solid film, Equations (A3a) and (A3b) were used to extract the in-plane modulus of the Cu film from the measured  $\lambda$ . The average wavelength of the two types of specimens with a solid Cu film layer with thickness 0.53  $\mu\text{m}$  and 2.5  $\mu\text{m}$ , Specimens #3 and #4 in Table 3.3, was  $\lambda = 53.9 \pm 0.5 \mu\text{m}$  and  $\lambda = 255.2 \pm 2 \mu\text{m}$ , respectively, Figure 3.9(c). For 0.53- $\mu\text{m}$  and 2.5- $\mu\text{m}$  solid Cu films fabricated at 0° e-beam incidence the in-plane modulus was derived from experimental wrinkle data as  $119 \pm 3 \text{ GPa}$  and  $120 \pm 3 \text{ GPa}$ , respectively, which is in agreement with literature reports for solid Cu films and provides validation of the accuracy of the experimental procedure utilized in this study [101,105]. For solid Cu films deposited on PDMS at 20° e-beam incidence, Specimens #5 and #6 in Table 3.3, the measured wrinkle wavelength was  $\lambda = 47.1 \pm 1 \mu\text{m}$  and  $\lambda = 235.1 \pm 3 \mu\text{m}$  for 0.5- $\mu\text{m}$  and 2.5- $\mu\text{m}$  thick films, respectively, Figure 3.9(c). Consistently for both 0.5- $\mu\text{m}$  and 2.5- $\mu\text{m}$  thick films, the extracted in-plane compressive modulus averaged  $94 \pm 6 \text{ GPa}$ . Such a reduction in the in-plane modulus of the solid Cu films with e-beam incidence angle is expected, as larger deposition angles gradually result in less coherent Cu films eventually

forming isolated islands (which are taken advantage of to grow nanosprings and nanochevrons) and, therefore, these films have a reduced effective in-plane modulus [35,36]. Finally,  $\varepsilon_c$  was extracted from the applied strain and the measured wrinkle amplitude and wavelength, by applying Equation (3.3), as the average value at different applied strains that are plotted in Figure 3.10(a). For Cu films deposited at  $0^\circ$  e-beam incidence angle,  $\varepsilon_c = 0.097\%$ , whereas for films deposited at  $20^\circ$ ,  $\varepsilon_c = 0.11\%$ . The higher  $\varepsilon_c$  for films deposited at  $20^\circ$  e-beam incidence is consistent with the lower in-plane modulus of those films compared to the Cu films deposited at normal e-beam incidence.

As shown in Figure 3.9(c), when a Cu nanospring interface layer is inserted between the PDMS substrate and the Cu solid film,  $\lambda$  is reduced from  $235.1 \pm 3 \mu\text{m}$  to  $73.1 \pm 0.4 \mu\text{m}$  if  $2 \mu\text{m}$  of the  $2.5\text{-}\mu\text{m}$  total film thickness are replaced by a Cu nanospring film with  $0.5\text{-}\mu\text{m}$  pitch (Specimen #2). Likewise,  $\lambda$  is further reduced to  $65.2 \pm 0.3 \mu\text{m}$  for a Cu interface of nanosprings with  $0.25\text{-}\mu\text{m}$  pitch (Specimen #1). Using Equations (A8a) and (A8b), the effective in-plane compressive modulus,  $E_i$ , of the Cu nanospring films with  $0.25\text{-}\mu\text{m}$  and  $0.5\text{-}\mu\text{m}$  pitch was calculated as  $500 \pm 21 \text{ MPa}$  and  $830 \pm 20 \text{ MPa}$ , respectively. This is strictly the effective compressive modulus of the nanostructured GLAD films in the particular range of compressive strains, and is due to the mechanical interactions between the compressed nanostructures in the GLAD films. As shown in Figures 3.9(b) and 3.13(b), the wrinkle wavelength remained constant during incremental compression by  $0.25\%$ , which, by virtue of Equations (A3a) and (A3b), shows that the interface layer modulus remained constant during the entire compression and wrinkling process. The larger wrinkle wavelength in Specimen #2 compared to Specimen #1, Figures 3.7(b) and 3.7(a), respectively, stems from the stronger interaction between the nanosprings in Specimen #2, thus leading to larger effective in-plane compressive modulus and, in turn, larger  $\varepsilon_c$  values ( $0.168\%$  vs.  $0.156\%$  for Specimens #2 and #1, respectively) as computed via Equation (3.3). Graphically, the experimental data plots in Figure 3.10(a) show that a compliant interface layer could be used as an effective means to tune  $\varepsilon_c$ . Tables 3.2 and 3.3 provide a summary of all experimental parameters and the measured and extracted quantities for the test specimens discussed in this Section.

**Table 3.2** PDMS specimens with a 2.0- $\mu\text{m}$  thick Cu nanospring interface layer followed by a 0.5- $\mu\text{m}$  solid Cu film deposited at 20° (2.5  $\mu\text{m}$  total thickness).

Specimen #	Deposition angle (°)	Pitch ( $\mu\text{m}$ )	Wrinkle wavelength ( $\mu\text{m}$ )	In-plane compressive modulus of interface (MPa)	Critical strain (%)
1	86	0.25	65.2 $\pm$ 0.3	500 $\pm$ 21	0.156
2	86	0.5	73.1 $\pm$ 0.4	830 $\pm$ 20	0.168

**Table 3.3** PDMS specimens with solid Cu films deposited at 0° and 20° e-beam incidence.

Specimen #	Deposition angle (°)	Thickness ( $\mu\text{m}$ )	Wrinkle wavelength ( $\mu\text{m}$ )	Elastic modulus (MPa)	Critical strain (%)
3	0	0.53	53.9 $\pm$ 0.5	119 $\pm$ 3	0.097
4	0	2.5	255.2 $\pm$ 2	120 $\pm$ 3	0.096
5	20	0.5	47.1 $\pm$ 1	94 $\pm$ 6	0.115
6	20	2.5	235.1 $\pm$ 3	94 $\pm$ 4	0.114

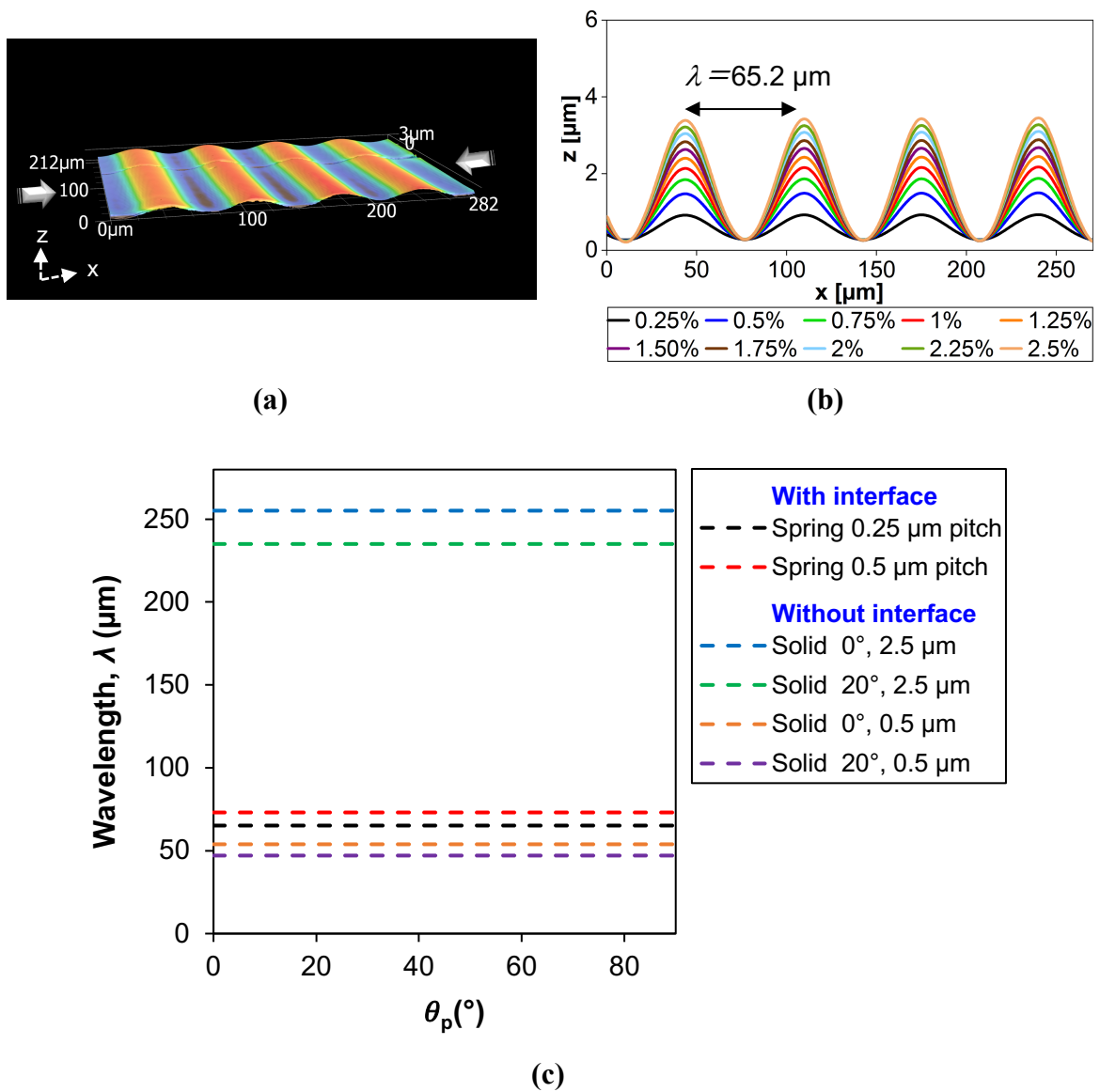
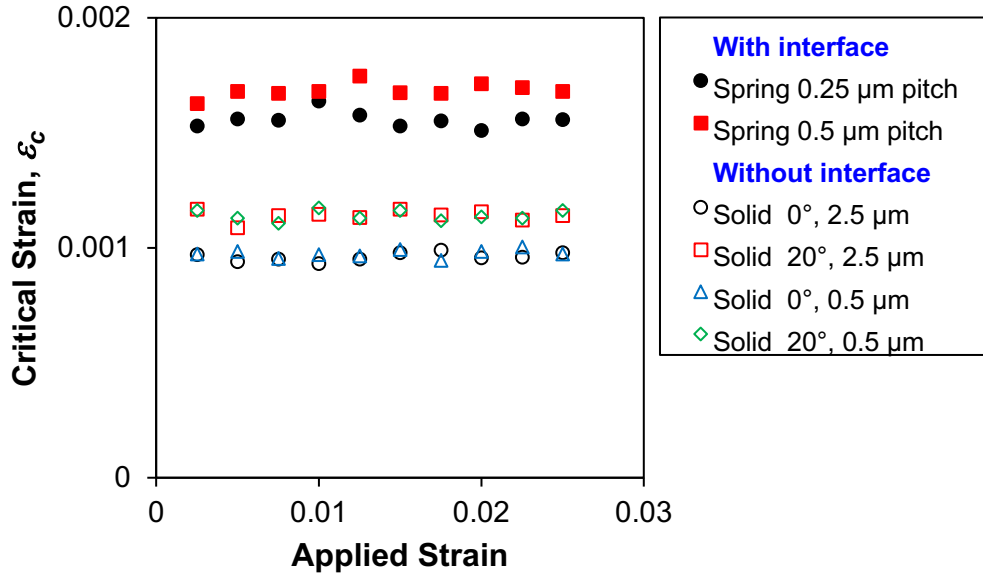
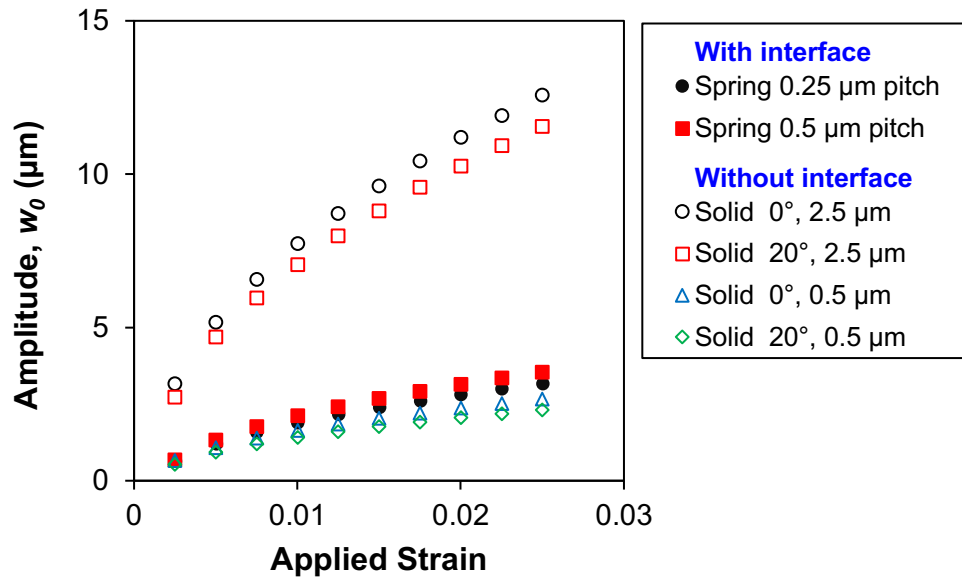


**Figure 3.9** (a) 3D topography of a PDMS specimen with a 0.5-μm solid Cu film on a 2.0-μm interface layer comprised of Cu nanosprings with 0.25-μm pitch (Specimen #1 in Table 3.2), obtained with a 3D laser scanning confocal microscope. The 3D topography corresponds to 1% compressive strain. The arrows point to the direction of uniaxial compression. (b) Sequence of wrinkle profiles obtained while unloading Specimen #1 in 0.25% strain increments. (c) Measured wrinkle wavelength of the Cu films listed in Tables 3.2 and 3.3, with and without a nanospring interface layer.



(a)



(b)

**Figure 3.10** (a) Critical strain calculated from measured wrinkle amplitude and wavelength values, and (b) wrinkle amplitude of Cu solid films with and without an interface layer. Conversion of part of the solid Cu film into a Cu nanospring film greatly reduces the wrinkle amplitude. See Tables 3.2 and 3.3 for specimen details.

Based on the results shown in Figure 3.9(c), it is deduced that  $\lambda$  could be **(a)** increased by adding a compliant interface layer while maintaining the thickness of the 0.5- $\mu\text{m}$  thick solid Cu film (Specimens #3, #5 vs. Specimens #1, #2) that may be serving as the electrical or data conduit on a flexible electronics substrate, or **(b)** significantly reduced by substituting 2  $\mu\text{m}$  of a 2.5- $\mu\text{m}$  thick solid Cu layer (Specimens #4, #6) with a Cu nanospring film, while still maintaining high electrical conductivity through a 0.5- $\mu\text{m}$  top solid Cu layer. In the latter case, large portion of the original solid layer becomes very compliant and  $\lambda$  decreases by about 70%, while  $\varepsilon_c$  increases by about 50%, Figure 3.10(a). Thus, the insertion of a compliant interface layer provides an additional means to control the wrinkle wavelength and amplitude, Figures 3.9(c) and 3.10(b). In general, without modifying the composition or thickness of the top solid film in a two-layer system,  $w_o$  can only be tuned by the applied strain, as inferred from Equation (A6). For a given applied compressive strain to a two-layer system,  $\lambda$  is determined by the material properties of the substrate and the top film, Equation (A3a), and  $w_o$  is controlled by  $\varepsilon_c$  and  $\lambda$ , Equation (A6). On the other hand, in a three-layer system,  $w_o$  could be further controlled by the compliant interface layer, Figure 3.10(b). For instance, under 1% uniaxial compressive strain,  $w_o$  is reduced by a factor of 3.6 (7  $\mu\text{m}$  vs. 1.9  $\mu\text{m}$ ) when 2.0  $\mu\text{m}$  of the 2.5- $\mu\text{m}$  thick Cu layer are substituted by an interface layer of Cu nanosprings with 0.25- $\mu\text{m}$  pitch (Specimen #1 vs. #6). Notably, for a given applied strain, the compliance of the interface reduced the physical length scale of the wrinkle pattern while maintaining the same aspect ratio  $w_o/\lambda$  (0.03) by reducing both  $\lambda$  (from 235.1  $\mu\text{m}$  to 65.2  $\mu\text{m}$ ) and  $w_o$  (from 7  $\mu\text{m}$  to 1.9  $\mu\text{m}$ ) by the same factor of 3.6. On the other hand, the insertion of a 2.0- $\mu\text{m}$  thick interface of Cu nanosprings with 0.25- $\mu\text{m}$  pitch (Specimen #1) to an originally 0.5- $\mu\text{m}$  thick Cu film on a PDMS substrate (Specimen #5) increased the physical length scale of the wrinkle pattern while maintaining the same value of  $w_o/\lambda$  (0.03) by increasing both  $\lambda$  (from 47.1  $\mu\text{m}$  to 65.2  $\mu\text{m}$ ) and  $w_o$  (from 1.4  $\mu\text{m}$  to 1.9  $\mu\text{m}$ ) by the same factor of 1.4. For solid Cu films without an interface, both  $\lambda$  and  $w_o$  increase with Cu film thickness, as deduced from Equations (A3b) and (A6), respectively, and, as commonly done in prior works, the physical length scale of a wrinkle pattern is tuned by modifying the top film thickness [27]. Therefore, the compliance of interface layer

provides additional means to control the physical length scale of the wrinkle pattern without modifying the total thickness  $t_i+t_f$ .

### 3.4 Control of Wrinkling through an Anisotropic Interface

In the case of an isotropic interface of nanosprings discussed in Section 3.3, the wrinkle direction coincided with the direction of uniaxial compressive stress, e.g. Figure 3.9(a). In a two-layer system comprised of an orthotropic film and an isotropic substrate, the orientation of the wrinkle pattern is dictated by the principal stresses *and* the material anisotropy [13]. However, due to manufacturing constraints, the vast majority of solid films deposited on substrates are isotropic. This practical material constraint can be eliminated by introducing an anisotropic interface layer to control the wrinkle direction. Towards this goal, PDMS specimens with an orthotropic Cu interface layer comprised of nanochevrons were fabricated via GLAD, Figures 3.7(c-i), with their details provided in Table 3.4. These specimens were uniaxially loaded at different angles with respect to the principal material axis with the aid of the stretching device shown in Figure 2.4 and the geometrical definitions in Figures 3.6 and 3.7(j).

As described in Section 3.2.2, the analytical solution to this problem requires the in-plane moduli of the anisotropic interface layer, i.e.  $E_{i,1}$  and  $E_{i,2}$ . In order to simplify the solution to this problem, the orthotropic interface layer and the isotropic solid cap layer were treated as a single composite layer, forming a bilayer system with the isotropic PDMS substrate. Then, Equation (3.1) can be used to solve this problem.  $E_{i,1}$  and  $E_{i,2}$  were calculated as follows: First uniaxial compression was applied in  $0^\circ$  and  $90^\circ$  directions with respect to the principal material axis. For Specimens #10 and #13 with  $0.5\text{-}\mu\text{m}$  pitch,  $\lambda$  was measured to be  $70.4\pm 0.3\ \mu\text{m}$  and  $50.7\pm 0.1\ \mu\text{m}$ , respectively, Figure 3.11. Then, the effective in-plane compressive modulus,  $E_i$ , of the nanochevron interface layers in Specimens #10 and #13 was extracted through Equations (3.10a), (3.15), (3.16a) and (3.16b) as  $710\pm 10\ \text{MPa}$  and  $75.1\pm 2\ \text{MPa}$ , respectively. The lower modulus in the  $90^\circ$  direction is due to the larger separation between individual nanochevrons in this direction as also deduced by comparison of Figures 3.7(f) and 3.7(i). The critical strain for

**Table 3.4** PDMS specimens with a 2.0- $\mu\text{m}$  thick interface layer comprised of nanochevrons, followed by a 0.5- $\mu\text{m}$  solid film deposited at 20° angle (2.5- $\mu\text{m}$  total thickness).

Specimen #	7	8	9	10	11	12	13
Pitch ( $\mu\text{m}$ )	0.25	0.25	0.25	0.5	0.5	0.5	0.5
$\theta_p$ (°)	0	45	90	0	20	45	90
$\lambda$ ( $\mu\text{m}$ )	63.1 $\pm$ 0.2	56.2 $\pm$ 0.1	49.5 $\pm$ 0.1	70.4 $\pm$ 0.3	68.1 $\pm$ 0.2	59.3 $\pm$ 0.2	50.7 $\pm$ 0.1
In-plane compressive modulus of interface (MPa)	$E_{i,1}$ = 420 $\pm$ 5		$E_{i,2}$ = 50.1 $\pm$ 3	$E_{i,1}$ = 710 $\pm$ 10			$E_{i,2}$ = 75.1 $\pm$ 2
$\varepsilon_c$ (%)	0.147	0.134	0.117	0.163	0.158	0.139	0.12
Wrinkle direction w.r.t principal stress direction (°)	0	7.1 $\pm$ 0.2	0	0	4.5 $\pm$ 0.1	9.6 $\pm$ 0.3	0

Specimens #10 and #13 was calculated as  $\varepsilon_c = 0.163\%$  and  $\varepsilon_c = 0.12\%$ , respectively, by applying Equation (3.3) to the experimental data and averaging for different applied strains, Figure 3.12(a). Similar testing procedures applied to Specimens #7 and #9 with interface layers comprised of nanochevrons with 0.25- $\mu\text{m}$  pitch, yielded  $\lambda = 63.1\pm 0.2 \mu\text{m}$  and  $\lambda = 49.5\pm 0.1 \mu\text{m}$ , respectively, which were used to extract the effective in-plane compressive modulus,  $E_i$ , in 0° and 90° directions as 420 $\pm$ 5 MPa and 50.1 $\pm$ 3 MPa, respectively. The corresponding critical strains were calculated as  $\varepsilon_c = 0.147\%$  and  $\varepsilon_c = 0.117\%$  through Equation (3.3) and the experimental measurements. Similarly to

isotropic nanospring films, nanochevron films with smaller pitch (0.25  $\mu\text{m}$ ) had lower  $E_i$  than nanochevron films with 0.5  $\mu\text{m}$  pitch. Finally, according to the  $w_o$  vs.  $\varepsilon$  plot in Figure 3.12(b), films of Cu nanochevrons with 0.25- $\mu\text{m}$  pitch, Specimen #9, possessed the lowest  $w_o$  due to the smallest  $E_i$ , also leading to the smallest  $\lambda$ , when the principal stress was oriented at  $90^\circ$  with the respect to the principal material axis. For the four specimen cases (#7, #9, #10, #13) discussed so far in this Section, the principal stress was applied at  $0^\circ$  and  $90^\circ$  with respect to the principal material axis and the wrinkle direction was always parallel to the principal stress direction.

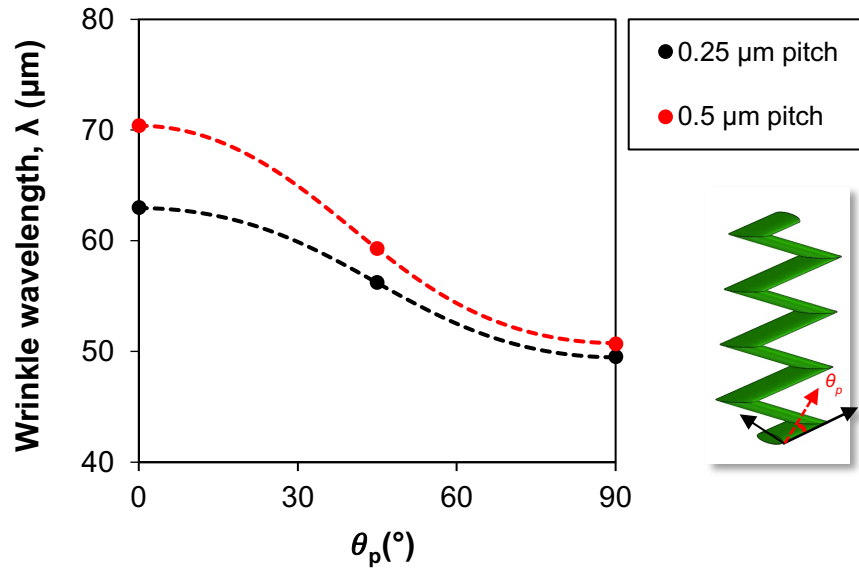
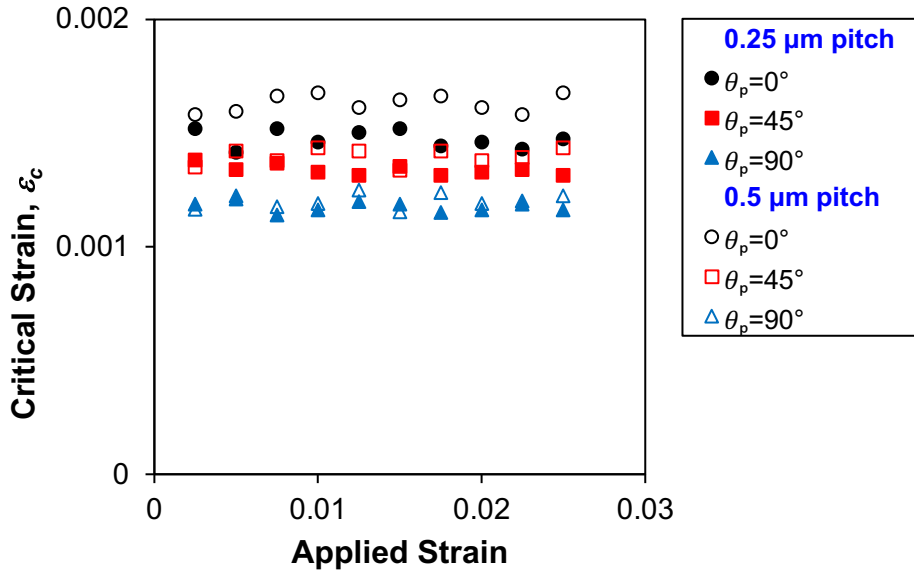
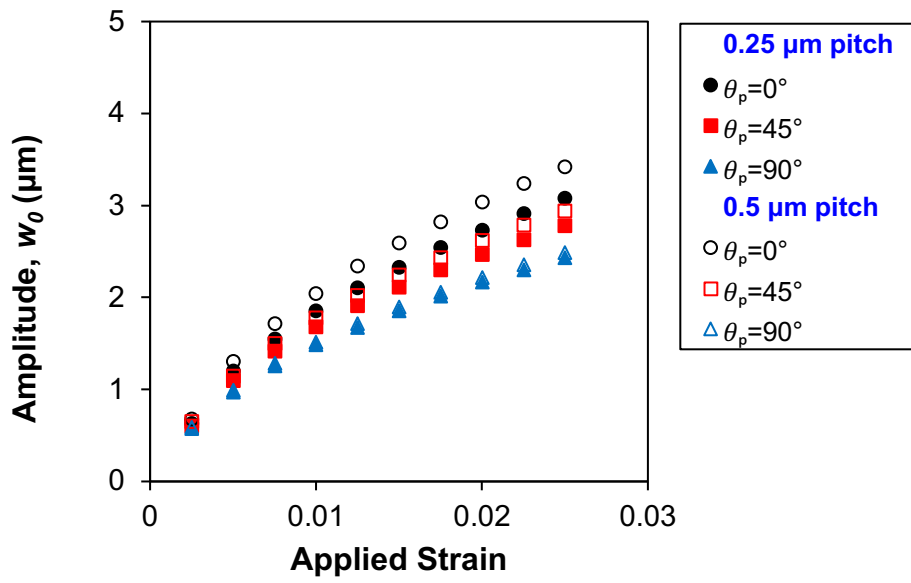


**Figure 3.11** Wrinkle wavelength of specimens with nanochevron interfaces, Table 3.4, as a function of principal stress direction, measured with respect to the principal material axis,  $\theta_p$ . The principal material axis of the chevrons is aligned with the  $x$ -axis as shown in the inset. The dashed lines show the calculation of  $\lambda$  through Equations (3.16a) and (3.16b) after calibration of the effective in-plane compressive modulus.

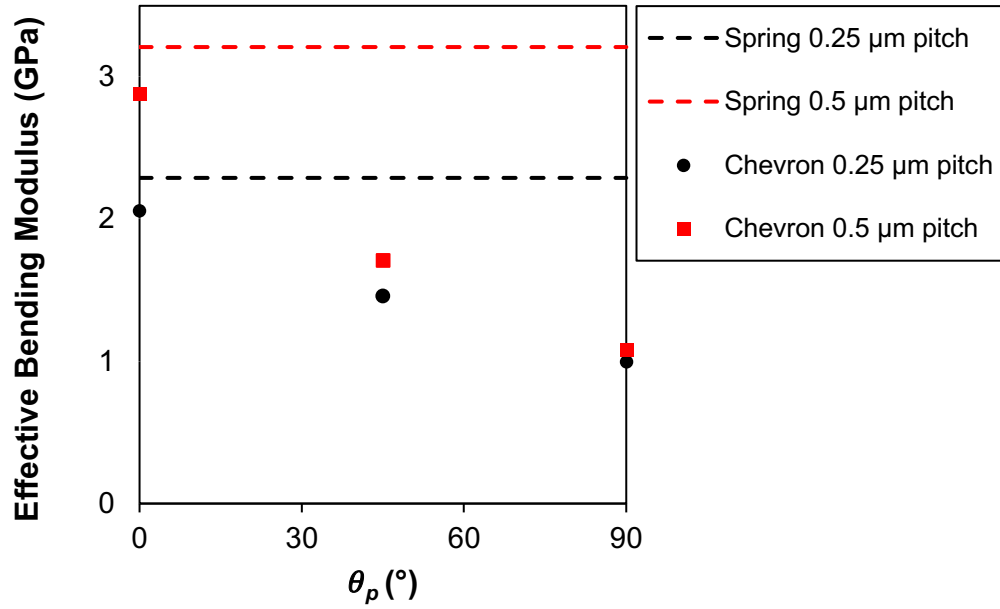


(a)



(b)

(Figure 3.12 continued)



(c)

**Figure 3.12 (a)** Critical wrinkling strain calculated from measurements of  $w_0$  and  $\lambda$  at different applied strain values, and **(b)** effect of applied strain on  $w_0$  in a three-layer system with Cu nanochevrons as the interface layer. **(c)** Effective bending modulus of composite films,  $E_c$ , as function of  $\theta_p$ . For reference, the effective bending modulus of the composite films comprised of isotropic nanospring interface is given by the dashed lines.

Based on the aforementioned measurements, the anisotropy ratio,  $E_{i,1}/E_{i,2}$ , of nanochevron interface films with 0.25- $\mu\text{m}$  and 0.5- $\mu\text{m}$  pitch is equal to 8.4 (420/50.1) and 9.5 (710/75.1), respectively. Higher values of  $E_{i,1}/E_{i,2}$  result in stronger anisotropy: By using Equations (3.10a) and (3.10b), the anisotropy ratio of the effective bending modulus of the combined Cu nanochevron/top solid films,  $E_{c,1}/E_{c,2}$ , was calculated as 2 and 2.7 for nanochevrons with 0.25- $\mu\text{m}$  and 0.5- $\mu\text{m}$  pitch, respectively, Figure 3.12(c). Higher ratios of  $E_{c,1}/E_{c,2}$  enable further control of the wrinkle direction. For instance, the projected wrinkling response for  $E_{c,1}/E_{c,2} = 5$  and  $E_{c,1}/E_{c,2} = 10$ , as calculated through Equations (3.14)-(3.16), is plotted in Figure 3.13.

Compression of PDMS specimens with nanochevron interfaces at  $\theta_p \neq 0^\circ$  and  $\theta_p \neq 90^\circ$  would result in wrinkles whose direction deviates from the principal stress

direction. The wrinkle topography of a specimen with  $\theta_p=45^\circ$ , as obtained with a 3D scanning laser confocal microscope, is shown in Figure 3.14(a). Similar 3D surface topographies were obtained while unloading the PDMS substrate in 0.25% strain increments, and the wrinkle profiles along the principal stress direction were extracted and shown in Figure 3.14(b). Experiments for  $\theta_p = 45^\circ$  resulted in  $\lambda = 56.2\pm 0.1 \mu\text{m}$  and  $\lambda = 59.3\pm 0.2 \mu\text{m}$  for 0.25- $\mu\text{m}$  and 0.5- $\mu\text{m}$  chevron pitch (Specimens #8 and #12), respectively, Figure 3.11. Note that these values for  $\lambda$  correspond to the wrinkle wavelength along the wrinkle direction. Importantly, for  $\theta_p = 45^\circ$  the wrinkle direction,  $\theta$ , deviated from the principal stress direction by  $\theta_{wp} = 7.1\pm 0.2^\circ$  and  $\theta_{wp} = 9.6\pm 0.3^\circ$ , respectively, Table 3.4, where  $\theta_{wp} = \theta - \theta_p$ . For the same principal value of  $\theta_p$ , the larger anisotropy ratio,  $E_{c,1}/E_{c,2}$ , of Specimen #12 resulted in larger  $\theta_{wp}$  compared to Specimen #8 as a result of the combined effect of principal stress and material anisotropy. In addition, Equations (3.11) and (3.14)-(3.16) provide the means to calculate the effective in-plane shear modulus of the composite Cu film,  $G_{c,12}$ , from measurements of  $\lambda$  and  $\theta$ . For composite Cu films comprised of a solid top film and an interface of nanochevrons with 0.25- $\mu\text{m}$  and 0.5- $\mu\text{m}$  pitch (Specimens #8 and #12),  $G_{c,12}$  was found to be equal to 762 $\pm$ 10 MPa and 930 $\pm$ 20 MPa, respectively.

Finally, the stiffness matrix of the composite layer (solid Cu film /nanochevron Cu film), Equation (3.8), can be constructed through Equations (3.9a)-(3.9c) once the effective in-plane compressive modulus of the interface layer,  $E_i$ , and its shear modulus,  $C_{66}$  have been found. With respect to the latter, the value of  $\varepsilon_c$ , calculated from experimental measurements for  $\theta_p = 45^\circ$  by using Equation (3.18), is entered into Equation (3.14)-(3.17) to calculate the in-plane shear modulus of the composite layer,  $C_{66}$ . The stiffness matrix of the composite Cu film comprised of Cu nanochevrons with 0.25- $\mu\text{m}$  pitch was then calculated as:

$$[C_{ij}] = \begin{bmatrix} 21.8 & 1.5 & 0 \\ 1.5 & 21.4 & 0 \\ 0 & 0 & 10.1 \end{bmatrix} \text{ GPa} \quad (3.19),$$

while for the composite Cu film comprised of Cu nanochevrons of 0.5- $\mu\text{m}$  pitch:

$$[C_{ij}] = \begin{bmatrix} 22 & 1.6 & 0 \\ 1.6 & 21.5 & 0 \\ 0 & 0 & 10.5 \end{bmatrix} \text{ GPa} \quad (3.20).$$

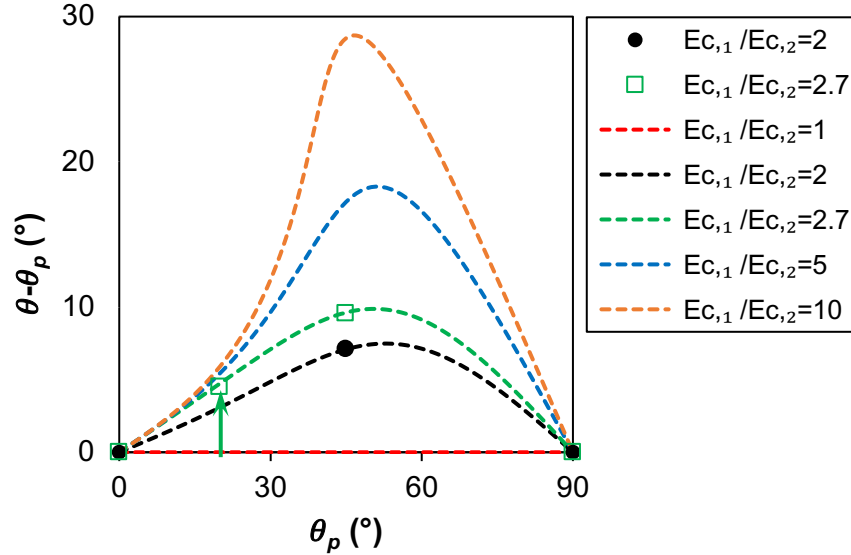


**Figure 3.13**  $\theta_{wp}$  vs.  $\theta_p$  for an isotropic interface of nanosprings ( $E_{c,1}/E_{c,2} = 1$ ), and orthotropic interfaces comprised of 2- $\mu\text{m}$  Cu nanochevrons with 0.25- $\mu\text{m}$  pitch ( $E_{c,1}/E_{c,2} = 2$ ) and 0.5- $\mu\text{m}$  pitch ( $E_{c,1}/E_{c,2} = 2.7$ ). The dashed lines are the calculation of  $\theta_{wp}$  through Equations (3.14)-(3.15) after calibration of the effective in-plane modulus of the nanochevrons. The curves for  $E_{c,1}/E_{c,2} = 5$  and  $E_{c,1}/E_{c,2} = 10$  were calculated by only increasing the value of  $E_{c,1}$ . The prediction of the calibrated model for  $\theta_p = 20^\circ$  agrees well with the experimental measurement (Specimen #11) pointed by the arrow.

The flexural and torsional rigidity of the composite layer, Equations (3.10a), (3.10b), and (3.11), can be input into Equations (3.14) and (3.15) to calculate  $\theta$ , which is measured relatively to the  $x$  axis. If an orthotropic interface is introduced,  $\theta$  will deviate from  $\theta_p$  depending on the anisotropy ratio of the effective bending modulus of the composite layer,  $E_{c,1}/E_{c,2}$ . Figure 3.13 shows several cases of  $\theta_{wp} = (\theta - \theta_p)$  vs.  $\theta_p$ . In the case of an isotropic composite layer  $E_{c,1}/E_{c,2} = 1$  and the wrinkle direction,  $\theta$ , is dictated only by  $\theta_p$ . The insertion of an orthotropic interface allowed for further tuning of the wrinkle direction that is determined by both the principal stress and the material

anisotropy. Under uniaxial loading,  $\theta$  deviated from  $\theta_p$  when the anisotropy ratio of the composite layer,  $E_{c,1}/E_{c,2} = 2$ , whereas  $\theta = \theta_p$  for an isotropic material. Similarly, when  $\theta_p$  is close to one of the material axes, namely  $\theta_p \approx 0^\circ$  or  $\theta_p \approx 90^\circ$ ,  $\theta$  is mainly dictated by  $\theta_p$  and the material anisotropy has a small effect on  $\theta$ . For the experimental case of  $E_{c,1}/E_{c,2} = 2.7$ ,  $\theta_{wp}$  assumes its largest value at  $\theta_p = 52^\circ$ . Although in the present study,  $E_{c,1}/E_{c,2} = 2.7$ , larger values of  $\theta_{wp}$  are possible for higher anisotropy ratios,  $E_{c,1}/E_{c,2}$ . As shown in Figure 3.13,  $\theta_{wp}$  was estimated to increase to as much as  $28.5^\circ$  for  $E_{c,1}/E_{c,2} = 10$ .

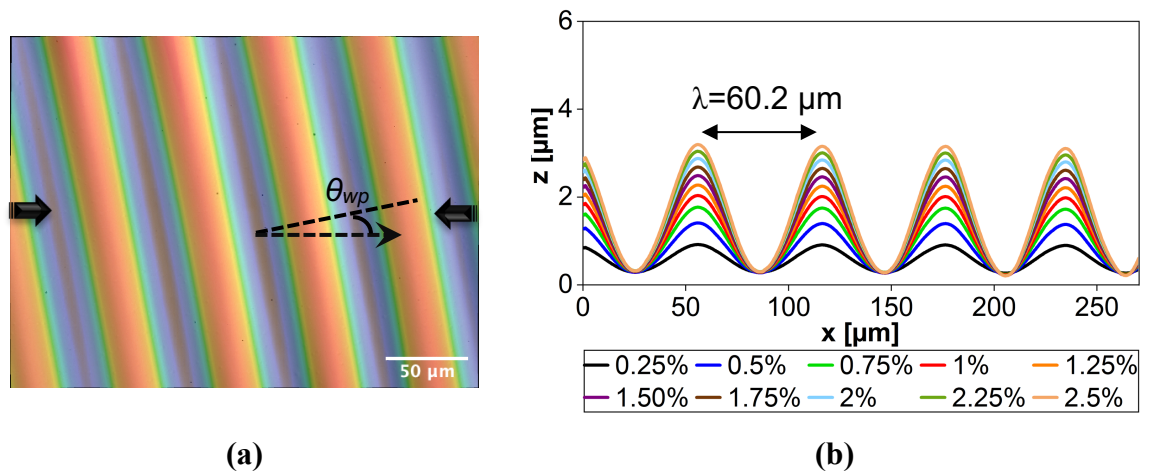


**Figure 3.14** (a) Topography and (b) wrinkle profile of 2.0- $\mu\text{m}$  thick Cu interface comprised of Cu nanochevrons with 0.5- $\mu\text{m}$  pitch with  $\theta_p = 45^\circ$  (Specimen #12). The two black arrows point to the principal stress direction.

Finally, a validation experiment was carried out with Specimen #11 which was comprised of a Cu nanochevron interface layer with 0.5- $\mu\text{m}$  pitch, subjected to compressive stress at  $\theta_p = 20^\circ$ . In this case,  $\theta_{wp}$  was measured to be  $4.5 \pm 0.1^\circ$  which compared well with the value of  $4.7^\circ$  that was predicted by the analytical model in Equation (3.14), by using the measured flexural and torsional rigidity of the composite layer, given in Equations (3.10a), (3.10b), and (3.11), Figure 3.13.

### 3.5 Conclusions

A compliant interface layer between a soft substrate and a stiff thin film was shown to provide effective control of the wrinkle wavelength, amplitude and direction. The GLAD method was utilized to fabricate isotropic (films of nanosprings) and orthotropic (films of nanochevrons) interface layers with control of the effective compressive film modulus through the pitch of the nanostructures. The compliant interface provided a novel means to modify the physical length scale of the wrinkle pattern while maintaining the same wrinkle amplitude/wavelength aspect ratio for the same applied strain. Orthotropic Cu nanochevron films with 0.25- $\mu\text{m}$  and 0.5- $\mu\text{m}$  pitch were shown to have substantial anisotropy ratios of 8.4 and 9.5, respectively, which were utilized to modify the wrinkle direction by as much as  $9.6 \pm 0.3^\circ$  with respect to principal stress direction. Modifications to the nanochevron pitch would further increase the anisotropy ratio and, thus, the wrinkle anisotropy. The prediction by an analytical model, calibrated with experimental measurements from the wrinkle patterns of three-layer material systems with an orthotropic interface, was in good agreement with the experiment.

An important novelty of the present work are the first of their kind measurements of the effective in-plane compressive Young's moduli of isotropic (nanospring) and orthotropic (nanochevron) GLAD films, which were shown to depend on the nanospring or nanochevron pitch that controlled the intertwining between individual nanostructures and, hence, their mechanical interactions. The Cu nanochevron films demonstrated a strong effect of material anisotropy on the directional modulus, with the effective in-plane compressive modulus measured to be  $710 \pm 10$  MPa and  $75.1 \pm 2$  MPa along the principal material directions.

# CHAPTER 4

## Strain Attenuation via Interface Engineering

In this Chapter, a comprehensive design approach is employed through a detailed multilayer elasticity model, originally developed by Li et al. [78], to calculate the coupled mechanical property and layer thickness design space of an interface material that could attenuate or completely eliminate the strain transfer from a stiff Carbon Fiber Reinforced Polymer (CFRP) laminate to a thin film PV module, while also maintaining the energy harvesting performance of the PV film at large substrate strains. Such an interface would also extend the maximum CFRP laminate strain before the functionality of the PV film begins to decline or microcracking occurs in the PV film. The strain attenuation achieved by PDMS as the interface layer and the performance evaluation of the PV film are determined experimentally. An analytical model developed by Li et al. [78] is extended for the case of an orthotropic substrate. All model parameters, including the properties of the anisotropic CFRP laminate, are derived and provided in Appendices B1 and B2. The combined effect of thickness and elastic properties of the material system is quantified in the form of strain attenuation maps, and the results of a comprehensive experimental study are discussed and compared to model predictions.

### 4.1 Analysis and Experimental Methods

#### 4.1.1 Material Selection and Fabrication

The PV film modules (PT15-300), manufactured by Iowa Thin Film Technologies Inc. (Ames, IA), were comprised of a 1- $\mu\text{m}$  conductive ZnO layer (TCO), 1- $\mu\text{m}$  aSi, a Kapton insulation and an Al substrate. They were bare PV films without the

encapsulation that is added to protect against the elements. The composite substrate was a unidirectional  $[0^\circ]_8$  CFRP laminate assembled from prepreg (DA 409U/G35 150 unidirectional carbon fibers) [106] and cured on a hot plate.

PDMS was selected as the interface material because of its tunable mechanical properties and the ability to cast in different thicknesses, which met the requirements set by the analytical model in this study. By varying the ratio of the silicone elastomer-to-curing agent from 33:1 to 5:1, the initial elastic modulus can be controlled in the broad range of 0.1-2 MPa [107,108]. Furthermore, control of the PDMS film thickness provides a broad range of values for the effective compliance of the PDMS interface layer. Notably, PDMS (i) can be directly cast or spin-coated onto the back side of the PV film without affecting its functionality, (ii) provides large area coverage and a flat surface for direct attachment of other materials, (iii) is electrically insulating, and (iv) can withstand a broad range of service temperatures. The schematic in Figure 4.1 shows the three-layer material system, with  $E$ ,  $G$ ,  $\nu$  and  $t$  being the elastic modulus, shear modulus, Poisson's ratio and layer thickness, respectively. The subscripts 1, 2 and 3 correspond to the CFRP laminate, the PDMS interface material and the PV layer, respectively.

PDMS was synthesized by mixing different ratios of silicone elastomer-to-curing agent (SYLGARD 184, Dow Corning, Midland, MI) followed by degassing for 25 min. The PV film was attached to a Si wafer with the TCO side facing the Si wafer to spin coat PDMS on the back side of the Al substrate. The spinning rate is determined by the viscosity of PDMS, which, in turn, depends on the ratio of the silicone elastomer-to-curing agent [109,110]. After spin-coating, the PDMS layer was cured together with the unidirectional  $[0^\circ]_8$  CFRP laminate on a hot plate at 80°C and for 4 hr. The CFRP prepreg was already pre-cured under light pressure on a hot plate at 180°C for 4 hr. For improved adhesion, all CFRP specimens were polished with a grinder-polisher (ECOMET 3, BUEHLER, Inc.) before attached to the uncured PDMS layer to ensure good adhesion. Thus, the PDMS layer also served as the adhesive between the CFRP laminate and the PV film. In the absence of the PDMS interface, the PV film was co-cured directly with the prepreg resulting in good adhesion until failure at strains as high as 1.7%.

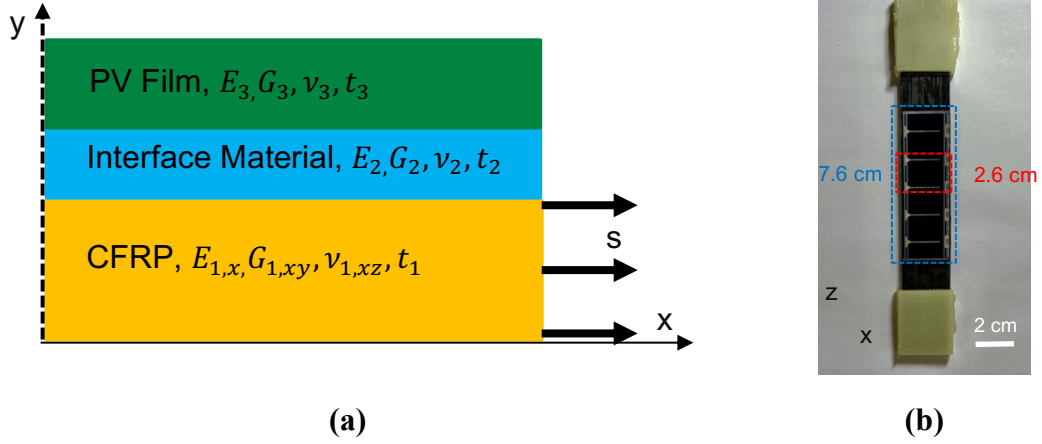


**Figure 4.1 (a)** Schematic of (symmetric half) three-layer structure. **(b)** Integrated PV film-PDMS-CFRP laminate test specimen. The yellow tabs provide gripping for mechanical testing. The 7.6 cm long PV module shown in (b) is a full length PV module, while the 2.6 cm segment of the full length PV module shown in the same figure is a unit PV cell.

#### 4.1.2 Analytical Problem Formulation

In order to evaluate the interface material parameters resulting in a reduction of the uniaxial tensile strain applied to the CFRP laminate across the interface material, the strain attenuation,  $\Delta\varepsilon_{(1-3),xx}$ , between the CFRP laminate and the PV film is defined as a metric:

$$\Delta\varepsilon_{(1-3),xx} = \frac{\varepsilon_{1,xx}|_{y=t_1} - \varepsilon_{3,xx}|_{y=t_1+t_2}}{\varepsilon_{1,xx}|_{y=t_1}} \times 100 (\%) \quad (4.1),$$

where the layer thicknesses  $t_1$  and  $t_2$  are defined in Figure 4.1(a), and  $\varepsilon_{i,xx}$  is the uniaxial strain in layer  $i$ .

The stresses and strains in the three-layer stack in Figure 4.1 were calculated analytically following the 2D problem formulation by Li et al. [78]. Plane strain conditions were assumed since the lateral dimensions of the test specimens were much larger than the thickness of the PV film, the CFRP laminate and the PDMS. Furthermore,

structural bending was neglected because of the much larger thickness and stiffness of the CFRP laminate compared to the other layers. Perfect bonding between all layers was assumed. The PV and PDMS were considered as isotropic, and the CFRP substrate was treated as orthotropic, as described in Appendix B1. Finally, all materials were considered as linearly elastic in the relatively small range of strains applied in this problem (<2%). Based on these assumptions and symmetry conditions, the boundary conditions in this problem are:

$$\begin{aligned}
\tau_{1,yx}\Big|_{x=0} &= 0 \text{ (symmetry plane)} \\
\tau_{1,yx}\Big|_{y=0} &= 0 \text{ (free surface)} \\
\sigma_{3,yy}\Big|_{y=t_1+t_2+t_3} &= 0 \\
\int_0^{t_1} \sigma_{1,xx}\Big|_{x=\frac{L}{2}} dy &= St_1 \\
\int_{t_1}^{t_1+t_2} \sigma_{2,xx}\Big|_{x=\frac{L}{2}} dy + \int_{t_1+t_2}^{t_1+t_2+t_3} \sigma_{3,xx}\Big|_{x=\frac{L}{2}} dy &= 0
\end{aligned} \tag{4.2},$$

where  $\sigma$  and  $\tau$  are the tensile and shear stress in each layer,  $S$  is the stress applied to the CFRP laminate, and  $L$  is the length of the PV film.

An analytical solution for the stress fields in the CFRP laminate, the PDMS interface layer, and the PV film is then obtained and given in Equations (4.3), (4.4) and (4.5), respectively, by solving the differential equations for force equilibrium, and using the boundary conditions in Equation (4.2) along with the interface stress and strain compatibility conditions, as described by [78]:

$$\begin{aligned}
\tau_{1,yx} &= P_1 \sinh n_1 x \sin b_1 y \\
\sigma_{1,xx} &= \frac{P_1 b_1}{n_1} \cosh n_1 x \cos b_1 y + E
\end{aligned} \tag{4.3},$$

$$\sigma_{1,yy} = -\frac{P_1 n_1}{b_1} \cosh n_1 x \cos b_1 y + h_1(x)$$

$$\tau_{2,yx} = \sinh n_2 x (M \sin b_2 y + N \cos b_2 y)$$

$$\sigma_{2,xx} = \frac{b_2}{n_2} \cosh n_2 x (M \cos b_2 y - N \sin b_2 y) + F \quad (4.4),$$

$$\sigma_{2,yy} = -\frac{n_2}{b_2} \cosh n_2 x (M \cos b_2 y - N \sin b_2 y) + h_2(x)$$

$$\tau_{3,yx} = P_3 \sinh n_3 x \sin b_3 (t_1 + t_2 + t_3 - y)$$

$$\sigma_{3,xx} = -\frac{P_3 b_3}{n_3} \cosh n_3 x \cos b_3 (t_1 + t_2 + t_3 - y) + G \quad (4.5).$$

$$\sigma_{3,yy} = \frac{P_3 n_3}{b_3} \cosh n_3 x \cos b_3 (t_1 + t_2 + t_3 - y) + h_3(x)$$

The longitudinal strain in each layer is then calculated from generalized Hooke's law:

$$\varepsilon_{1,xx} = \left( \frac{P_1 b_1}{n_1} \cosh n_1 x \cos b_1 y + E - \nu_{1,xy}^* \left( -\frac{P_1 n_1}{b_1} \cosh n_1 x \cos b_1 y + h_1(x) \right) \right) \frac{1}{E_{1,x}^*}$$

$$\varepsilon_{2,xx} = \left( \frac{b_2}{n_2} \cosh n_2 x (M \cos b_2 y - N \sin b_2 y) - \nu_2^* \left( -\frac{n_2}{b_2} \cosh n_2 x (M \cos b_2 y - N \sin b_2 y) + h_2(x) \right) \right) \frac{1}{E_2^*} \quad (4.6).$$

$$\begin{aligned} \varepsilon_{3,xx} = & \left( -\frac{P_3 b_3}{n_3} \cosh n_3 x \cos b_3 (t_1 + t_2 + t_3 - y) + G \right. \\ & \left. - v_3^* \left( \frac{P_3 n_3}{b_3} \cosh n_3 x \cos b_3 (t_1 + t_2 + t_3 - y) \right. \right. \\ & \left. \left. + h_3(x) \right) \right) \frac{1}{E_3^*} \end{aligned}$$

The functional forms of the parameters  $E$ ,  $F$ ,  $G$ ,  $M$ ,  $N$ ,  $h_1$ ,  $h_2$ ,  $h_3$ ,  $n_1$ ,  $n_2$ ,  $n_3$ ,  $P_1$ , and  $P_3$  in Equations (4.3)-(4.6) are provided in Appendix B2.

## 4.2 Determination of Layer Properties

The thickness and mechanical properties of the CFRP laminate, the PDMS interface layer and the PV film were determined and served as inputs to the analytical model. The uniaxial modulus of each layer was determined via uniaxial tensile testing as described in Section 2.2.1. PDMS films with different mixing ratios (Silicone elastomer/Curing agent) from 33:1 to 5:1 were cast and cut into the form of long strips with dimensions 19×5×2 mm (L×W×T) to obtain the small-strain tensile modulus of PDMS,  $E_2$ . Individual strips of PV films with dimensions 50×2 mm (L×W) were also tested to obtain the effective modulus of the PV film,  $E_3$ . Example stress-strain curves of the PV film and the CFRP laminate are shown in Figures 4.2(a) and 4.2(b). The initial slope of each curve represents the elastic modulus,  $E_3 = 10.4 \pm 0.1$  GPa and  $E_{l,x} = 82.8 \pm 1.5$  GPa, respectively.  $\nu_{l,xz}$  was calculated as 0.22 from the ratio of the normal strains in z and x direction, which were computed via DIC.

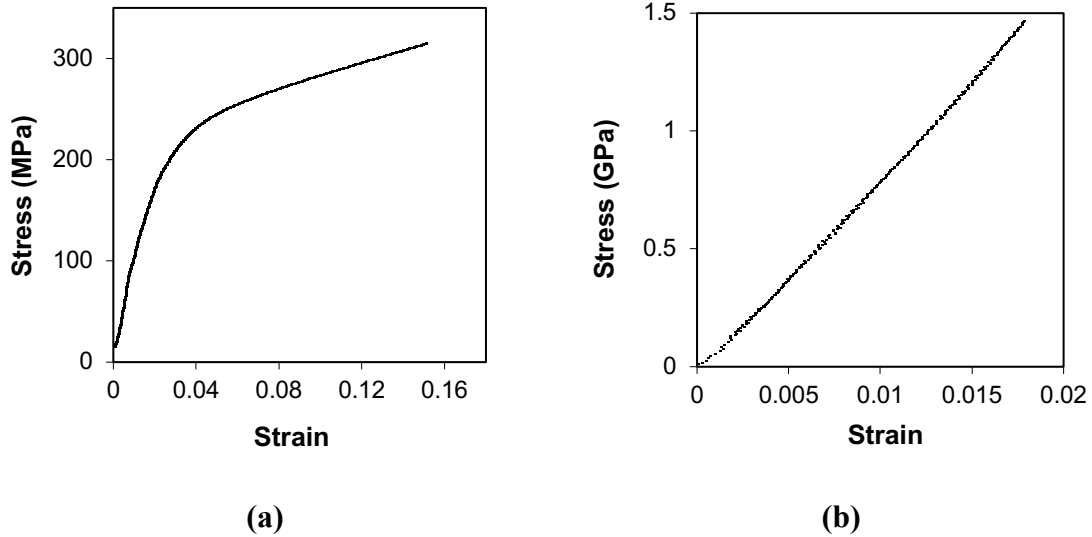


**Figure 4.2** Stress-strain curves of a **(a)** PV thin film and **(b)** a unidirectional  $[0^\circ]_8$  CFRP laminate.

PDMS coatings with various elastic moduli and thicknesses, serving as the compliant interface layer were designed as guided by the analysis in Section 4.1.2 and applied via spin coating onto the back side of the PV film. The PDMS layer thickness that was measured after curing with the aid of a Scanning Electron Microscope (SEM) was controlled by the spin coater rotational speed as shown in the plot in Figure 4.3(a). Furthermore, stress-strain curves of PDMS specimens for the three different mixing ratios of silicone elastomer-to-curing agent were obtained and given in Figure 4.3(b). In the present application, the PDMS layer is subjected to a small range of strains ( $<2\%$ ) which are controlled by the CFRP laminate strain, therefore, the initial elastic modulus of PDMS is relevant to our calculations. Thus, the relevant PDMS modulus values were determined by linear fitting the experimental stress-strain curves of pure PDMS films in the strain range 0.3-0.9%, which is the range of the mean tensile strain that the PDMS interface layers experienced between their top (PV side) and bottom surfaces (CFRP laminate side) in the present experiments. For mixing ratios of 5:1, 10:1 and 33:1 the elastic moduli of PDMS were measured as  $0.87 \pm 0.008$ ,  $0.46 \pm 0.006$ , and  $0.1 \pm 0.002$  MPa respectively. These elastic moduli were used in all calculations in this dissertation research.

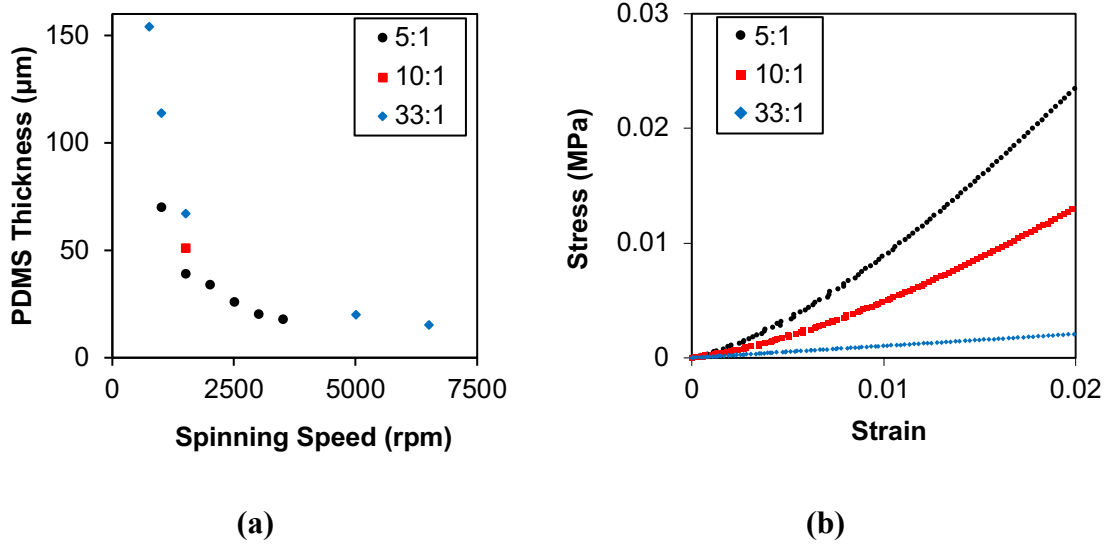


**Figure 4.3** (a) Spinning speed vs. cured PDMS layer thickness and (b) stress-strain curves of freestanding PDMS films with different mixing ratios of silicone elastomer-to-curing agent.

**Table 4.1** Measured properties of the PV module film and the CFRP laminate.

	Thickness ( $\mu\text{m}$ )	Elastic modulus (GPa)	Poisson's ratio
<b>PV film (with supporting layers)</b>	$52 \pm 0.05$	$10.4 \pm 0.1$	$0.3 \pm 0.001$
<b>Composite laminate</b>	$1900 \pm 4$	$E_{1,x} = 82.8 \pm 1.5$	$\nu_{1,xz} = 0.22 \pm 0.003$

### 4.3 Determination of Parameter Space for Interface Layer Properties

The solution for the longitudinal strain in Equation (4.6) provides a tool to design an interface material that reduces the strain transfer from the CFRP laminate to the PV film. However, the complexity of equations for  $\varepsilon_{i,xx}$  does not readily lead to an obvious design strategy. From the structure of the longitudinal strain solution in Equation (4.6) and the mechanics of the problem the mechanical properties and geometrical parameters (layer thickness) that influence the value of  $\Delta\varepsilon_{(1-3),xx}$  in Equation (4.1) were identified.

In the case of uniaxial loading that was considered in this study, parametric calculations were carried out to evaluate the relative contribution of the mechanical properties and the layer thicknesses given in Figure 4.1(a) to  $\Delta\varepsilon_{(1-3),xx}$ . With the material properties and thickness for the CFRP and the PV module serving as a starting point, Table 4.1, first  $G_2$  and  $t_2$  were varied systematically to calculate the longitudinal strain in the three layers via Equation (4.6). The results showed that  $\Delta\varepsilon_{(1-3),xx}$  scales in an inverse manner with the effective shear stiffness of the PDMS interface layer,  $G_2/t_2$ . Assuming isotropic mechanical behavior for PDMS one can further write:  $\frac{G_2}{t_2} = \frac{E_2}{2t_2(1+\nu_2)}$ . Therefore, to simplify the presentation of our results,  $E_2/t_2$  was used as the control parameter, after substituting  $\nu_2 = 0.499$  for all PDMS compositions. The results presented in the next Sections are the same if  $G_2/t_2$  was used as the control parameter. Similarly, by varying the properties of the PV module layer in Equation (4.6) it was shown (Appendix B3) that  $E_3$  and  $t_3$  both increase  $\Delta\varepsilon_{(1-3),xx}$  and their combined effect can be captured by the effective longitudinal stiffness of the PV layer,  $E_3t_3$ .

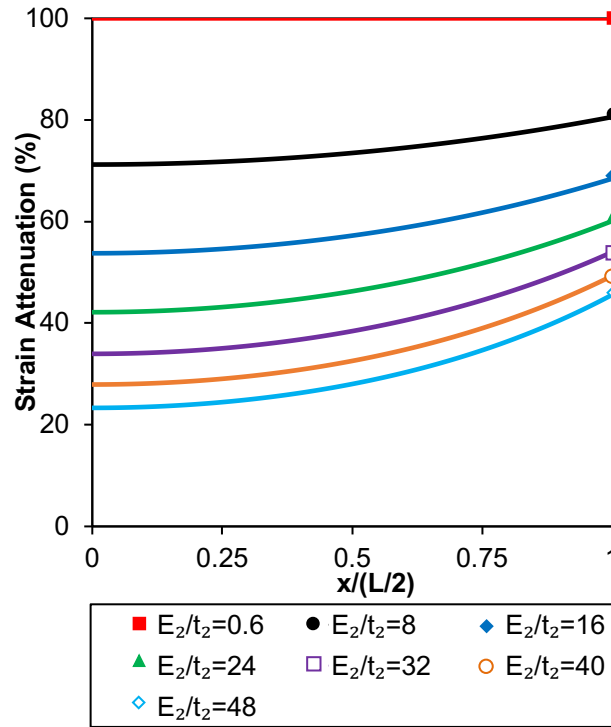
The aforementioned design parameters for the PDMS interface agree with the results reported by Dai et al. [64] who used a shear lag model to calculate the strain transferred across an adhesive. Their shear lag model did not include the properties of the substrate, which for all practical purposes can be considered as perfectly rigid. The elastic solution adopted in this study allows taking into account the thickness and uniaxial modulus of the CFRP substrate too. The longitudinal strain solution in Equation (4.6) can provide insights into the role of  $E_{1,x}$  and  $t_1$ . A parametric study, carried out by varying  $E_{1,x}$  and  $t_1$  in the calculation of  $\Delta\varepsilon_{(1-3),xx}$ , showed that  $E_{1,x}$  and  $t_1$  begin to matter when  $E_{1,x}t_1 \approx E_3t_3$ . If the CFRP laminate acts as load-bearing and  $E_{1,x}t_1$  is several orders of magnitude larger than  $E_3t_3$ , then  $E_1$  and  $t_1$  have no effect on  $\Delta\varepsilon_{(1-3),xx}$ . It can be also shown (Appendix B3) that for  $\frac{E_3t_3}{E_{1,x}t_1} \geq 0.51$ , a reduction in  $E_{1,x}t_1$  begins to decrease  $\Delta\varepsilon_{(1-3),xx}$ , because of the increased relative stiffness of the PV module compared to the CFRP laminate. Given the large thickness and uniaxial modulus of the CFRP laminate used in the present study, Table 4.1, it is  $\frac{E_3t_3}{E_{1,x}t_1} = 0.0034 \ll 0.51$ , therefore, order of magnitude changes to the term  $E_{1,x}t_1$  would have no practical effect on strain attenuation in the

present study. Thus, for all practical purposes only the term  $E_3t_3$  was treated as a control parameter, albeit not varied herein because a commercial PV module with fixed thickness and mechanical properties was utilized.

For the material system at hand,  $E_3t_3 = 540.8 \text{ MPa}\cdot\text{mm}$  as calculated from the data in Table 4.1 for the given PV module. Different values for  $E_2/t_2$  were then entered into Equation (4.6) to calculate  $\Delta\varepsilon_{(1-3),xx}$  in the range 0% and 100%. The resulting range of  $E_2/t_2$  values served as a guide to prepare a series of test specimens with  $E_2/t_2$  values approximately ranging from 0.6 to 48 MPa/mm. As shown in Figure 4.4(a), for this range of  $E_2/t_2$  values,  $\Delta\varepsilon_{(1-3),xx}$  between 23% and 100% could be theoretically achieved for the 2.6-cm long unit PV cell shown in Figure 4.1(b).

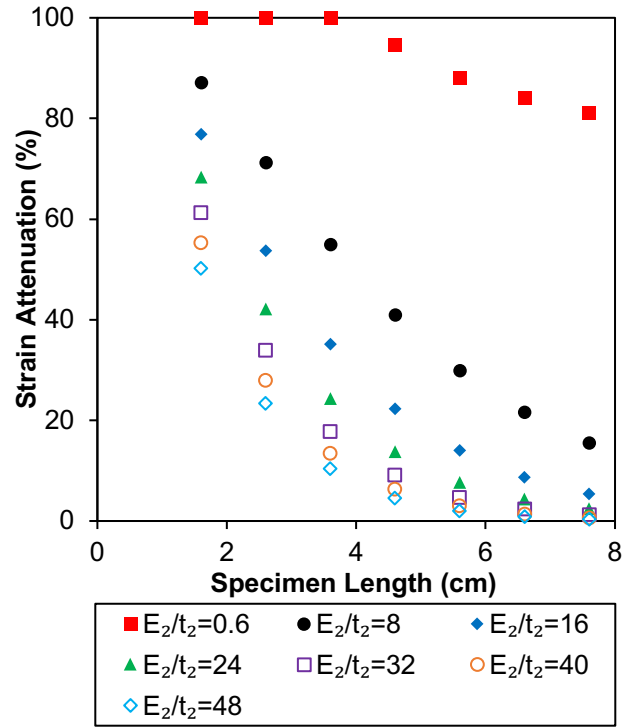
For the same  $E_2$  and  $t_2$ ,  $\Delta\varepsilon_{(1-3),xx}$  scales inversely with the PV film length,  $L$ . As shown in Figure 4.4(b), smaller values of  $E_2/t_2$  are required to achieve the same strain attenuation in longer PV films. For instance, for a 3.6-cm long PV film,  $E_2/t_2 = 0.6 \text{ MPa/mm}$  results in 100% strain attenuation, whereas for a 7.6-cm long PV module, the strain attenuation is reduced to 81% for the same value of  $E_2/t_2$ . In order to gain further perspectives, strain attenuation maps were constructed for a short, 2.6-cm unit PV cell and a long, 7.6-cm (full length) PV module, Figures 4.5(a,b), for different values of  $E_3t_3$  and  $E_2/t_2$ . These strain attenuation maps can be used for PV modules with different properties from those in the present study. The strain attenuation maps depend on the PV film length because Equation (4.6) contains its length through the boundary conditions given in Equation (4.2). The strain attenuation reported in the maps in Figures 4.5(a,b) is calculated at the mid-point along each PV film, e.g. Figure 4.4(a). As pointed out with dashed lines in Figures 4.5(a,b), for the same value of  $E_3t_3 = 540.8 \text{ MPa}\cdot\text{mm}$ , as determined by the properties of the given PV module in Table 4.1, the full PV module (7.6 cm) would require a more compliant or a thicker interface layer, as defined by the ratio  $E_2/t_2$ , to achieve 80% strain attenuation (star point) at the mid-span of its length, compared to the shorter (2.6 cm) unit PV cell. Specifically,  $E_2/t_2 = 0.59 \text{ MPa/mm}$  for the 7.6-cm full PV module, compared to  $E_2/t_2 = 4.9 \text{ MPa/mm}$  for the 2.6-cm unit PV cell. This translates into 8.3 times more compliant or thicker interface layer for the full PV

module compared to the unit PV cell. Similar correlations can be derived from Figure 4.4(b) for other PV film lengths.



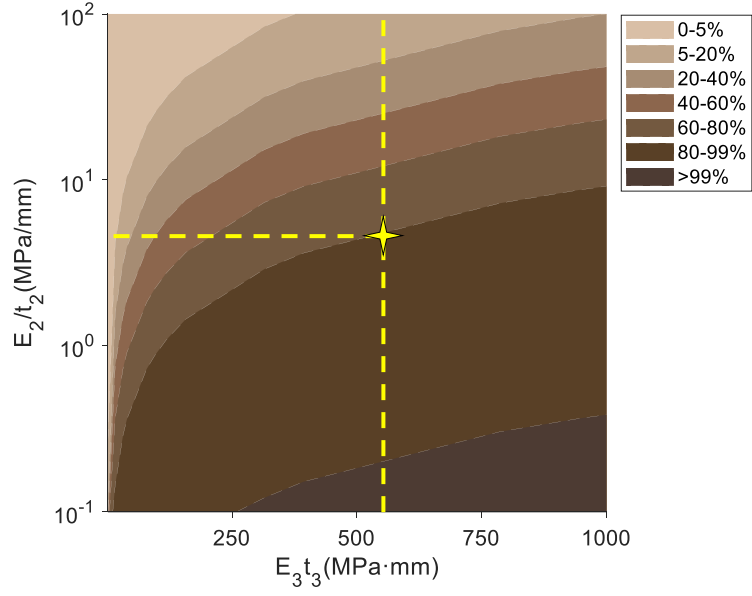
(a)

(Figure 4.4 continued)

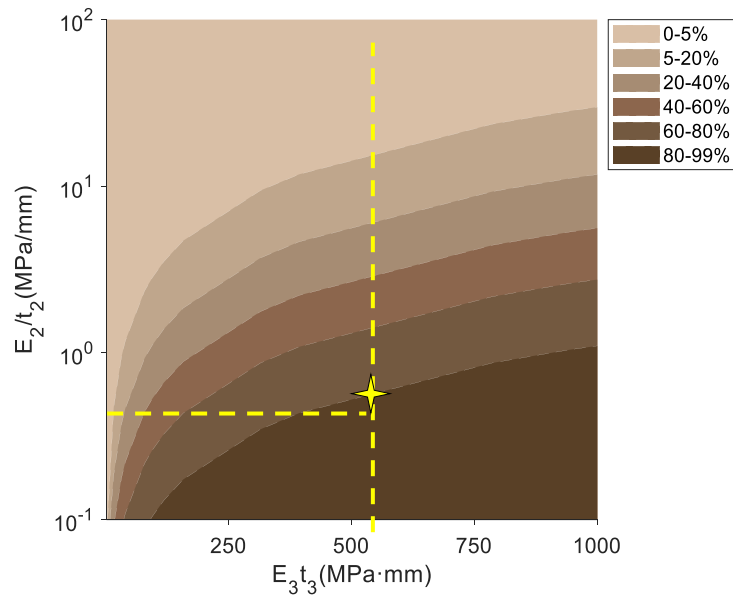


(b)

**Figure 4.4 (a)** Strain attenuation for  $E_3t_3 = 540.8$  MPa·mm for a 2.6-cm long unit PV cell, Figure 4.1(b). **(b)** Strain attenuation as a function of PV module length. The units of  $E_2/t_2$  are MPa/mm.



(a)



(b)

**Figure 4.5.** Strain attenuation map for a (a) 2.6-cm long unit PV cell, and a (b) 7.6-cm long full length PV module. The strain attenuation in the mid-span of the length of each PV film is plotted. Darker shades designate larger strain attenuation. The star symbol marks the same percentage of strain attenuation (80%) for the two PV film lengths.

#### 4.4 Experimental Evaluation of Strain Attenuation

In the absence of a PDMS interface, strain measurements via DIC showed *zero* strain attenuation between the PV film and the CFRP laminate. Because  $E_{1,x}t_1$  is several orders larger than  $E_3t_3$ , the strain in the CFRP laminate is fully imposed onto the PV film. Complete strain transfer takes place under the condition of perfect bonding, which was verified by the fact that the strain on the CFRP laminate side was identical to that on the PV film side until CFRP laminate failure.

Insertion of the PDMS interface layer provided strain attenuation that depended on the interface layer properties. Tables 4.2 and 4.3 list the details of the PDMS interface layers in the specimens prepared for the purposes of this study, with  $E_2/t_2$  values ranging between 0.6 and 48 MPa/mm. The specimens in Table 4.2 were comprised of 2.6-cm long PV films, which is the length of a unit PV cell, and were used only for strain attenuation measurements. In the specimens listed in Table 4.3, the PV modules were 7.6 cm long which is the length of a full PV film module and the shortest PV film that could be easily wired to obtain the FF. These specimens were used for concurrent strain attenuation and FF measurements. Specimen #10 served as the control to verify that the strain measured on the CFRP laminate and the PV film was the same until failure of the laminate. Indeed, using full field strain measurements via DIC the strain was confirmed to be the same on the CFRP laminate and the PV film (i.e. 0% strain attenuation). Furthermore, fragmentation initiated in the PV film at  $\sim 0.8\%$  strain, which agrees with Antartis and Chasiotis [59] for the onset of fragmentation in the aSi layer. Fragmentation was virtually complete at 1% strain, as shown in Figure 4.6.

In the presence of a PDMS interface layer, the measured  $\Delta\varepsilon_{(1-3),xx}$  ranged from 36% to 100% as summarized in Tables 4.2 and 4.3. The smallest value of  $\Delta\varepsilon_{(1-3),xx}$  was recorded for the minimum value of  $t_2=18\ \mu\text{m}$  (smaller values resulted in poor adhesion between the PV and the CFRP laminate) and the maximum value of  $E_2$  that was attained for 5:1 mixing ratio of silicone elastomer-to-curing agent. This is consistent with the effect of the ratio  $E_2/t_2$  described in Section 4.1.2. Examples of the strain measured on the CFRP laminate vs. the PV module side are plotted in Figure 4.7 for different strain

attenuation values. For instance, in the case of Specimen #13 the strain in the PV module remained zero in the entire test until CFRP laminate failure at 1.76% strain. Similarly, a 114- $\mu\text{m}$  thick PDMS layer in Specimen #12 resulted in 81% strain attenuation: the strain in the CFRP laminate reached 1.6% while the strain in the PV film was only 0.31%, without any signs of aSi fragmentation. Specimens that were loaded and unloaded before failure were inspected and no detachment between the PV module and the CFRP laminate was detected.

**Table 4.2** Measured strain attenuation for a unit PV cell with 2.6 cm length and different PDMS layers.

<b>Specimen #</b>	<b>1</b>	<b>2</b>	<b>3</b>	<b>4</b>	<b>5</b>	<b>6</b>	<b>7</b>	<b>8</b>	<b>9</b>
<b>Silicone-to-curing agent ratio</b>	33:1	33:1	33:1	10:1	5:1	5:1	5:1	5:1	5:1
<b>PDMS elastic modulus (MPa)</b>	0.1	0.1	0.1	0.46	0.87	0.87	0.87	0.87	0.87
<b>PDMS thickness (<math>\mu\text{m}</math>)</b>	114	67	15	51	69	39	34	26	18
<b><math>E_2/t_2</math> (MPa/mm)</b>	0.9	1.5	6.5	9	13	22	26	33	48
<b>Peak tensile strain (%)</b>	1.1	1.2	1.3	0.9	1.3	0.9	0.7	0.9	1.1
<b>Measured strain attenuation (%)</b>	100	100	100	81	67	58	52	45	36

**Table 4.3** Measured strain attenuation for a full PV module with 7.6 cm length and different PDMS layers.

Specimen #	10 (Control)	11	12	13
Silicone-to-curing agent ratio	None	33:1	33:1	33:1
PDMS elastic modulus (MPa)		0.1	0.1	0.1
PDMS thickness ( $\mu\text{m}$ )		67	114	154
$E_2/t_2$ (MPa/mm)		1.5	0.9	0.6
Ultimate tensile strain of CFRP laminate (%)	1.6	1.1	1.6	1.8
Measured strain attenuation (%)	0	67	81	100

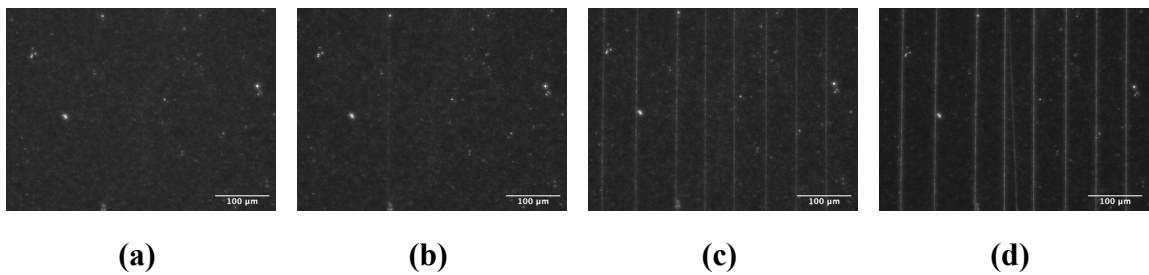


**Figure 4.6** Fragmentation of Specimen #10 subjected to tensile strain: (a) 0%, (b) 0.79%, (c) 1%, and (d) 1.58%. The specimen was loaded in the horizontal direction. Visualization of the fragmentation cracks requires high magnification optical microscopy and oblique angle illumination to highlight the hairline cracks.

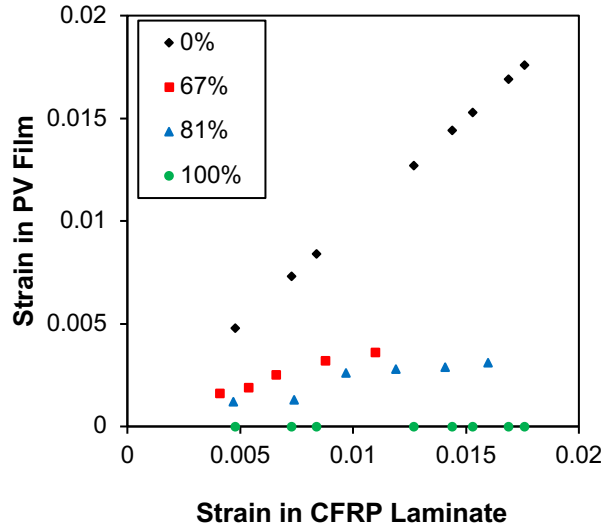


**Figure 4.7** Experimental tensile strain in the PV layer vs. the CFRP laminate for strain attenuation 0% (#10), 67% (#11), 81% (#12), and 100% (#13). The numbers in parentheses correspond to the specimens listed in Table 4.3.

As predicted by the theoretical model, the PV film elastic modulus, thickness and length controlled the strain attenuation. For instance, Specimens #5-9 had the same elastic modulus but gradually decreasing thickness, which resulted in gradually decreasing strain attenuation from 67% to 36%. On the other hand, Specimen #3 with comparable thickness to Specimen #9 but 8.7 times lower elastic modulus provided 100% strain attenuation. A similar conclusion is drawn by comparing the strain attenuation provided by Specimens #5 and #2 which had comparable PDMS layer thickness and the resulting strain attenuation scaled inversely with the elastic modulus of PDMS. The nine specimens in Table 4.2 demonstrate the coupled role of thickness and elastic modulus on the effective shear stiffness of the PDMS layer, while also demonstrating the robust control of strain transfer by the PDMS interface.

#### 4.5 Experimental Results vs. Analytical Model Predictions

The effective shear stiffness,  $E_2/t_2$ , of the PDMS interface vs. strain attenuation is plotted in Figure 4.8(a) and compared with the model predictions by Equations (4.1) and

(4.6). The model predictions closely followed the trend of the experimental strain attenuation data, but also consistently underestimated the strain attenuation by 10-35%. For instance, for  $E_2/t_2 = 12.6$  MPa/mm, the experimental strain attenuation was 67% compared to a predicted value of 60%. The systematic difference between the model and the experimental predictions may originate in several experimental and modeling sources. Among them are the model assumptions, specifically not accounting for the effect of bending, which depends on the ratio  $E_3t_3/E_{1,x}t_1$ . This effect is expected to be rather small because the combined contribution of the interface and the PV layers to the shift of the neutral axis of the integrated structure, Figure 4.1(a), is small due to the much larger modulus and thickness of the CFRP laminate.

The difference between the experimental measurements and the model predictions shown in Figure 4.8(a) is more likely to originate in the uncertainty in the elastic modulus values of the PDMS layer as integrated between the CFRP laminate and the PV film. The elastic modulus of PDMS was measured from freestanding test specimens, whereas the PDMS interface layer was cured in situ between the CFRP laminate and the PV module. Confinement and thermal gradients during curing can affect the degree of cross-linking of PDMS and, therefore, its elastic modulus. To test this assumption, the value  $(\frac{E_2}{t_2})_{model}$  was calculated by substituting Equation (4.6) and the experimentally measured strain attenuation for the PDMS interface layers fabricated with a silicone elastomer-to-curing agent mixing ratio of 5:1 (Table 4.2), into Equation (4.1). Then, a least squares minimization procedure was applied by using all the experimental data for strain attenuation less than 100%:

$$\sum_{i=1}^n [c(\frac{E_2}{t_2})_{measured} - (\frac{E_2}{t_2})_{model}]_i^2 \quad (4.7)$$

where  $c$  is a correction factor applied uniformly to all values  $(\frac{E_2}{t_2})_{measured}$  which were calculated by using direct measurements of  $E_2$  and  $t_2$  (Table 4.2), and  $n$  is the number of data points. Assuming accurate measurements of  $t_2$  via an SEM, the best fit  $E_2$  value for PDMS interface layers with mixing ratio 5:1 was found from Equation (4.7) to be 0.55

MPa, which is smaller by a factor  $c = 0.64$  than the value of 0.87 MPa that was obtained by mechanical testing of freestanding PDMS specimens of the same composition. Substituting the calculated modulus value for PDMS into the analytical model, a very good agreement emerged between the experimental measurements and the model predictions, as shown in Figure 4.8(b).

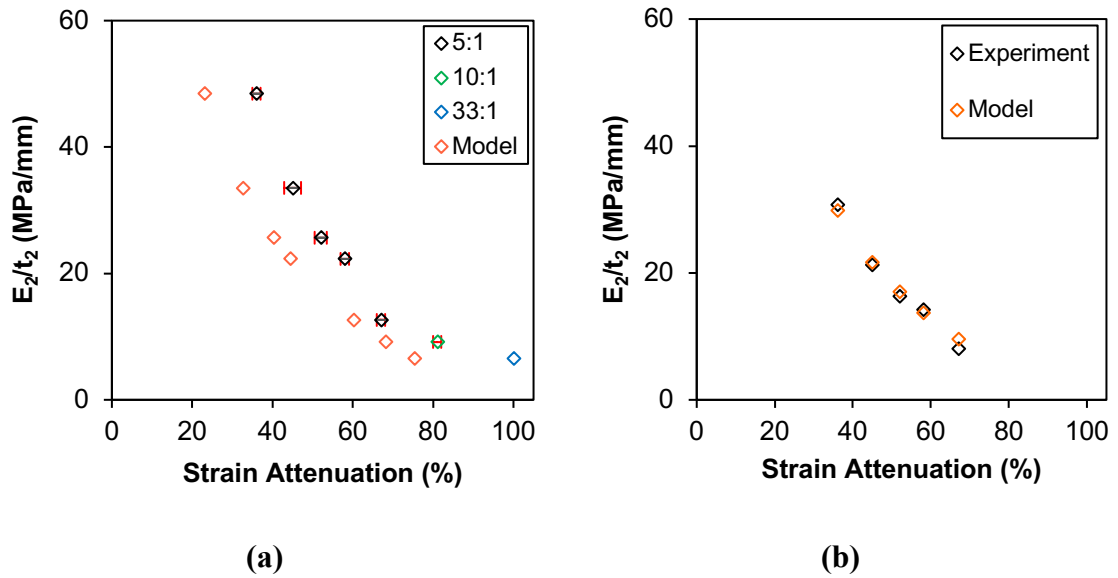


**Figure 4.8 (a)** Experimental results vs. model predictions for  $E_2/t_2$  vs. strain attenuation. The experimental data correspond to Specimens #1-9 in Table 4.2. **(b)** Experimental measurements vs. model predictions for  $E_2/t_2$  vs. strain attenuation after substitution of a best fit value for the  $E_2$ . The experimental data correspond to Specimens #5-9 in Table 4.2.

#### 4.6 I-V Characteristic Curves vs. CFRP Laminate Strain

The method described in Section 2.3 to evaluate the PV film's performance was applied in the Section. The I-V characteristic curves of the test specimens listed in Table 4.3 were measured during mechanical testing. Example I-V characteristic curves are plotted in Figures 4.9(a-d), which, in turn were used to calculate the FF via Equation

(2.6) that is plotted in Figure 4.10. In the absence of a PDMS interface, the value of FF declined after the PV module (and the CFRP laminate) reached 0.80% strain, from an initial value of FF = 0.73 to as low as FF = 0.59 when the CFRP laminate failed at 1.58% strain. This range of FF values as a function of tensile strain is in agreement with results by Jones et al. [61], also see Gleskova et al. [111], derived from bending tests of triple junction aSi-Ge solar cell films. As shown in Figure 4.6(b), the aSi layer began to fragment at ~0.80% strain, which is consistent with a prior study by this group [59]. In the presence of a PDMS interphase the FF maintained the strain-free value of 0.74, even when the CFRP laminate reached 1.76% strain, Figure 4.10.

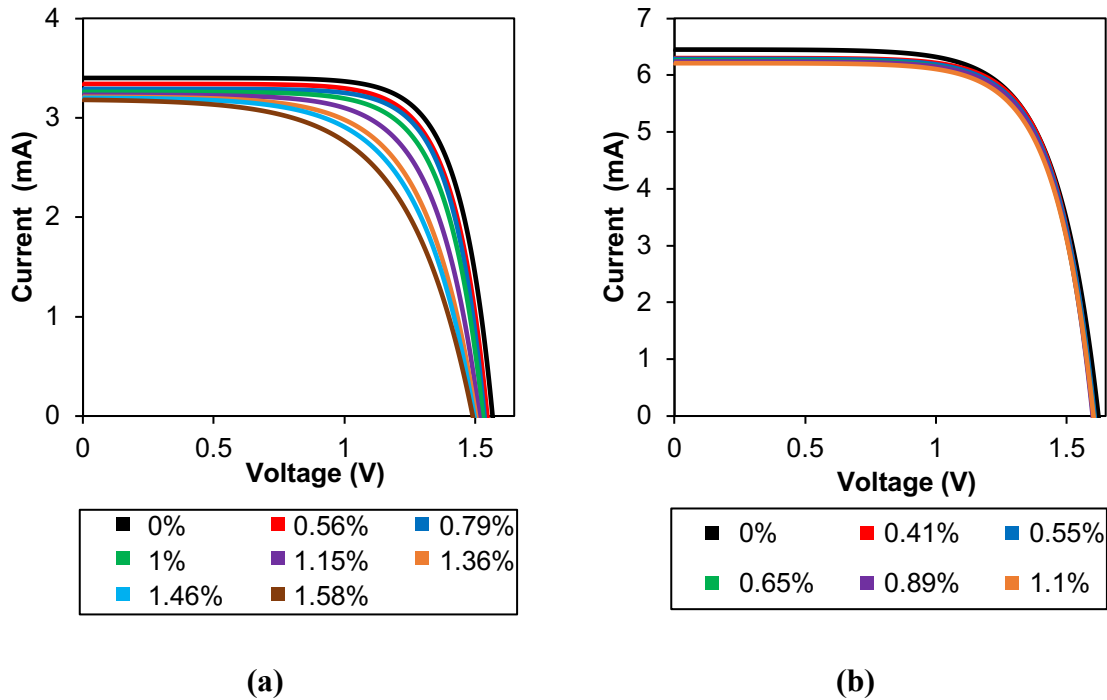


(Figure 4.9 continued)

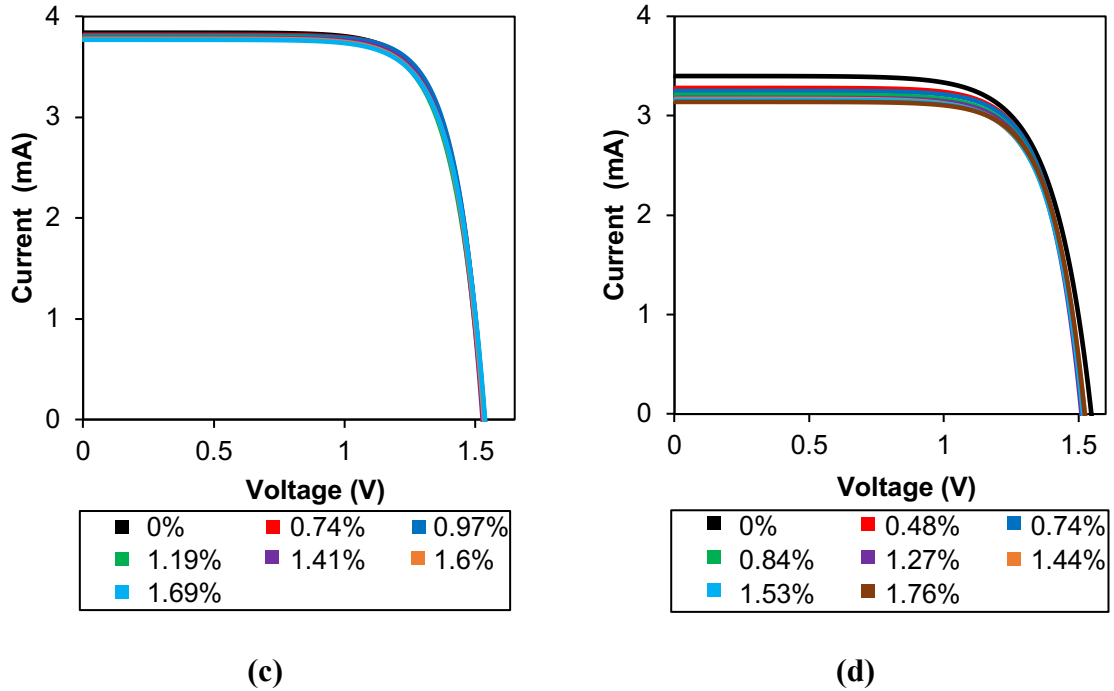


**Figure 4.9** I-V characteristic curves obtained from test specimens **(a)** #10 (0%), **(b)** #11 (67%), **(c)** #12 (81%), and **(d)** #13 (100%) listed in Table 4.3, with the experimental strain attenuation values given in parentheses. The legends show the (%) strain applied to the CFRP laminate.

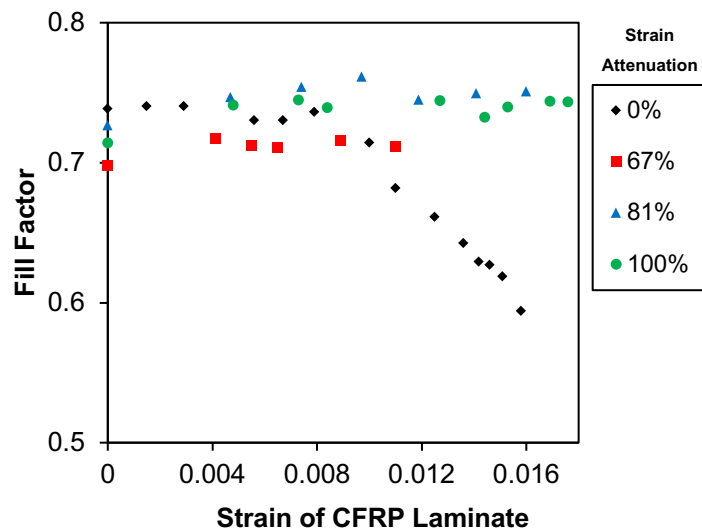


**Figure 4.10** Fill factor of PV films with strain attenuation 0%, 67%, 81%, and 100% as measured from Specimens #10, #11, #12, and #13, respectively. The specimen details are given in Table 4.3.

## 4.7 Evaluation of Strain Attenuation Methodology

The validated design framework for interfacial strain attenuation presented in this dissertation research demonstrated that the effective shear stiffness of a PDMS interface can be tuned effectively (reaching 100% strain attenuation) and efficiently (using the minimum PDMS interface layer thickness required to attain 100% strain attenuation) by changing either the thickness or the elastic modulus of PDMS to meet a target value of  $E_2/t_2$  according to the  $E_3t_3$  value for the PV module and the strain attenuation maps given in Figure 4.5. Within the practical limits for the small strain elastic modulus of PDMS (0.1-10 MPa, as controlled by the ratio of silicone elastomer-to-curing agent), and its thickness (~20-500  $\mu\text{m}$ ), the value of  $E_2/t_2$  of the PDMS interface can be varied by more than three orders of magnitude (0.2 - 500 MPa/mm) to achieve high strain attenuation for a broad range of  $E_3t_3$  values. The minimum thickness of the PDMS layer depends on the surface roughness of the CFRP laminate and the back side of the PV module. In this work the surface of the pre-cured CFRP laminates was smoothed with a grinder-polisher to reduce the surface roughness and allow for bonding to the PV films by using PDMS layers that were as thin as ~18  $\mu\text{m}$ . Thinner PDMS layers resulted in debonding of the PV film during stretching of the CFRP laminate. On the other hand, thick PDMS layers with cured thicknesses of the order of 500  $\mu\text{m}$  or more require special measures to prevent flow during casting and curing. Such thick interface layers also begin to affect the overall thickness of the integrated structure and introduce potentially significant bending effects.

The strategy for strain attenuation presented in this dissertation research provides guidelines for the thickness and synthesis/mechanical properties of an effective (attaining 100% strain attenuation) and efficient (ensuring minimum necessary layer thickness) PDMS interface layer for PV modules with different lengths and/or  $E_3t_3$ . This compliant interface not only eliminates strain transfer but also extends the maximum strain that can be applied to load-bearing structures with integrated PV films, thus extending the current spectrum of applications of solar energy. From a practical viewpoint, for a given thickness and modulus of an interface layer, staggered short and wide PV modules bonded onto a substrate that is loaded in the longitudinal direction would result in higher strain attenuation than longer PV modules, which also is consistent with the results and

recommendations by Dai et al. [64]. On the other hand, for a given form factor of a PV module, strain attenuation maps similar to those in Figure 4.5 provide guidelines to tune the PDMS interface layer thickness and modulus in order to obtain a desired strain attenuation.

## 4.8 Conclusions

It was shown that a compliant interface layer can be efficiently designed to eliminate strain transfer from a stiff CFRP laminate to a thin PV film and, therefore, extend the service load of load-bearing structures with integrated thin film solar power. On the contrary, in the absence of a compliant interphase, PV modules begin to fragment at 0.80% strain, gradually losing their functionality. Maps of strain attenuation due to a compliant interface were created capturing the coupled effects of the elastic mechanical properties and thickness of the interface layer ( $E_2/t_2$ ) and the bonded PV module ( $E_3t_3$ ), as well as the length of the PV module. Based on these strain attenuation maps, PDMS was shown to be an effective interface material because of its versatility to span a broad range of elastic moduli,  $E_2$ , and thickness,  $t_2$ , values. Experimental combinations of  $E_2$  and  $t_2$  provided  $E_2/t_2$  values for PDMS in the range 0.6-48 MPa/mm, which resulted in up to 100% attenuation of CFRP laminate strain transfer to the PV module. After accounting for manufacturing effects on the effective modulus of the PDMS interface layer, a very good agreement between the experimental measurements and the model predictions emerged. The attenuation or complete elimination of strain transfer from the CFRP laminate to a PV module allowed maintaining the initial value of the fill factor of the PV module until failure of the CFRP laminate at strains as high as  $\sim 1.8\%$ . On the contrary, in the absence of the PDMS interface the fill factor declined beyond the application of 0.8% strain to the CFRP laminate. The work presented in this Chapter provides a validated framework for the design of compliant interfaces between load-bearing structures and integrated functional brittle films.

# CHAPTER 5

## Conclusions

The objective of this dissertation research was to employ compliant interfaces to (a) control surface wrinkling of material systems comprised of a stiff film on a compliant substrate, and (b) mitigate strain transfer from a stiff substrate to a brittle film. This Chapter summarizes the research outcomes and provides an assessment of the extent to which the dissertation objectives were met.

### 5.1 Assessment of Dissertation Outcomes

Prior to this study, no other methods had been reported to control the wrinkle wavelength, amplitude, and direction without modifying the composition or structure of a bilayer material system and without the application of multiaxial loading. In this dissertation, isotropic or orthotropic compliant interface layers made by GLAD were introduced for the first time between a stiff film and a compliant substrate to modify wrinkling. Then, the effect of effective in-plane compressive modulus and anisotropy of the interface layer on the wrinkle pattern were assessed. Towards the above goal, the effect of GLAD process parameters on the morphology of the resulting nanostructures was studied and optimized to fabricate the aforementioned interface layers. The effective in-plane compressive modulus and anisotropy ratio of GLAD nanostructured films were reported for the first time with the aid of analytical models drawn from literature.

Towards the second objective of this research, a highly compliant interface layer comprised of PDMS was successfully integrated between a thin PV film and a CFRP laminate to achieve strain attenuation. Brittle thin PV films can suffer from fragmentation

while subjected to substrate strains as low as 0.3%. Prior to this dissertation, the vast majority of research was focused on improving the functional performance of PV films. An elasticity model by Li et al. [78] was adopted to assess the required interface layer for strain attenuation. It was deduced that for a material system comprised of a stiff CFRP laminate with a fragile top thin film PV, independent control of both the stiffness and the thickness of the interface material is required to handle a wide range of PV film thickness and stiffness values and achieve partial or complete strain attenuation and full preservation of the energy harvesting performance of PV films at large substrate strains.

### **5.1.1 Control of Wrinkle Pattern through Interface Layers**

After a thorough evaluation of the effect of GLAD processing parameters, the deposition angle and rate were selected as  $86^\circ$  and  $10 \text{ \AA}/\text{sec}$ , respectively, to ensure good shadowing effect and good definition of different types of GLAD nanostructures. Two types of GLAD nanostructure films, comprised of nanosprings or nanochevrons, were fabricated by controlling the deposition rate and the rotation speed. Moreover, pitch control modified the interaction between individual GLAD nanostructures in the respective films, thus leading to different effective in-plane compressive moduli for the same total film thickness. As a result, the optimal deposition angle, rotation speed, and deposition rate were identified and used to fabricate isotropic (nanospring) and orthotropic (nanochevron) interface layers to control wrinkling.

The approach to control the wrinkle pattern of a two-layer system, comprised of a stiff film on a compliant substrate, by a compliant interface layer was investigated utilizing the aforementioned GLAD films. The isotropic (nanospring) and orthotropic (nanochevron) Cu interface layers were introduced between a PDMS substrate and a solid Cu film to modify the resulting wrinkle patterns. For instance, by means of these GLAD interface layers, the wrinkle wavelength was reduced by a factor of 3.6 after  $2 \mu\text{m}$  out of  $2.5 \mu\text{m}$  of a solid film were replaced by a Cu nanospring film with  $0.25\text{-}\mu\text{m}$  pitch as the interface layer. Concurrently, the wrinkle amplitude was also reduced by a factor of 3.6 for the same applied strain. Hence, the compliance of the interface layer reduced the

physical length scale of the wrinkle pattern, namely the wrinkle wavelength and amplitude, while maintaining the amplitude-to-wavelength aspect ratio without varying the total thickness as the original solid film. The physical length scale of a wrinkle pattern of a solid film without an interface layer can only be tuned by modifying film's thickness. Furthermore, the effective in-plane compressive modulus of Cu nanospring films was obtained experimentally for the first time, as  $500\pm 21$  MPa and  $830\pm 20$  MPa for a pitch of  $0.25\ \mu\text{m}$  and  $0.5\ \mu\text{m}$ , respectively, by taking advantage of the mechanics of surface wrinkling. The reduced interactions between individual Cu nanosprings with  $0.25\text{-}\mu\text{m}$  pitch contributed to a lower effective in-plane compressive modulus of the respective films.

An analytical model by Yin et al. [13] was extended and utilized to simulate the wrinkling of a three-layer system with an orthotropic interface layer comprised of Cu nanochevrons with  $0.25\ \mu\text{m}$  and  $0.5\ \mu\text{m}$  pitch. By controlling the principal stress direction with respect to the principal material axis, the effective in-plane compressive moduli of Cu nanochevron films with  $0.5\text{-}\mu\text{m}$  pitch along the principal material axis and its normal was calculated as  $710\pm 10$  MPa and  $75.1\pm 2$  MPa, respectively. The anisotropy ratio of Cu nanochevron films,  $E_{i,1}/E_{i,2}$ , was measured to be 8.4 and 9.5 for  $0.25\text{-}\mu\text{m}$  pitch and  $0.5\text{-}\mu\text{m}$  pitch, respectively. This anisotropy ratio directly affects the anisotropy ratio of the effective bending modulus of the composite layer, including the interface layer and the top film,  $E_{c,1}/E_{c,2}$ , and influences the wrinkle direction. The latter deviated from the principal stress direction by  $9.6\pm 0.3^\circ$  when the principal stress direction was at  $45^\circ$  with respect to the principal material axis in Cu nanochevron films with  $0.5\text{-}\mu\text{m}$  pitch as the interface. Therefore, the resulting GLAD nanostructures as the interface layers were demonstrated to be an effective means to control the wrinkling.

### **5.1.2 Strain Attenuation through an Interface Layer**

An approach to achieve the strain attenuation between a brittle film and a stiff substrate was the second objective of this dissertation. PDMS as a compliant interface layer successfully reduced or eliminated the strain transfer from a CRFP laminate

(substrate) to a PV film (brittle film), and protect the latter from structural loads. An analytical model was adopted to identify the range of values for the effective shear stiffness (shear modulus over thickness,  $G_2/t_2$ ) of candidate interface materials by taking the properties of the PV-CFRP laminate material system at hand into account, namely the elastic modulus and thickness of the PV film and the CRFP composite, and the length of the PV film. By controlling both the elastic modulus and the thickness of PDMS, a large range of  $E_2/t_2$  values from 0.6 to 48 MPa/mm was achieved, which resulted in partial or complete strain attenuation in experimental studies. A very good agreement between the experimental measurements and the model predictions was established after accounting for confinement effects on the modulus of PDMS during curing. Furthermore, the fill factor was measured to evaluate the performance of the PV film. The PV film was shown to preserve its initial fill factor while subjected to substrate strains as high as 1.7%, whereas in the absence of an interface layer the fill factor decreased for substrate strains larger than 0.8%. A validated framework, including strain attenuation maps, to select the effective shear stiffness of an interface material in order to reach different strain attenuation levels, was constructed to provide guidance for general applications.

## **5.2 Future Directions**

### **5.2.1 Control of GLAD Film through Seeding**

During GLAD deposition, first randomly distributed nuclei form on a substrate. To grow ordered GLAD films on a substrate, the substrate is seeded prior to GLAD [35,43]. By controlling the seed dimensions and spacing pattern, the initial shadowing is also controlled and, therefore, GLAD films can be grown with a desired order. For example, the seed dimension and spacing have been shown to affect the major and minor axes of the elliptical cross-section of GLAD nanosprings, and hence their mechanical properties [37]. To assist the effective design of GLAD seeding, a model was derived to relate the seed dimensions to the precise shape and dimensions of GLAD nanostructures. The seed spacing should obey the following relationship for effective shadowing to take place during the GLAD process (e.g. no new seed nucleation and growth between prefabricated seeds), Figure 5.1 [43]:

$$w_s < \Delta \leq h \tan(\alpha) + w_s \quad (5.1),$$

where  $h$  is the seed height,  $w_s$  is the seed width, and  $\Delta$ , is the seed spacing. Given the growth angle,  $\beta$ , GLAD structures begin to grow at a height  $h_2$  ( $h_2 < h$ ) from the top edge of the seed, where  $h_2$  is the distance between the highest and the lowest point of the seed where atoms arrive, Figure 5.1(b).

From geometric relations and the schematics in Figure 5.1(a) and 5.1(b):

$$\Delta = h \tan(\alpha) - w_2 + w_s \quad (5.2),$$

where  $w_2$  is the distance between the edge of the seed and the point which extends from the lowest point of the seed where atoms arrive at the edge of a seed to the surface, and

$$\frac{w_2}{h \tan(\alpha)} = \frac{h - h_2}{h} \quad (5.3).$$

From Equation (5.2),  $w_2$  can be expressed as a function of the seed height,  $h$ , deposition angle,  $\alpha$ , seed width,  $w_s$ , and seed spacing,  $\Delta$ , via:

$$w_2 = h \tan(\alpha) + w_s - \Delta \quad (5.4).$$

Similarly, from Equation (5.3),  $h_2$  can be expressed as a function of the seed height,  $h$ , deposition angle,  $\alpha$ , seed width,  $w_s$ , and seed spacing,  $\Delta$ , via:

$$h_2 = h - \frac{w_2}{\tan(\alpha)} \quad (5.5).$$

By assuming that each seed is perfectly covered by atoms, the major axis of the elliptical cross-section of a GLAD nanocolumn,  $2a$ , is determined by:

$$2a = l_s \quad (5.6),$$

where  $l_s$  is the seed length in Figure 5.1(b). The minor axis of the elliptical cross-section of a GLAD nanocolumn,  $2b$ , can be derived from geometry, Figure 5.1(b):

$$2b = w_s \cos(\beta) + h_2 \sin(\beta) \quad (5.7).$$

By inserting Equation (5.5) into Equation (5.7), the minor axis of the elliptical cross-section of a GLAD nanocolumn,  $2b$ , becomes:

$$2b = w_s \cos(\beta) + \left( h - \frac{h \tan(\alpha) + w_s - \Delta}{\tan(\alpha)} \right) \sin(\beta) \quad (5.8)$$

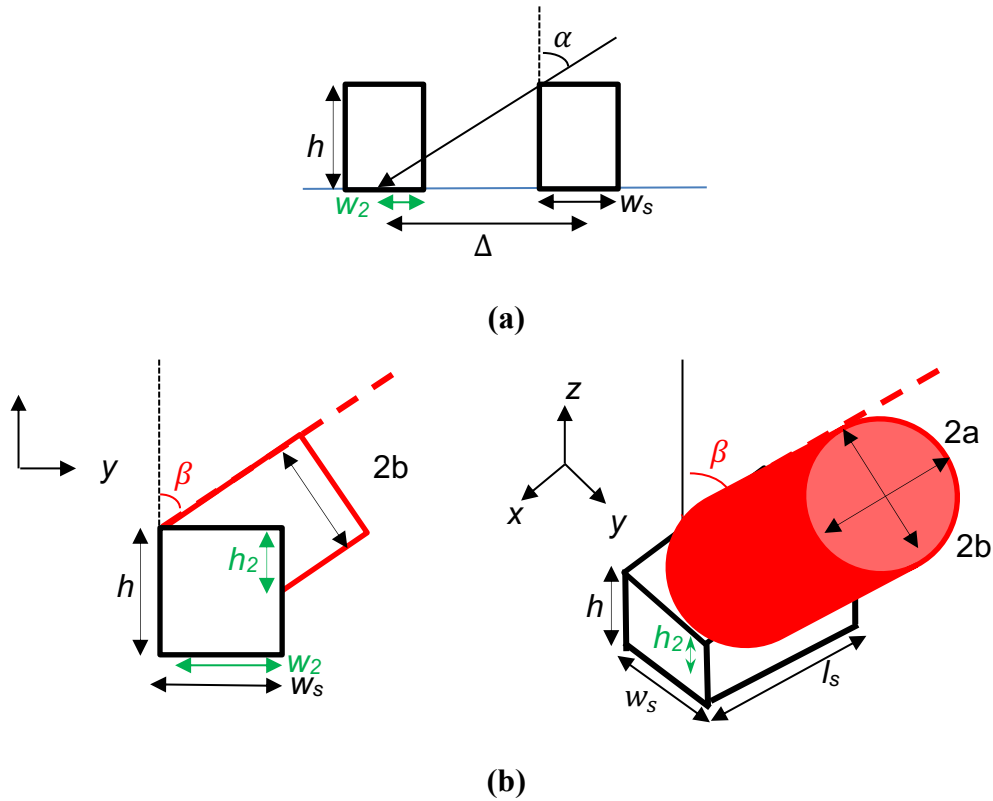


**Figure 5.1** (a) Seed profile. (b) Schematic of GLAD growth of a pillar on a seed illustrating the model assumptions. Black color represents the seed and red color represents a GLAD pillar [43]. Reprinted with permission from IEEE.

To verify the validity of this model, Si nanosprings that were tested before by our group [38] were inspected and compared with model predictions. Si nanosprings were

deposited at an angle  $\alpha = 85^\circ$  on circular Si seeds in a hexagonal pattern. The seeds had 500-nm diameter and 300-nm height,  $h$ , with spacing  $\Delta=900$  nm or  $\Delta=1500$  nm, Figures 5.2(a,b). These seeding parameters were entered into Equations (5.6) and (5.8) to predict the major and minor axes,  $2a$  and  $2b$ , of the Si nanosprings.

The major and minor axes were before measured in [38] with  $\beta$  measured to be  $60^\circ$ . The results are compared with the model predictions Table 5.1: For increasing seed spacing,  $\Delta$ , the minor axis,  $2b$ , also increased which was captured well by the model. However, the model overestimated the minor axis,  $2b$ , by a factor 1.2-1.7. The model predicted that the major axis should be equal to the seed length,  $l_s$ , namely the seed diameter in the case of a circular seed. This prediction worked well in the case of 1500-nm seed spacing, but it overestimated the case of 900-nm seed spacing by a factor of 1.3. This could be due to fewer atoms accumulating on each seed for smaller seed spacing, thus leading to a smaller major axis. Deposition of fewer atoms on each seed would violate the model assumption that each seed is perfectly covered by vapor atoms. In order to predict the major and minor axes, more precisely, future work could incorporate the role material properties such as melting temperature in surface diffusion which takes place during the deposition and influences seed growth.

**Table 5.1** Measurements from [38] vs. model predictions from Equations (5.6) and (5.8).

<b>Seed Spacing (nm)</b>	<b>Major axis (nm)</b>	<b>Minor axis (nm)</b>	<b>Predicted Major axis (nm)</b>	<b>Predicted Minor axis (nm)</b>
<b>900</b>	$380 \pm 10$	$160 \pm 10$	500	280
<b>1500</b>	$470 \pm 25$	$250 \pm 30$	500	320

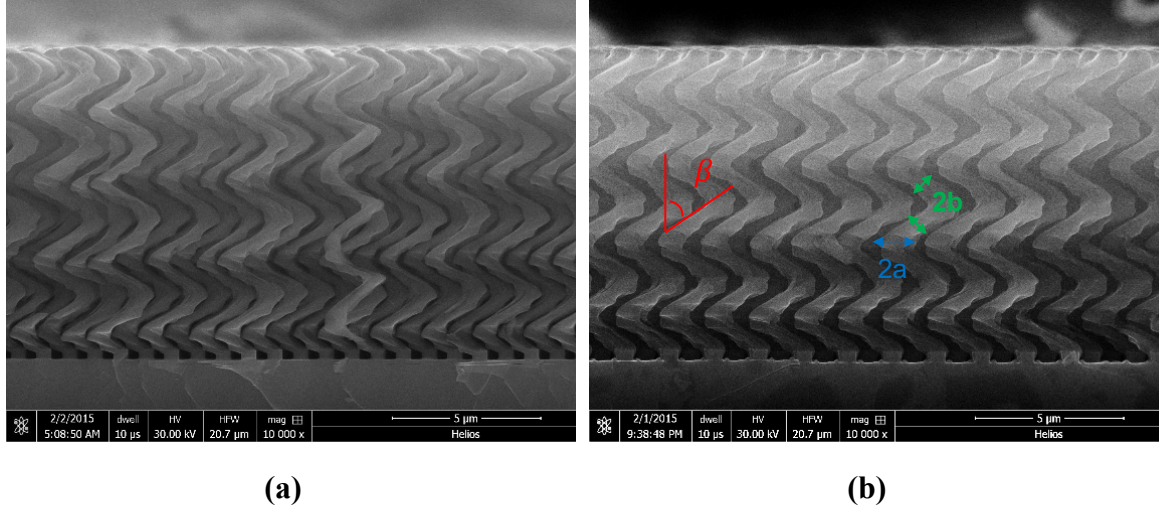


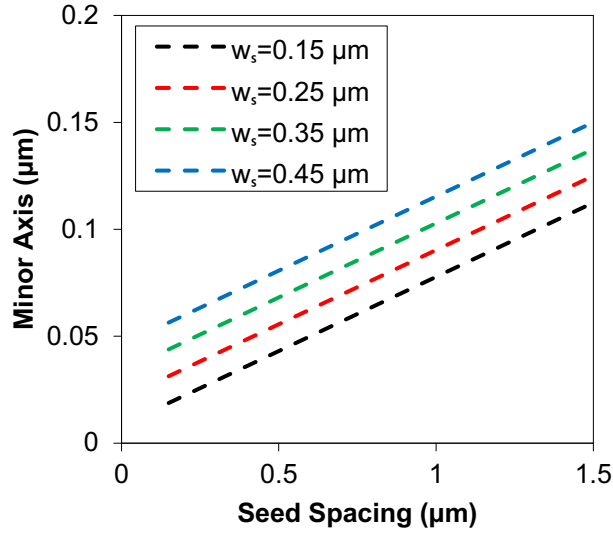
**Figure 5.2** SEM images of Si nanospring films with seed spacing,  $\Delta$ , of (a) 900 nm and (b) 1500 nm from [38]. The inserts in (b) show where  $2a$ ,  $2b$ , and  $\beta$  were measured. Reprinted with permission from Elsevier.

### 5.2.2 Seed Design for GLAD Deposition

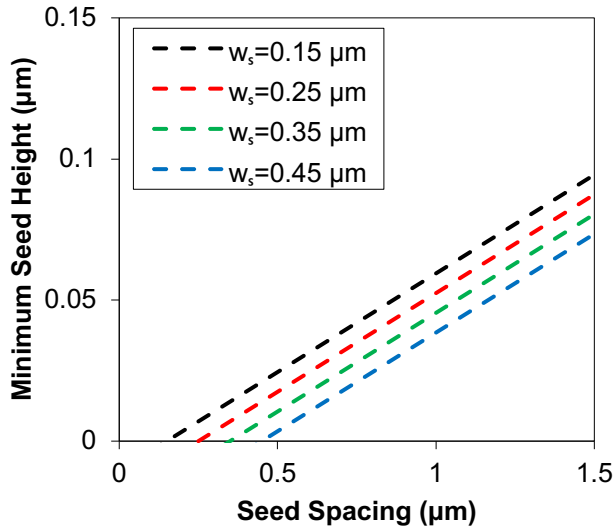
The model in Equations (5.6) and (5.8), was employed to design the seeding of GLAD films. The major axis,  $2a$ , is controlled directly by the seed length,  $l_s$ , Equation (5.6). The minor axis,  $2b$ , vs. seed spacing,  $\Delta$ , and seed width,  $w_s$ , is plotted in Figure 5.3(a) for a given minimum seed height by using Equation (5.8). To create the initial shadowing effect, the minimum height of a seed is determined by  $\alpha$ ,  $w_s$ , and  $\Delta$  from a geometric relation presented by Jensen and Brett [43]:  $\Delta \leq h \tan(\alpha) + w_s$ , and is plotted in Figure 5.3(b). The growth angle,  $\beta$ , was measured to be  $82.8^\circ$  at  $\alpha = 86^\circ$  (Section 3.1) and was used for the calculations for Figure 5.3. From these predictions, smaller  $2a$  and  $2b$  can be achieved by designing smaller  $\Delta$  and seed dimensions. In addition, a larger minimum seed height is needed to ensure a shadowing effect for larger  $\Delta$  and smaller  $w_s$ , Figure 5.3(b).

The model presented in this Section was utilized to design several seed patterns, whose details are listed in Table 5.2. The seed spacing,  $\Delta$ , was varied from 250 nm to 750 nm and the seed diameter was 150 nm or 300 nm. To ensure no structures were grown between seeds, the seed height,  $h$ , was set as 300 nm which is  $\sim 7.5$  times higher than the

minimum seed height required for 750-nm seed spacing and 300-nm seed width, computed via Equation (5.1) and plotted in Figure 5.3(b).



(a)



(b)

**Figure 5.3** (a) Minor axis vs. seed spacing for different seed widths and 0.3-μm seed height for  $\alpha=86^\circ$ ,  $\beta=82.8^\circ$ . (b) Minimum seed height vs. seed spacing with different seed widths and  $\alpha=86^\circ$ ,  $\beta=82.8^\circ$ .

**Table 5.2** Seeding parameters.

Seed Pattern #	Seed height (nm)	Seed diameter (nm)	Seed spacing (nm)
1	300	150	250
2	300	150	550
3	300	300	550
4	300	300	750

Seed patterns with smaller  $\Delta$  and smaller seed diameter were selected to produce more compliant GLAD films compared to previous works by this group [37,38]. Cylindrical seeds were prepared because, in general, GLAD produces circular or elliptical nanocolumn cross-sections irrespective of the actual seed shape [43]. Hence, the seed diameter is used to refer to the seed dimensions in Table 5.2. Tetragonal seed patterns were selected because of their advantage of uniform shadowing effect and the ability to directly measure the geometry of GLAD nanostructures as opposed to a denser hexagonal pattern.

E-beam lithography was used to fabricate 100×100  $\mu\text{m}$  seed patterns. Compared to conventional photolithography, e-beam lithography provides the flexibility of tuning the seed dimensions at the nanometer scale, albeit at a higher cost and for smaller area coverage. E-beam lithography enabled the quick evaluation of GLAD nanostructures before larger seeded areas would be produced by other techniques such as nanoimprint lithography. A JBX-6000FS/E e-beam lithography system equipped with a ZR0/W emitter, was employed for the purposes of this study. The system has a 10 nm resolution on PMMA resist [112]. A 200-nm thick PMMA film was spin coated on a Si wafer, and the seed patterns designed in AUTOCAD were written on the PMMA film with a 50 kV and 1 nA e-beam. A 35-nm Ni layer was deposited as the mask followed by lift-off. The samples were cleaned by oxygen plasma to remove the resist residue. After lift-off, SF<sub>6</sub> and C<sub>4</sub>F<sub>6</sub> were used to etch the 300-nm Si seeds with a ICP-RIE system by using the Bosch process. The wafer and the resist left were cleaned by acetone and Piranha. The seed pattern is shown in Figure 5.4.

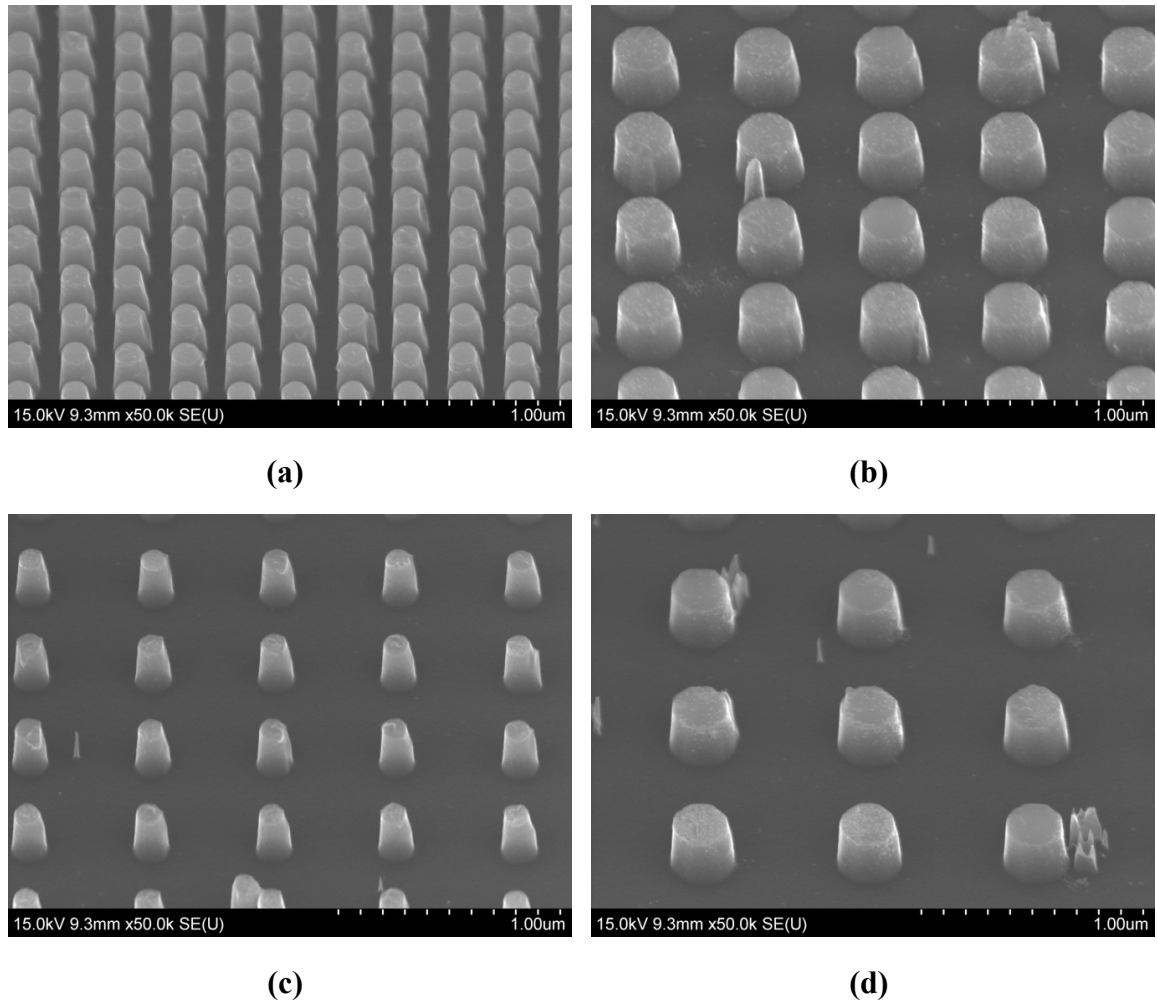


**Figure 5.4** Tetragonal Si Seed Patterns **(a)** #1, **(b)** #2, **(c)** #3 and **(d)** #4 viewed at 52°.

Cu nanochevron films were then grown on the seed patterns at the nominal deposition rate of 10 Å/sec and deposition angle  $\alpha=86^\circ$ , Figure 5.5. As a first step to evaluate the GLAD films, a Focused Ion Beam (FEI Helios) was used to open  $12 \times 6 \mu\text{m}^2$  windows with a depth of 10  $\mu\text{m}$  for cross-sectional imaging, by using 80 pA current to minimize re-deposition during ion milling.

From the cross-sectional FIB images, Figure 5.5, Seed Pattern #4 produced Cu nanochevrons with the largest dimensions, whereas Seed Pattern #1 produced the smallest Cu nanochevrons, as expected from the model in Equations (5.6) and (5.8). The latter films are also expected to be the most compliant. The four seeding cases in Figure

5.5 demonstrated how the model described in this Section could be utilized to provide a first order seed design before larger area production is pursued via other methods. Larger seeded areas would allow for more precise, non-intrusive, measurements of the dimensions of Cu nanochevrons, because a clean cross-section can be generated by cleaving the substrate instead of using a FIB. Mechanical testing of the Cu nanochevron films in Figure 5.5 will shed more light into the effect of seeding on their mechanical compliance.

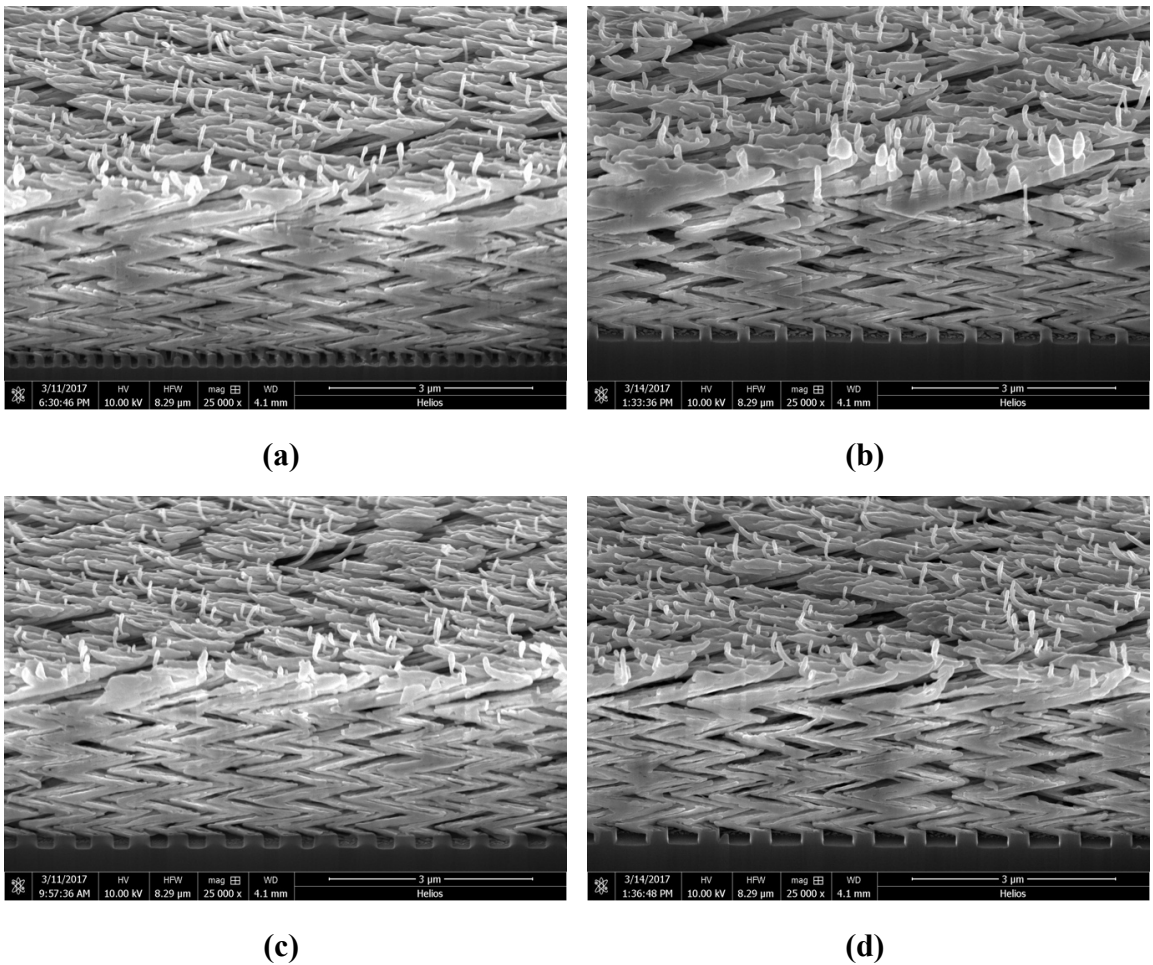


**Figure 5.5** Cu nanochevron films deposited at nominal rate  $10 \text{ \AA}/\text{sec}$  and deposition angle of  $86^\circ$  on Seed Patterns (a) #1, (b) #2, (c) #3 and (d) #4.

# APPENDIX A

## Wrinkle Control

### A.1 Mechanical Properties of PDMS Substrate

Strips of PDMS with dimensions 19×5×2 mm (L×W×T) were cast and tested under uniaxial tension with a Bose ElectroForce 3200 Series III Test Instrument to obtain the elastic modulus,  $E_s$ . The sample surface was speckle-patterned with an airbrush to compute the film strain via Digital Image Correlation (DIC) (Correlated Solutions, SC) from images obtained during testing with a CCD camera at 1 fps. The Young's modulus of films PDMS serving as the substrate was calculated as  $8\pm 0.02$  MPa at 7.5-10% applied strain which is the strain range PDMS was used in this work, Figure A.1.

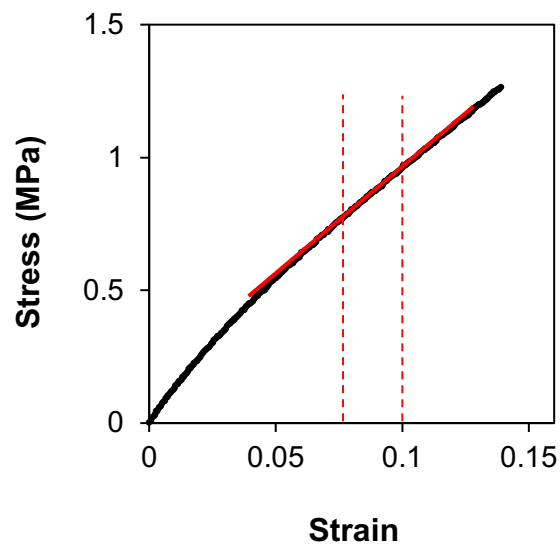


Figure A.1 Small strain response of PDMS substrate.

## A.2 Details of the Wrinkle Problem Formulation

Details of the problem formulation by Allen [33] and Lejeune [77] for a two-layer and a three-layer material system, respectively, are provided in this Appendix. The wrinkle behavior of an isotropic two-layer system is governed by the Föppl–von Kármán equation that describes the large deflection of a thin flat plate on an infinite substrate that is subjected to uniaxial compression [96]:

$$D_1 \frac{d^4 w}{dx^4} - t_f b \sigma_{xx} \frac{d^2 w}{dx^2} = qb = -\frac{w E_s^* n b}{2} \quad (\text{A1}),$$

Under uniaxial compression, a wrinkle pattern of stripes forms, and the film deflection  $w$  can be described by the following sinusoidal form:

$$w = w_o \cos(nx) \quad (\text{A2}),$$

where  $w_o$  is the wrinkle amplitude.

By inserting Equation (A2) into Equation (A1) and minimizing  $\sigma_{xx}$  (by taking the derivative of Equation (A1) with respect to  $n$  after rearranging Equation (A1)), the critical wavenumber,  $n_{cr}$ , at which wrinkling initiates and the corresponding wrinkle wavelength,  $\lambda$ , are calculated as:

$$n_{cr} = \frac{1}{t_f} \left( \frac{3E_s^*}{E_f^*} \right)^{\frac{1}{3}} \quad (\text{A3a}),$$

$$\lambda = \frac{2\pi}{n_{cr}} \quad (\text{A3b}).$$

By inserting Equation (A3a) into Equation (A1) and rewriting  $\sigma_{xx} = E_f^* \varepsilon_c$ , the critical strain,  $\varepsilon_c$ , at wrinkle initiation is found:

$$\varepsilon_c = \frac{1}{4} \left( \frac{3E_s^*}{E_f^*} \right)^{2/3} \quad (\text{A4}).$$

When wrinkling initiates,  $w$  can be related to the difference between the applied strain,  $\varepsilon$ , and the critical strain,  $\varepsilon_c$ , as [113]:

$$\varepsilon - \varepsilon_c = \frac{1}{\lambda} \int_0^\lambda \sqrt{1 + \left(\frac{dw}{dx}\right)^2} dx - 1 \quad (\text{A5}).$$

By inserting Equation (A2) into Equation (A5), the wrinkle amplitude,  $w_0$ , can be found:

$$w_0 = \frac{\lambda}{\pi} \sqrt{\varepsilon - \varepsilon_c} \quad (\text{A6}).$$

The wrinkle behavior of an isotropic three-layer system can also be described by the Föppl–von Kármán equation [96]. Under uniaxial compression, the governing differential equation can be written by treating the interface layer and the top film as a composite layer:

$$D_{c,1} \frac{d^4 w}{dx^4} - (t_i + t_f) b \sigma_{xx} \frac{d^2 w}{dx^2} = q b = -\frac{w E_s^* n b}{2} \quad (\text{A7}),$$

where  $w$  takes the sinusoidal form in Equation (A2). As mentioned in Section 3.2.1, the governing differential equation is solved by a methodology developed by Lejeune et al. [77] for a trilayer material system where the top two layers are modeled as a single composite layer, when the stiffness of the interface material is higher than the substrate stiffness and practically contributes to the stiffness of the top film. Hence, the flexural rigidity of the composite layer is given by  $D_{c,1} = E_i^* I_i + E_f^* I_f$ . The moment of inertia is calculated after finding the bending neutral axis based on the thickness and modulus of the top film and the interface layer [84]. By inserting Equation (A2) into Equation (A7) and minimizing  $\sigma_{xx}$  (by taking the derivative of Equation (A7) with respect to  $n$ , after rearranging Equation (A7) as a function of  $\sigma_{xx}$ ), the critical wavenumber,  $n_{cr}$ , and the corresponding wrinkle wavelength,  $\lambda$ , are calculated as:

$$n_{cr} = \left( \frac{E_s^*}{4(E_i^* I_i + E_f^* I_f)} \right)^{\frac{1}{3}} \quad (\text{A8a}),$$

$$\lambda = \frac{2\pi}{n_{cr}} \quad (\text{A8b}).$$

A similar procedure as in the case of a two-layer system is followed to find the critical strain,  $\varepsilon_c$ . After inserting Equation (A8a) into Equation (A7) and rewriting  $\sigma_{xx} = (E_i^* t_i + E_f^* t_f) \varepsilon_c / (t_i + t_f)$  based on rule of mixture (the top solid film and the interface layer are in the isostrain condition), the critical strain,  $\varepsilon_c$ , can be found:

$$\varepsilon_c = \frac{n_{cr}^2 (E_i^* I_i + E_f^* I_f)}{(E_i^* t_i + E_f^* t_f)} + \frac{E_s^*}{2n_{cr} (E_i^* t_i + E_f^* t_f)} \quad (\text{A9}).$$

Then,  $w_o$  can be calculated from Equation (A6).

When the wrinkle direction is not parallel to the principal stress direction, Figure A.2, the wrinkle profile along the principal stress direction,  $w_l$ , can be described as:

$$w_l = w_o \cos(n_1 x_1) \quad (\text{A10}),$$

where  $n_l$  is the wavenumber along the principal stress direction,  $x_l$ , Figure A.2.

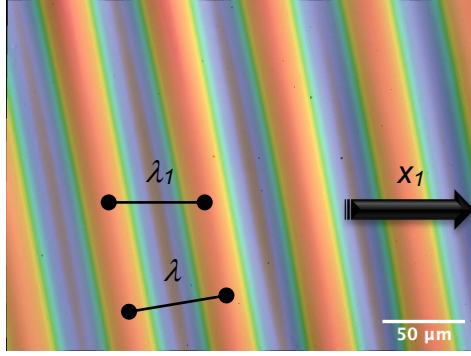


**Figure A.2** Example of wrinkle pattern, based on Figure 3.14(a), in which the wrinkle direction is not parallel to the principal stress direction,  $x_1$ , pointed out by the arrow. The wrinkle direction deviates from principal stress direction by  $\theta_{wp}$ .

When wrinkling initiates,  $w_0$  can be related to the difference between the applied strain,  $\varepsilon$ , and the critical strain,  $\varepsilon_c$ , by using Equation (A5) as:

$$\varepsilon - \varepsilon_c = \frac{1}{\lambda_1} \int_0^{\lambda_1} \sqrt{1 + \left(\frac{dw_1}{dx_1}\right)^2} dx_1 - 1 \quad (\text{A11}),$$

where  $\lambda_1$  is the wrinkle wavelength along the principal stress direction. By inserting Equation (A10) into Equation (A11),  $w_0$  can be found as:

$$w_0 = \frac{\lambda_1}{\pi} \sqrt{\varepsilon - \varepsilon_c} \quad (\text{A12}).$$

### A.3 Wrinkle Wavelength vs. Applied Strain

Plots of measured  $w_0$  vs.  $\varepsilon$  for the specimens listed in Tables 3.2 and 3.4 are given in Figure A.3. It is shown that the  $\lambda$  remains constant, which is expected from Equation (A8) if the elastic modulus of the interface remains constant in the entire range of applied strains. The plots indeed validate this assumption.

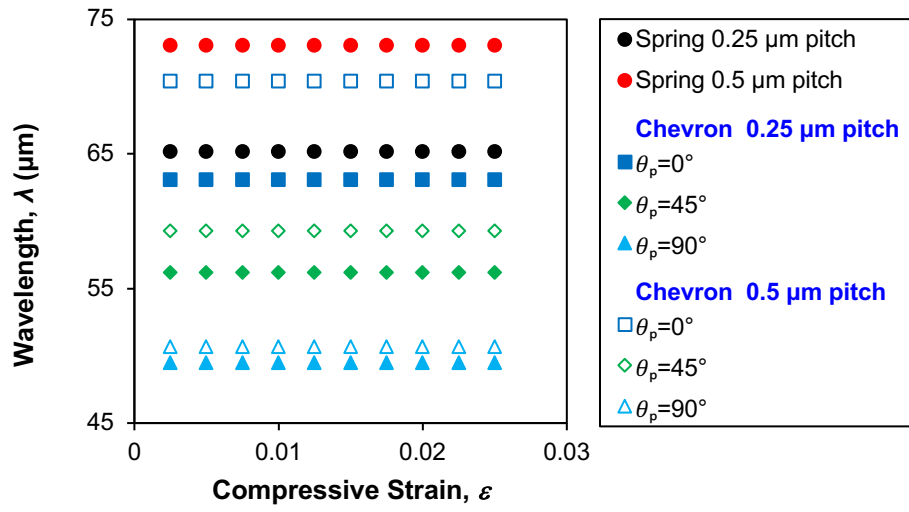


Figure A.3 Wrinkle wavelength vs. compressive strain.

# APPENDIX B

## Strain Attenuation

### B.1 Derivation of Plane Strain Modulus of the CFRP Laminate

In the solution for the stress and strain fields for the three and the two layer composite specimens described in Section 4.1.2, the composite laminate was assumed to be transversely isotropic, Figure B.1. The axes  $x$ ,  $y$ ,  $z$  coincide with the material coordinates of the unidirectional CFRP laminate.

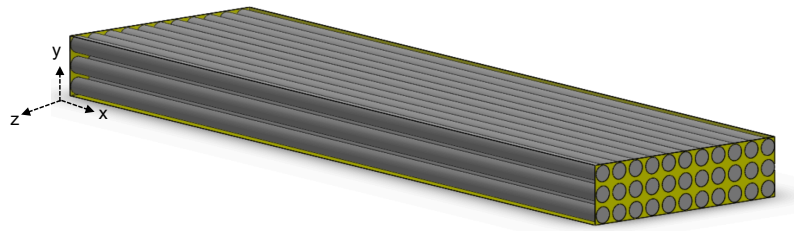


**Figure B.1** Definition of coordinates of the transversely isotropic CFRP laminate.

The stiffness matrix of an orthotropic CFRP laminate is given by:

$$\begin{bmatrix} \varepsilon_{1,xx} \\ \varepsilon_{1,yy} \\ \varepsilon_{1,zz} \\ \varepsilon_{1,yz} \\ \varepsilon_{1,xz} \\ \varepsilon_{1,xy} \end{bmatrix} = \begin{bmatrix} \frac{1}{E_{1,x}} & \frac{-\nu_{1,yx}}{E_{1,y}} & \frac{-\nu_{1,zx}}{E_{1,z}} & 0 & 0 & 0 \\ \frac{-\nu_{1,xy}}{E_{1,x}} & \frac{1}{E_{1,y}} & \frac{-\nu_{1,zy}}{E_{1,z}} & 0 & 0 & 0 \\ \frac{-\nu_{1,xz}}{E_{1,x}} & \frac{-\nu_{1,yz}}{E_{1,y}} & \frac{1}{E_{1,z}} & 0 & 0 & 0 \\ 0 & 0 & 0 & \frac{1}{2G_{1,yz}} & 0 & 0 \\ 0 & 0 & 0 & 0 & \frac{1}{2G_{1,xz}} & 0 \\ 0 & 0 & 0 & 0 & 0 & \frac{1}{2G_{1,xy}} \end{bmatrix} \begin{bmatrix} \sigma_{1,xx} \\ \sigma_{1,yy} \\ \sigma_{1,zz} \\ \sigma_{1,yz} \\ \sigma_{1,xz} \\ \sigma_{1,xy} \end{bmatrix} \quad (\text{B.1}),$$

where  $\nu_{1,xz} = \nu_{1,xy}$ ,  $\nu_{1,yz} = \nu_{1,yx}$ ,  $E_{1,z} = E_{1,y}$ ,  $G_{1,xz} = G_{1,xy}$  and  $\frac{\nu_{1,zx}}{E_{1,z}} = \frac{\nu_{1,xz}}{E_{1,x}}$

Herein, we consider plane strain conditions as the dimension in z-direction is much larger than the dimension in the y-direction:

$$\varepsilon_{1,zz} = \frac{\sigma_{1,zz}}{E_{1,z}} - \sigma_{1,yy} \frac{\nu_{1,zy}}{E_{1,z}} - \sigma_{1,xx} \frac{\nu_{1,xz}}{E_{1,x}} = 0 \quad (\text{B.2}).$$

From Equation (B.2),  $\sigma_{1,zz}$  can be written in terms of  $\sigma_{1,xx}$  and  $\sigma_{1,yy}$  and then inserted into Equation (B.1) to determine  $\varepsilon_{1,xx}$ :

$$\sigma_{1,zz} = E_{1,z} \left( \sigma_{1,yy} \frac{\nu_{1,zy}}{E_{1,z}} + \sigma_{1,xx} \frac{\nu_{1,xz}}{E_{1,x}} \right) \quad (\text{B.3a}),$$

$$\varepsilon_{1,xx} = \frac{\sigma_{1,xx}}{E_{1,x}} - \sigma_{1,yy} \frac{\nu_{1,zx}}{E_{1,z}} - \frac{\nu_{1,xz}}{E_{1,x}} E_{1,z} \left( \sigma_{1,yy} \frac{\nu_{1,zy}}{E_{1,z}} + \sigma_{1,xx} \frac{\nu_{1,xz}}{E_{1,x}} \right) \quad (\text{B.3b}).$$

Equation (B.3b) can then be rearranged as:

$$\frac{E_{1,x}}{1 - \nu_{1,xz}^2 \frac{E_{1,z}}{E_{1,x}}} \varepsilon_{1,xx} = \sigma_{1,xx} - \frac{\nu_{1,xz} \nu_{1,zy} + \nu_{1,xz}}{1 - \nu_{1,xz}^2 \frac{E_{1,z}}{E_{1,x}}} \sigma_{1,yy} = 0 \quad (\text{B.4}).$$

Based on Hooke's law and the form of Equation (B.4), the plane strain modulus,  $E_{1,x}^*$ , Poisson's ratio,  $\nu_{1,xy}^*$ , of the CFRP laminate are:

$$E_{1,x}^* = \frac{E_{1,x}}{1 - \nu_{1,xz}^2 \frac{E_{1,z}}{E_{1,x}}}$$

$$\nu_{1,xy}^* = \frac{\nu_{1,xz} \nu_{1,zy} + \nu_{1,xz}^2 \frac{E_{1,z}}{E_{1,x}}}{1 - \nu_{1,xz}^2 \frac{E_{1,z}}{E_{1,x}}}$$
(B.5).

This result for the plane strain modulus,  $E_{1,x}^*$ , and Poisson's ratio,  $\nu_{1,xy}^*$ , of a CFRP laminate can be also found in [114].

Assuming isostrain conditions, the micromechanical theory of rule-of-mixtures (ROM) and the isotropic properties for the matrix can be used to calculate the Young's modulus,  $E_{1,z}$ , Poisson's ratio,  $\nu_{1,zy}$ , and shear modulus,  $G_{1,xy}$ , of the CFRP laminate as follows:

$$E_{1,z} = \frac{1}{\frac{V_f}{E_f} + \frac{V_m}{E_m}}$$

$$\nu_{1,zy} = \nu_f V_f + \nu_m V_m$$
(B.6),

$$G_{1,xy} = \frac{1}{\frac{V_f}{G_f} + \frac{V_m}{G_m}}$$

where  $V_f$  and  $V_m$  are the volume fractions of the fiber and the matrix in the CFRP laminate, respectively, and were calculated as 0.32 and 0.68, respectively, by using  $E_{1,x} = E_f V_f + E_m V_m$  with the experimental input of  $E_{1,x}=82.8$  GPa. The plane strain shear modulus,  $G_{1,xy}^*$ , of the CFRP laminate is  $G_{1,xy}^* = G_{1,xy}$ . According to the manufacturers' data sheets, the elastic moduli of the fiber and the matrix,  $E_f$  and  $E_m$ , are 250 GPa [115] and 3.3 GPa [116], respectively. The Poisson's ratios of the fiber and the matrix,  $\nu_{f,zy}$  and  $\nu_m$ , have been reported as 0.3 [117] and 0.32 [116], respectively. Then, the shear modulus of the matrix,  $G_m$ , was calculated as 1.28 GPa by assuming isotropic

properties for the matrix. The transverse modulus,  $E_{f,z}$ , and the shear modulus,  $G_{f,xy}$ , of the fiber have been reported to be 8 GPa and 27.3 GPa, respectively [117]. The calculated properties of the CFRP laminate are given in Table B.1.

**Table B.1** Material properties of composite laminate, calculated by Equations (B.6).

$E_{1,z}$ (GPa)	$G_{1,xy}$ (GPa)	$\nu_{1,zy}$
4.06	1.84	0.31

The PDMS interface material and the PV film are considered isotropic. Their plane strain modulus,  $E_i^*$ , Poisson's ratio,  $\nu_i^*$ , and shear modulus,  $G_i^*$ , are given by:

$$E_i^* = \frac{E_i}{1 - \nu_i^2}, G_i^* = G_i = \frac{E_i}{2(1 + \nu_i)}, \nu_i^* = \frac{\nu_i}{1 - \nu_i}, \text{ for } i = 2 \text{ and } 3 \quad (\text{B.7}).$$

The values of  $E_3$  and  $\nu_3$  can be found in Table 4.1 and  $G_3$  was calculated to be 4 GPa.  $E_2$  can be found in Table 4.2. Similarly,  $G_2$  was calculated to be 0.29 MPa, 0.15 MPa, 0.03 MPa for  $E_2$  is equal to 0.87 MPa, 0.46 MPa, 0.1 MPa, respectively with  $\nu_2=0.499$ .

## B.2 Parameters in Stress and Strain Field Solution of Three-layer System

The stress field parameters for the CFRP laminate layer are:

$$b_1 = \sqrt{K \left( -\nu_{1,xy}^* + \frac{E_{1,x}^*}{G_{1,xy}^*} \right)}, b_i = \sqrt{K(2 + \nu_i^*)} \text{ for } i = 2, 3 \quad (\text{B.8}).$$

$$n_i = \sqrt{K} \text{ for } i = 1, 2, 3$$

$$P_1 = \left( \frac{St_1 - St_1^2}{\frac{E_2^*}{E_{1,x}^*} t_2 + \frac{E_3^*}{E_{1,x}^*} t_3 + t_1} \right) \left( \frac{n_1}{\cosh \frac{n_1 l}{2} \sin b_1 t_1} \right), \quad E = \frac{St_1}{\frac{E_2^*}{E_{1,x}^*} t_2 + \frac{E_3^*}{E_{1,x}^*} t_3 + t_1}$$

$$h_1 = \frac{-n_2 \cosh n_2 x (M \cos b_2 t_1 - N \sin b_2 t_1)}{b_2} + \frac{P_1 n_1 \cosh n_1 x \cos b_1 t_1}{b_1} + h_2$$

The stress field parameters for the PDMS interface layer are:

$$N = \left( \frac{P_1 \sin b_1 t_1}{\frac{f_2}{f_1} \sin b_2 t_1 + \cos b_2 t_1} \right), \quad M = \frac{N f_2}{f_1}, \quad F = \frac{E E_2^*}{E_{1,x}^*}, \quad h_3 = \frac{-P_3 n_3 \cosh n_3 x}{b_3}$$

$$h_2 = \frac{n_2 \cosh n_2 x (M \cos b_2 (t_1 + t_2) - N \sin b_2 (t_1 + t_2))}{b_2} + \frac{P_3 n_3 \cosh n_3 x \cos b_3 t_3}{b_3} + h_3$$

$$f_1 = -\frac{b_3 \sin b_2 (t_1 + t_2)}{E_3^* n_3 \tan b_3 t_3} - \frac{b_2 \cos b_2 (t_1 + t_2)}{E_2^* n_2} + \frac{n_3}{b_3} \left( \frac{\nu_3^*}{E_3^*} - \frac{\nu_2^*}{E_2^*} \right) \left( \frac{1}{\sin b_3 t_3} - \frac{1}{\tan b_3 t_3} \right) \sin b_2 (t_1 + t_2) \quad (\text{B.9.})$$

$$f_2 = \frac{b_3 \cos b_2 (t_1 + t_2)}{E_3^* n_3 \tan b_3 t_3} - \frac{b_2 \sin b_2 (t_1 + t_2)}{E_2^* n_2} - \frac{n_3}{b_3} \left( \frac{\nu_3^*}{E_3^*} - \frac{\nu_2^*}{E_2^*} \right) \left( \frac{1}{\sin b_3 t_3} - \frac{1}{\tan b_3 t_3} \right) \cos b_2 (t_1 + t_2)$$

Finally, the stress field parameters for the PV layer are:

$$P_3 = \frac{N \left( \frac{f_2 \sin b_2 (t_1 + t_2)}{f_1} + \cos b_2 (t_1 + t_2) \right)}{\sin b_3 t_3}, \quad G = \frac{E E_3^*}{E_{1,x}^*}, \quad (\text{B.10.})$$

The parameter  $K$  in (B.8) is found numerically by solving the following equation [78]:

$$\begin{aligned}
& \frac{\sqrt{2 + \nu_{1,xy}^*} \left( \frac{f_2 \sin b_2 t_1}{f_1} + \cos b_2 t_1 \right)}{E_{1,x}^* \tan b_1 t_1} \\
&= \frac{\sqrt{2 + \nu_2^*} \left( \frac{f_2 \cos b_2 t_1}{f_1} - \sin b_2 t_1 \right)}{E_2^*} - \left( \frac{\nu_{1,xy}^*}{E_{1,x}^*} \right. \\
&- \frac{\nu_2^*}{E_2^*} \left. \left( \frac{\frac{f_2 \cos b_2 t_1}{f_1} - \sin b_2 t_1 - \frac{f_2 \cos b_2 (t_1 + t_2)}{f_1} + \sin b_2 (t_1 + t_2)}{\sqrt{2 + \nu_2^*}} \right) \right) \\
&+ \frac{\left( \frac{f_2 \sin b_2 (t_1 + t_2)}{f_1} + \cos b_2 (t_1 + t_2) \right) \left( \frac{1}{\sin b_3 t_3} - \frac{1}{\tan b_3 t_3} \right)}{\sqrt{2 + \nu_3^*}}
\end{aligned} \tag{B.11}$$

The solution for  $K$  can be found graphically as the first root of Equation (B.11) in Figure B.2 following the approach in [78]:

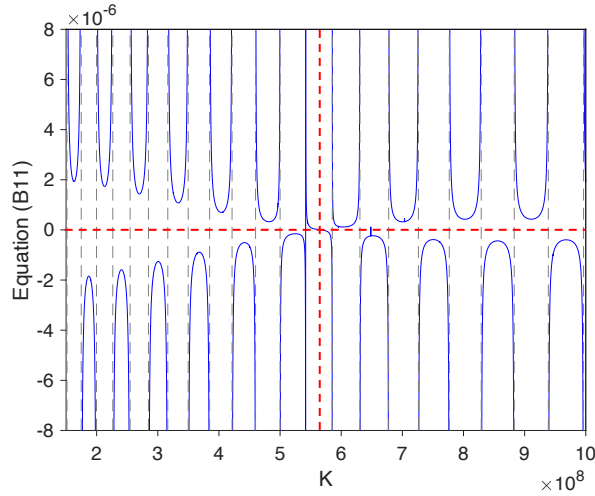


**Figure B.2** Equation (B.11) as function of  $K$ . This graphical solution gives  $K = 5.67 \cdot 10^8$  for  $L = 2.6$  cm,  $E_2 = 0.46$  MPa,  $t_2 = 46$   $\mu$ m, and  $E_3$ ,  $t_3$ ,  $E_{l,x}$ , and  $t_l$  taking values from Table 4.1.

### B.3 Effect of Material System Parameters on Strain Attenuation

The effective shear stiffness of the interface layer controlling the strain attenuation depends on the elastic modulus and thickness of the material system, namely  $E_{1,x}$ ,  $t_1$ ,  $E_3$ , and  $t_3$  which are defined in Chapter 4. A parametric study of the effect of each of the aforementioned parameters on strain attenuation is provided in this Section. The length of the PV film,  $L$ , is assumed to be 7.6 cm.  $E_2/t_2$  is used as the control parameter in the range 0.02-2000 MPa/mm. The values of  $E_{1,x}$ ,  $t_1$ ,  $E_3$ , and  $t_3$ , based on the specific material system in this study, are given in Table 4.1. As the starting point  $E_3t_3/E_{1,x}t_1$  is calculated as 0.0034. As shown in Figure B.3, higher strain attenuation is achieved for smaller values of  $E_2/t_2$ . The range of values for  $E_2/t_2$  can be varied by either changing  $E_2$  or  $t_2$ , but it is found that the same strain attenuation is achieved if  $E_2/t_2$  remains constant. This result demonstrated the effectiveness of  $E_2/t_2$  as the control parameter for the strain attenuation.

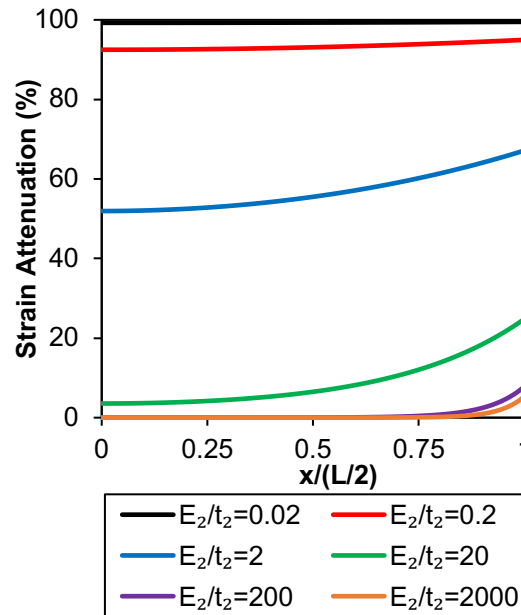


**Figure B.3** Strain attenuation for  $E_3t_3/E_{1,x}t_1 = 0.0034$  for a 7.6-cm long PV module. The units of  $E_2/t_2$  are MPa/mm.

The effect of  $E_3$  alone on the strain attenuation is demonstrated by increasing and decreasing  $E_3$  by ten times with respect to the reference value in Table 4.1. A comparison of the strain attenuation plots in Figures B.3, B.4(a), and B.4(b) shows that larger  $E_3$  results in higher strain attenuation for the same values of  $E_2/t_2$ . Similarly, the effect of  $t_3$  alone on strain attenuation is demonstrated in Figures B.5(a,b) by decreasing and increasing  $t_3$  by ten times with respect to the reference value in Table 4.1. A comparison with the plots in Figure B.3 shows that larger  $t_3$  results in higher strain attenuation for the same values of  $E_2/t_2$ .

From the plots in Figures B.4 and B.5, it is deduced that  $E_3$  and  $t_3$  have the same effect on the strain attenuation. Furthermore, as shown in Figure B.6, strain attenuation remains unchanged for the same value of  $E_2/t_2$  if the product of  $E_3t_3$  is held constant, e.g.  $E_3$  is increased by ten times while  $t_3$  is reduced by ten times. Hence, the combined effect of  $E_3$  and  $t_3$  was considered in this dissertation research through the product  $E_3t_3$ .

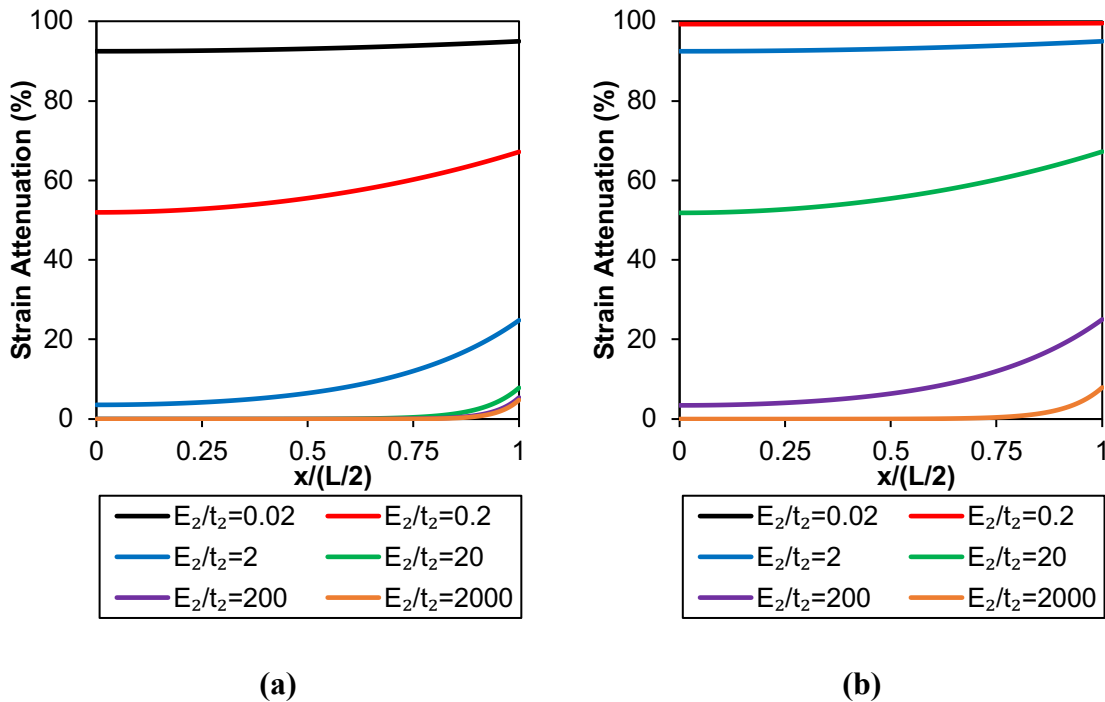


**Figure B.4** Strain attenuation for **(a)**  $E_3t_3/E_{1,x}t_1 = 0.00034$ , and **(b)**  $E_3t_3/E_{1,x}t_1 = 0.034$  by varying the value of  $E_3$  of a 7.6-cm long PV module. The units of  $E_2/t_2$  are MPa/mm.

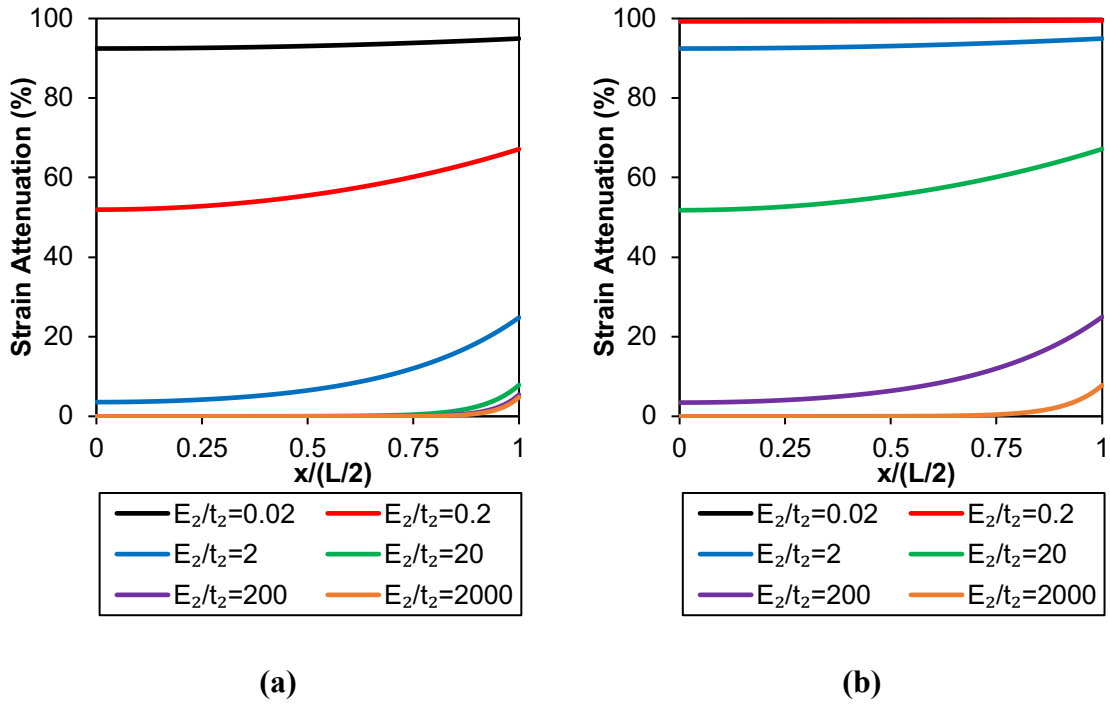


**Figure B.5** Strain attenuation for (a)  $E_3t_3/E_{1,x}t_1 = 0.00034$ , and (b)  $E_3t_3/E_{1,x}t_1 = 0.034$  by varying  $t_3$  of a 7.6-cm long PV module. The units of  $E_2/t_2$  are MPa/mm.

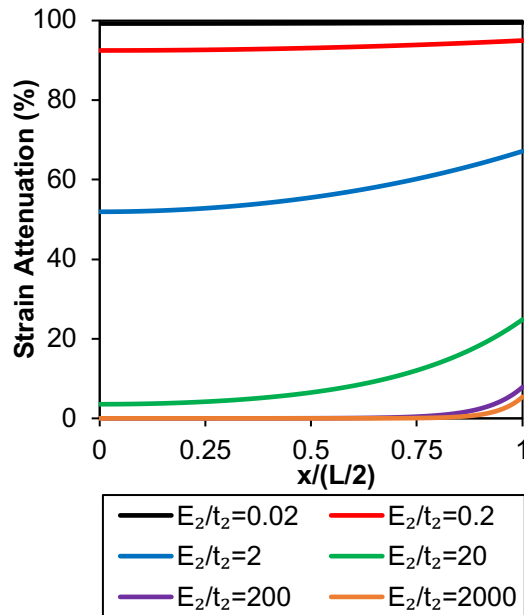


**Figure B.6** Strain attenuation for a 7.6-cm long PV module where  $E_3t_3/E_{1,x}t_1$  is kept equal to 0.0034 by simultaneously varying  $E_3$  and  $t_3$ . The units of  $E_2/t_2$  are MPa/mm.

The same procedure is used to evaluate the effect of  $E_{1,x}$  and  $t_l$  on strain attenuation. When the value of  $E_3t_3/E_{1,x}t_l$  is small, namely the effective substrate stiffness,  $E_{1,x}t_l$ , is much larger than the effective stiffness of the PV film,  $E_3t_3$ , variation of  $E_{1,x}$  and  $t_l$  has no effect on strain attenuation, as shown by comparison of Figures B.7(a) and B.7(b).

When the value of  $E_3t_3/E_{1,x}t_l$  becomes larger than  $0.51^1$ ,  $E_{1,x}$  and  $t_l$  begin to have an effect on strain attenuation. Smaller values of  $E_{1,x}$  and  $t_l$  decreased strain attenuation as shown in Figure B.8 where  $E_3t_3/E_{1,x}t_l \geq 0.51$ . These results show that if the effective substrate stiffness,  $E_{1,x}t_l$ , is comparable to the effective stiffness of the PV film,  $E_3t_3$ , then the effect of  $E_{1,x}$  and  $t_l$  must be taken into account. In this case, the CFRP laminate substrate no longer serves as the only load-bearing member.

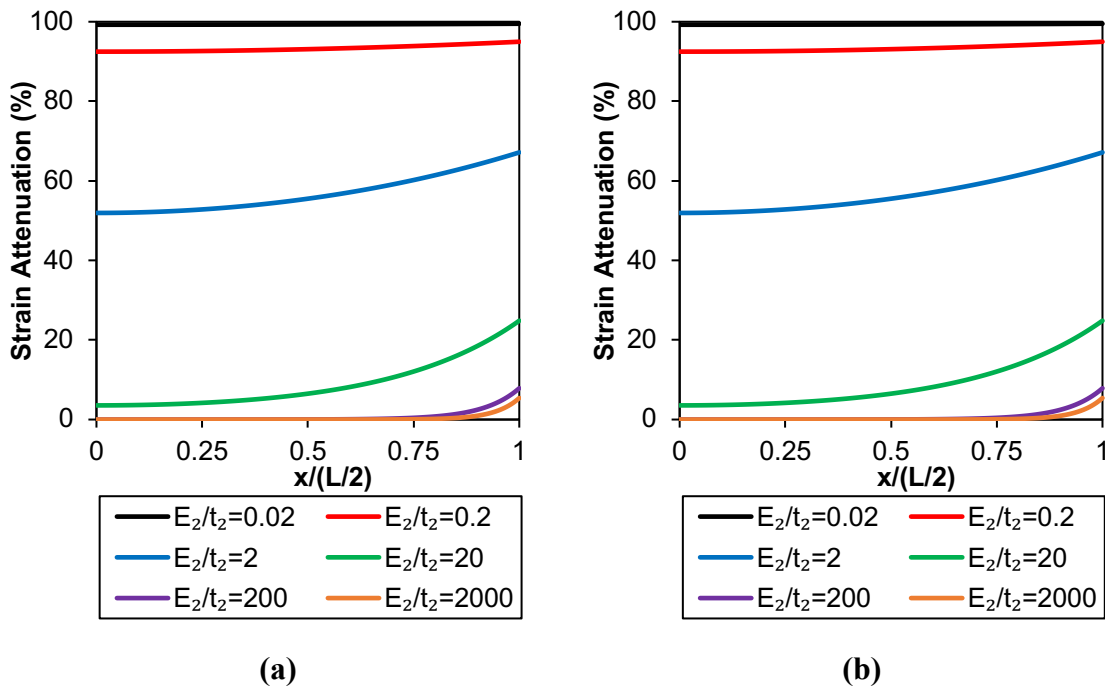


**Figure B.7** The same strain attenuation as in Figure B.3 is achieved for (a)  $E_3t_3/E_{1,x}t_l = 0.00034$  or (b)  $E_3t_3/E_{1,x}t_l = 0.34$  by either varying  $E_{1,x}$  or  $t_l$  of a 7.6-cm long PV module. The units of  $E_2/t_2$  are MPa/mm.

<sup>1</sup> The value of 0.51 was determined by iteratively solving for strain attenuation in Matlab. See also Chapter 4.

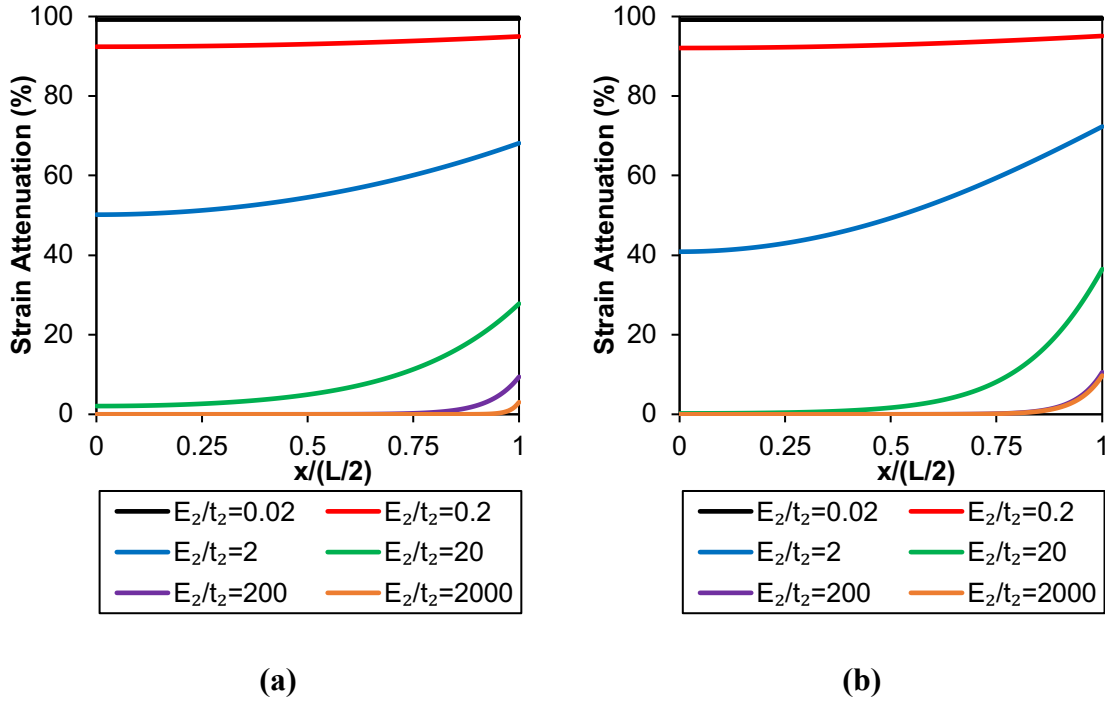


**Figure B.8** Strain attenuation for (a)  $E_3t_3/E_{1,x}t_1 = 0.51$  and (b)  $E_3t_3/E_{1,x}t_1 = 3.4$  by either varying  $E_{1,x}$  or  $t_1$  for a 7.6-cm long PV module. The units of  $E_2/t_2$  are MPa/mm.

In the elasticity model by Li et al. [78],  $t_1$  must be much smaller than the length of the PV film,  $L$ . Hence, the upper bound of  $t_1$  must be identified. It can be shown the calculation of strain attenuation at the center of the PV module is no longer accurate when  $t_1$  becomes sixteen times larger than its value in Table 4.1, namely  $t_1 = 0.4L$ . For the given material system, the strain attenuation changes from 52% to 56% for  $E_2/t_2 = 2$  MPa/mm when  $t_1 = 0.4L$ , Figure B.9, whereas for any  $t_1 < 0.4L$ , the model computes the same value for strain attenuation (52% in this case).

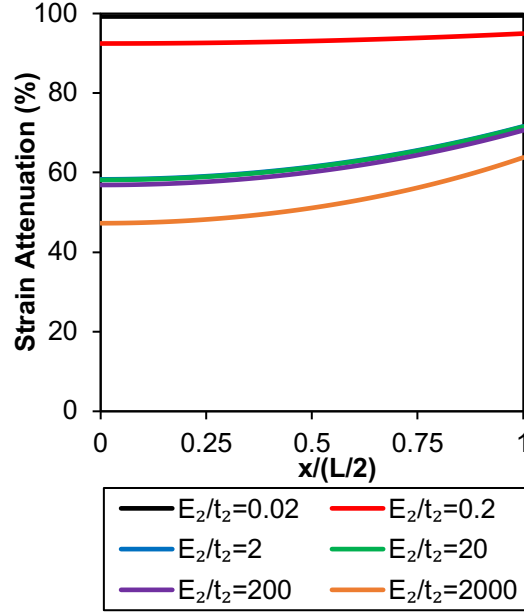


**Figure B.9** Strain attenuation for  $E_3t_3/E_{1,x}t_1 = 0.00021$  by increasing  $t_1$  sixteen times its value in Table 4.1 in a 7.6-cm long PV module. The units of  $E_2/t_2$  are MPa/mm.

The individual effect of  $E_{1,x}$ ,  $t_1$ ,  $E_3$ , and  $t_3$  on strain attenuation of the material system at hand was demonstrated by the aforementioned calculations. When variation of  $E_1$  or  $t_1$  has an effect on strain attenuation, namely when  $E_3t_3/E_{1,x}t_1 \geq 0.51$ , then it is important to compare their effect to that of  $E_3$  and  $t_3$ . This is examined in Figure B.10(a) by first setting  $E_3t_3/E_{1,x}t_1 = 5.1$  by decreasing  $t_1$  by 1500 times its reference value in Table 4.1. By comparison to Figure B10(a), Figures B.10(b) and B.10(c) show that  $t_3$  has a different effect on strain attenuation than  $t_1$ , by *further* increasing  $t_3$  and  $t_1$  by ten times, respectively. Specifically, for the same value of  $E_2/t_2$ , increasing  $t_3$  resulted in higher strain attenuation than increasing  $t_1$ . This is further shown in Figure B.10(d) by increasing  $t_3$  and decreasing  $t_1$  at the same time by a factor of 10 with respect to their values in Figure B10(a), therefore  $E_3t_3/E_{1,x}t_1 = 510$ . In this case the strain attenuation decreased from 35% to 3.4% for  $E_2/t_2 = 2$  MPa/mm because of the more significant effect of  $t_3$  than  $t_1$ .

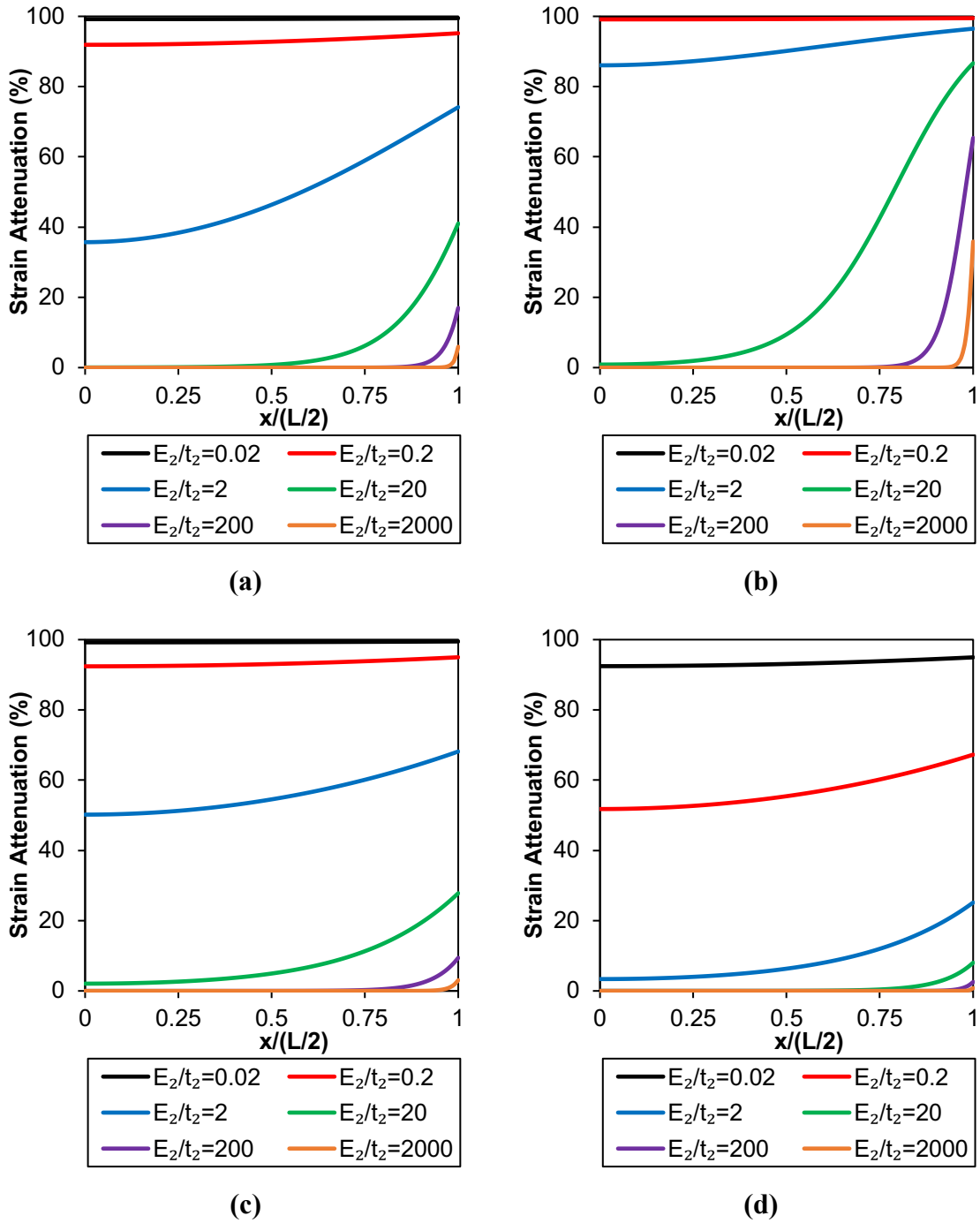


**Figure B.10** Strain attenuation for a 7.6-cm long PV module and (a)  $E_{3t_3}/E_{1,xt_1} = 5.1$  by decreasing  $t_1$  by 1500 times its value in Table 4, (b)  $E_{3t_3}/E_{1,xt_1} = 51$  and (c)  $E_{3t_3}/E_{1,xt_1} = 0.51$  by increasing  $t_3$  by 10 times and by increasing  $t_1$  by 10 times their given values in (a), respectively. (d) Strain attenuation for  $E_{3t_3}/E_{1,xt_1} = 510$  by increasing  $t_1$  by 10 times while decreasing  $t_3$  by 10 times their given values in (a). The units of  $E_2/t_2$  are MPa/mm.

In the problem formulation described in Chapter 4, the 3D problem was simplified into a 2D problem by adopting plane strain conditions. Alternatively, plane stress conditions, namely no stress in the y direction, Figure 4.1(a), could also be adopted to simplify the problem. In this case, the elastic modulus,  $E$ , and Poisson's ratios,  $\nu$ , of each layer are directly entered into the model. For a given value of  $E_2/t_2$  the strain attenuation model predictions, assuming plane stress conditions, differ by less than 3% from the predictions made under plane strain conditions.

## References

- [1] D. Antartis, R. Mott, D. Das, D. Shaddock, and I. Chasiotis, “Cu Nanospring Films for Advanced Nanothermal Interfaces”, *Advanced Engineering Materials*, 20(3), pp. 1700910, (2018).
- [2] J. Lintymer, N. Martin, J. M. Chappe, P. Delobelle, and J. Takadoum. “Influence of Zigzag Microstructure on Mechanical and Electrical Properties of Chromium Multilayered Thin Films”, *Surface and Coatings Technology*, 180, pp. 26-30, (2004).
- [3] Y. Yao, J. N. Tey, Z. Li, J. Wei, K. Bennett, A. McNamara, Y. Joshi, R. Tan, Nai. Ling, and C. P. Wong, “High-Quality Vertically Aligned Carbon Nanotubes for Applications as Thermal Interface Materials”, *IEEE Transactions on Components, Packaging and Manufacturing Technology*, vol. 4, no. 2, pp. 232–239, (2014).
- [4] T. Sumigawa, T. Sueda, Y. Futamura, M. Suzuki and T. Kitamura, “Effect of interface layer consisting of nanosprings on stress field near interface edge”, *Engineering Fracture Mechanics*, 76(9), pp. 1338, (2009).
- [5] T. Sumigawa, H. Hirakata, M. Takemura, S. Matsumoto, M. Suzuki, and T. Kitamura, “Disappearance of stress singularity at interface edge due to nanostructured thin film”, *Engineering Fracture Mechanics*, 75(10), pp. 3079, (2008).
- [6] K. M. Razeeb, E. Dalton, G. L. Cross, and A. J. Robinson, “Present and future thermal interface materials for electronic devices”, *International Materials Reviews*, 63(1), pp. 1-21, (2017).
- [7] L. Ge, L. Ci, A. Goyal, R. Shi, L. Mahadevan, P. M. Ajayan, and A. Dhinojwala, “Cooperative Adhesion and Friction of Compliant Nanohairs”, *Nano Letters*, 10(11), pp. 4509-4513, (2010).
- [8] Y. Zhang, J. Zheng, C. Fang, Z. Li, X. Zhao, Y. Li, and Y. Dai, “Enhancement of silicon-wafer solar cell efficiency with low-cost wrinkle antireflection coating of polydimethylsiloxane”, *Solar Energy Materials and Solar Cells*, 181, pp. 15-20, (2018).
- [9] Y. Rahmawan, M. Moon, K. Kim, K. Lee, and K. Suh, “Wrinkled, Dual-Scale Structures of Diamond-Like Carbon (DLC) for Superhydrophobicity”, *Langmuir*, 26(1), pp. 484-491, (2009).
- [10] A. Perez-Rosado, R. D. Gehlhar, S. Nolen, S. K. Gupta, and H. A. Bruck, “Design, fabrication, and characterization of multifunctional wings to harvest solar energy in flapping wing air vehicles”, *Smart Materials and Structures*, 24(6), pp. 065042-1-15, (2015).
- [11] K. K. Hung and I. Chasiotis, “Control of Surface Wrinkling through Compliant Nanostructured Interfaces”, *Advanced Materials Interfaces*, pp. 2101583, (2021).
- [12] K. K. Hung and I. Chasiotis, “Control of substrate strain transfer to thin film photovoltaics via interface design”, *Solar Energy*, 225, pp.643-655, (2021)
- [13] S. F. Yin, B. Li, Y. P. Cao, and X.Q. Feng, “Surface wrinkling of anisotropic films bonded on a compliant substrate”, *International Journal of Solids and Structures*, 141-142, pp. 219–231, (2018).
- [14] N. Bowden, S. Brittain, A. G. Evans, J. W. Hutchinson, and G. M. Whitesides, “Spontaneous formation of ordered structures in thin films of metals supported on an elastomeric polymer”, *Nature*, 393(6681), pp. 146–149, (1998).

- [15] G. C. Martin, T. T. Su, I. H. Loh, E. Balizer, S. T. Kowel, and P. Kornreich, “The metallization of silicone polymers in the rubbery and the glassy state”, *Journal of Applied Physics*, 53(1), pp. 797-799, (1982).
- [16] V. Tolpygo, and D. Clarke, “Wrinkling of  $\alpha$ -alumina films grown by thermal oxidation-I. Quantitative studies on single crystals of Fe–Cr–Al alloy”, *Acta Materialia*, 46(14), pp. 5153-5166, (1998.)
- [17] P. Lin, and S. Yang, “Spontaneous formation of one-dimensional ripples in transit to highly ordered two-dimensional herringbone structures through sequential and unequal biaxial mechanical stretching”, *Applied Physics Letters*, 90(24), pp. 241903-1-3, (2007).
- [18] X. Chen, and J. W. Hutchinson, “Herringbone Buckling Patterns of Compressed Thin Films on Compliant Substrates”, *Journal of Applied Mechanics*, 71(5), pp. 597-603, (2004).
- [19] J. Lee, H. W. Ro, R. Huang, P. Lemaillet, T. A. Germer, C. L. Soles, and C. M. Stafford, “Anisotropic, Hierarchical Surface Patterns via Surface Wrinkling of Nanopatterned Polymer Films”, *Nano Letters*, 12(11), pp. 5995-5999, (2012).
- [20] Z. Huang, W. Hong, and Z. Suo, “Evolution of wrinkles in hard films on soft substrates”, *Physical Review E*, 70(3), pp. 030601-1-4, (2004).
- [21] S. Im, and R. Huang, “Wrinkle patterns of anisotropic crystal films on viscoelastic substrates”, *Journal of the Mechanics and Physics of Solids*, 56(12), pp. 3315-3330, (2008).
- [22] Y. Wang, Q. Liu, J. Zhang, T. Hong, W. Sun, L. Tang, and C. F. Guo, “Giant Poissons Effect for Wrinkle-Free Stretchable Transparent Electrodes”, *Advanced Materials*, 31(35), pp. 1902955-1-8, (2019).
- [23] T. R. Hendricks, W. Wang, and I. Lee, “Buckling in nanomechanical films”, *Soft Matter*, 6(16), pp. 3701-3706, (2010).
- [24] J. B. Kim, P. Kim, N. C. Pégard, S. J. Oh, C. R. Kagan, J. W. Fleischer, and Y. L. Loo, “Wrinkles and deep folds as photonic structures in photovoltaics”, *Nature Photonics*, 6(5), pp. 328–329, (2012).
- [25] C. Harrison, C. M. Stafford, W. Zhang, and A. Karim, “Sinusoidal phase grating created by a tunably buckled surface”, *Applied Physics Letters*, 85(18), pp. 4016-4018, (2004).
- [26] Z. Zhang, T. Zhang, Y. W. Zhang, K. Kim, and H. Gao, “Strain-Controlled Switching of Hierarchically Wrinkled Surfaces between Superhydrophobicity and Superhydrophilicity”, *Langmuir*, 28(5), pp. 2753-2760, (2012).
- [27] D. Nguyen, V. H. Pham, V. T. Truong, I. Sbarski, J. Wang, A. Balčytis, S. Juodkazis, D. Mainwaring, R. Crawford, and E. Ivanova, “Role of topological scale in the differential fouling of *Pseudomonas aeruginosa* and *Staphylococcus aureus* bacterial cells on wrinkled gold-coated polystyrene surfaces”, *Nanoscale*, 10(11), pp. 5089-5096, (2018).
- [28] P. Kim, Y. Hu, J. Alvarenga, M. Kolle, Z. Suo, and J. Aizenberg, “Rational Design of Mechano-Responsive Optical Materials by Fine Tuning the Evolution of Strain-Dependent Wrinkling Patterns”, *Advanced Optical Materials*, 1(5), pp. 381-388, (2013).

- [29] J. Moon, E. Kim, S. K. Park, K. Lee, J. W. Shin, D. H. Cho, and J. I. Lee, “Organic wrinkles for energy efficient organic light emitting diodes”, *Organic Electronics*, 26, pp. 273-278, (2015).
- [30] D. Khang, H. Jiang, Y. Huang, and J. A. Roger, “A Stretchable Form of Single-Crystal Silicon for High-Performance Electronics on Rubber Substrates”, *Science* 311(5758), pp. 208-212, (2006).
- [31] J. A. Rogers, T. Someya, and Y. Huang, “Materials and Mechanics for Stretchable Electronics”, *Science*, 327(5973), pp. 1603-1607, (2010).
- [32] D. Kim, J. Ahn, W. M. Choi, H. Kim, T. Kim, J. Song, and J. A. Rogers, “Stretchable and Foldable Silicon Integrated Circuits”, *Science*, 320(5875), pp. 507-511, (2008).
- [33] H. G. Allen, “Analysis and design of structural sandwich panels”, Pergamon Press, Ch. 8 (1969).
- [34] A. Auguste, J. Yang, L. Jin, D. Chen, Z. Suo, and R. C. Hayward, “Formation of high aspect ratio wrinkles and ridges on elastic bilayers with small thickness contrast”, *Soft Matter*, 14(42), pp. 8545-8551, (2018).
- [35] M. M. Hawkeye, M. T. Taschuk and M. J. Brett. “Handbook of Deposition Technologies for Films and Coatings”, Amsterdam: Elsevier, pp. 621-678, (2010).
- [36] A. Barranco, A. Borrás, A. R. Gonzalez-Elipe, and A. Palmero, “Perspectives on oblique angle deposition of thin films: From fundamentals to devices”, *Progress in Materials Science*, 76, pp. 59–61, (2016).
- [37] D. Antartis, R. Mott, and I. Chasiotis, “Silicon nanosprings fabricated by glancing angle deposition for ultra-compliant films and interfaces”, *Materials & Design*, 144, pp. 184, (2018).
- [38] D. Antartis, R. Mott, and I. Chasiotis, “Si nanospring films for compliant interfaces”, *Journal of Materials Science*, 53(8), pp. 5829, (2017).
- [39] D. Antartis, H. Wang, C.Y. Tang, H.B. Chew, S.J. Dillon, and I. Chasiotis, “Nanofibrillar Si Helices for Low-Stress, High-Capacity Li Anodes with Large Affine Deformations”, *ACS Applied Materials & Interfaces*, 11(12), pp. 11716, (2019).
- [40] S. Wang, G. Xia, H. He, K. Yi, J. Shao, and Z. Fan, “Structural and optical properties of nanostructured TiO<sub>2</sub> thin films fabricated by glancing angle deposition”, *Journal of Alloys and Compounds*, 431(1-2), pp. 291, (2017).
- [41] P. Pedrosa, C. Lopes, N. Martin, C., Fonseca, and F. Vaz, “Electrical characterization of Ag: TiN thin films produced by glancing angle deposition”, *Materials Letters*, 115, pp. 138, (2014).
- [42] B. Polat, and O. Keles, “Designing self-standing silicon-copper composite helices as anodes for lithium ion batteries”, *Journal of Alloys and Compounds*, 677, pp. 228-236, (2016).
- [43] M. O. Jensen, and M. J. Brett. “Periodically Structured Glancing Angle Deposition Thin Films.” *IEEE Transactions on Nanotechnology* IEEE Trans. Nanotechnology 4.2, pp. 269-277, (2005).

- [44] A. Yildiz, H. Cansizoglu, M. Turkoz, R. Abdulrahman, A., Al-Hilo, M. Cansizoglu, T. M. Demirkan, and T. Karabacak, "Glancing angle deposited Al-doped ZnO nanostructures with different structural and optical properties", *Thin Solid Films*, 589, pp. 764-769, (2015).
- [45] J. J Merkel, T. Sontheimer, B. Rech, and C. Becker, "Directional growth and crystallization of silicon thin films prepared by electron-beam evaporation on oblique and textured surfaces", *Journal of Crystal Growth* 367, pp. 126-130, (2013)
- [46] H. Liu, Y. Xu, X. Zhang, W. Zhao, A. Ming, and F. Wei, "Enhanced NO<sub>2</sub> sensing properties of Pt/WO<sub>3</sub> films grown by glancing angle deposition", *Ceramics International*, 46(13), pp. 21388-21394, (2020).
- [47] J. N. Broughton, and M. J. Brett, "Electrochemical Capacitance in Manganese Thin Films with Chevron Microstructure", *Electrochemical and Solid-State Letters*, 5(12), pp. 1-10, (2002).
- [48] R. Krishnan, T. Lu, and N. Koratkar, "Functionally Strain-Graded Nanoscoops for High Power Li-Ion Battery Anodes", *Nano Letters*, 11(2), pp. 377-384, (2011).
- [49] H. B. Chew, B. Hou, X. Wang, and S. Xia, "Cracking mechanisms in lithiated silicon thin film electrodes", *International Journal of Solids and Structures*, 51(23-24), pp. 4176-4187, (2014)
- [50] E. Jiménez-Piqué, L., González-García, V., Rico, and A. González-Elipe, "Nanoindentation of nanocolumnar TiO<sub>2</sub> thin films with single and stacked zig-zag layers", *Thin Solid Films*, 550, pp. 445, (2014).
- [51] R. Kaneko, T. Yukishita, T. Sumigawa, and T. Kitamura, "Nonlinear elasticity in a meta-film comprising nano-helices", *Thin Solid Films*, 695, pp. 137749-1-6, (2020).
- [52] A. Reinders, P. Verlinden, W. Sark, and A. Freundlich, "Photovoltaic Solar Energy: from fundamentals to applications", Chichester: Wiley, (2007).
- [53] K. J. Maung, H. T. Hahn, and Y. S. Ju, "Multifunctional integration of thin-film silicon solar cells on carbon-fiber-reinforced epoxy composites", *Solar Energy*. 84(3), pp. 450-458, (2010).
- [54] J. Gerdes, A. Holness, A. Perez-Rosado, L. Roberts, A. Greisinger, E. Barnett, J. Kempny, D. Lingam, C. H. Yeh, H. A. Bruck, and S. K. Gupta, "Robo Raven: a flapping-wing air vehicle with highly compliant and independently controlled wings", *Soft Robotics*, 1(4), pp. 275-288, (2014).
- [55] A. Perez-Rosado, H. A. Bruck, and S. K. Gupta, "Integrating solar cells into flapping wing air vehicles for enhanced flight endurance", *Journal of Mechanisms and Robotics*. 8(5), pp. 051006-1-11, (2016).
- [56] Y. Dai, Y. Huang, X. He, D. Hui, and Y. Bai, "Continuous performance assessment of thin-film flexible photovoltaic cells under mechanical loading for building integration", *Solar Energy*. 183, pp. 96-104, (2019).
- [57] G. Dennler, S. Bereznev, D. Fichou, K. Holl, D. Ilic, R. Koeppel, and T. Wöhrle, "A self-rechargeable and flexible polymer solar battery", *Solar Energy*. 81(8), pp. 947-957, (2007).

- [58] A. Chen, and A. Alateeq, “Performance of solar cells integrated with rigid and flexible building substrates under compression”, *Journal of Building Engineering*, 34, pp.101938-1-11, (2021).
- [59] D. Antartis, and I. Chasiotis, “Residual stress and mechanical property measurements in amorphous Si photovoltaic thin films”, *Solar Energy*. 105, pp. 694-704, (2014).
- [60] J. C. Kim, and S. K. Cheong, “I–V curve characteristics of solar cells on composite substrate under mechanical loading”, *Journal of Mechanical Science and Technology*. 28(5), pp. 1691-1696, (2014).
- [61] R. Jones, T. Johnson, W. Jordan, S. Wagner, J. Yang, and S. Guha, “Effects of mechanical strain on the performance of amorphous silicon triple-junction solar cells”, *Conference Record of the Twenty-Ninth IEEE Photovoltaic Specialists Conference*, pp. 1214-1217, (2002).
- [62] J. Park, V. A. Dao, S. Kim, D. P. Pham, S. Kim, A. H. Le, J. Kang, and J. Yi, “High Efficiency Inorganic/Inorganic Amorphous Silicon/Heterojunction Silicon Tandem Solar Cells”, *Scientific Reports*. 8(1), pp. 1-11, (2018).
- [63] Y. Xu, Z. Hu, H. Diao, Y. Cai, S. Zhang, X. Zeng, H. Hao, X. Liao, E. Fortunato, and R. Martins, “Heterojunction solar cells with n-type nanocrystalline silicon emitters on p-type c-Si wafers”, *Journal of Non-Crystalline Solids*, 352(9-20), pp. 1972-1975, (2006),
- [64] Y. Dai, Y. Bai, and T. Keller, “Stress mitigation for adhesively bonded photovoltaics with fibre reinforced polymer composites in load carrying applications”, *Composites Part B: Engineering*, 177, pp.107420-1-9, (2019).
- [65] S. P. Lacour, S. Wagner, R. J. Narayan, T. Li, and Z. Suo, “Stiff subcircuit islands of diamond-like carbon for stretchable electronics”, *Journal of Applied Physics*, 100(1), pp. 014913-1-6, (2006).
- [66] J. Sun, N. Lu, J. Yoon, K. Oh, Z. Suo, and J. J. Vlassak, “Inorganic islands on a highly stretchable polyimide substrate”, *Journal of Materials Research*, 24(11), pp. 3338-3342, (2009).
- [67] N. Lu, J. Yoon, and Z. Suo, “Delamination of stiff islands patterned on stretchable substrates”, *International Journal of Materials Research*, 98(8), pp. 717-722, (2007).
- [68] G. Lubin, “*Handbook of composites*”, New York: Van Nostrand Reinhold, (1982).
- [69] T. Tong, Y. Zhao, L. Delzeit, A. Kashani, M. Meyyappan, and A. Majumdar, “Dense Vertically Aligned Multiwalled Carbon Nanotube Arrays as Thermal Interface Materials”, *IEEE Transactions on Components and Packaging Technologies*, 30(1), pp. 92-100, (2007).
- [70] L. Qu, L. Dai, M. Stone, Z. Xia, and Z. L. Wang, “Carbon Nanotube Arrays with Strong Shear Binding-On and Easy Normal Lifting-Off”, *Science*, 322(5899), pp. 238-242, (2008).
- [71] X. Zhao, M. Ohkohchi, M., Wang, S. Iijima, T. Ichihashi, and Y. Ando, “Preparation of high-grade carbon nanotubes by hydrogen arc discharge”, *Carbon*, 35(6), pp. 775-781, (1997).

- [72] K. A. Shah, and B. A. Tali, "Synthesis of carbon nanotubes by catalytic chemical vapour deposition: A review on carbon sources, catalysts and substrates", *Materials Science in Semiconductor Processing*, 41, pp. 67-82, (2016).
- [73] C. Daraio, V. F. Nesterenko, S. Jin, W. Wang, and A. M. Rao, "Impact response by a foamlike forest of coiled carbon nanotubes", *Journal of Applied Physics*, 100(6), pp. 064309-1-4, (2006).
- [74] C. H. See, and A. T. Harris, "A Review of Carbon Nanotube Synthesis via Fluidized-Bed Chemical Vapor Deposition", *Industrial & Engineering Chemistry Research*, 46(4), pp. 997-1012, (2007).
- [75] A. J. Hart, and A. H. Slocum, "Rapid Growth and Flow-Mediated Nucleation of Millimeter-Scale Aligned Carbon Nanotube Structures from a Thin-Film Catalyst", *The Journal of Physical Chemistry B*, 110(16), pp. 8250-8257, (2006).
- [76] G. D. Nessim, M. Seita, K. P. O'Brien, A. J. Hart, R. K. Bonaparte, R. R. Mitchell, and C. V. Thompson, "Low Temperature Synthesis of Vertically Aligned Carbon Nanotubes with Electrical Contact to Metallic Substrates Enabled by Thermal Decomposition of the Carbon Feedstock", *Nano Letters*, 9(10), pp. 3398-3405, (2009).
- [77] E. Lejeune, A. Javili, and C. Linder, "An algorithmic approach to multi-layer wrinkling", *Extreme Mechanics Letters*, 7, pp. 10-17, (2016).
- [78] L. Li, R. Li, S. Wang, Z. Wang, T. Ling, and C. Li, "Stress analysis of film-on-substrate structure under tensile loads", *Mechanics of Materials*, 120, pp. 1-14, (2018).
- [79] L. Wang, B. Sun, K. S. Ziemer, G. A. Barabino, and R. L. Carrier, "Chemical and physical modifications to poly(dimethylsiloxane) surfaces affect adhesion of Caco-2 cells", *Journal of Biomedical Materials Research Part A*, 9999A, pp. 1264, (2009).
- [80] R. Seghir, and S. Arscott, "Extended PDMS stiffness range for flexible systems", *Sensors and Actuators A: Physical*, 230, pp. 38, (2015).
- [81] K. Sivaramakrishnan, and T. L. Alford, "Metallic conductivity and the role of copper in ZnO/Cu/ZnO thin films for flexible electronics", *Applied Physics Letters*, 94(5), pp. 052104-1-3, (2009).
- [82] S. Lee, H. Guim, D. Kim, Y. Joo, C. Shim, J. Ahn, I. Choi, and M. Abbasi, "Transmission orientation imaging of copper thin films on polyimide substrates intended for flexible electronics," *Scripta Materialia*, 138, pp. 52-56, (2017).
- [83] R. Qin, M. Hu, N. Zhang, Z. Guo, Z. Yan, J. Li, J. Liu, G. Shan, and J. Yang, "Flexible Fabrication of Flexible Electronics: A General Laser Ablation Strategy for Robust Large-Area Copper-Based Electronics", *Advanced Electronic Materials*, 5(10), 1900365-1-10, (2019).
- [84] Z. Li, S. Khuje, A. Chivate, Y. Huang, Y. Hu, L. An, Z. Shao, J. Wang, S. Chang, and S. Ren, "Printable Copper Sensor Electronics for High Temperature", *ACS Applied Electronic Materials*, 2(7), pp. 1867-1873, (2020).
- [85] S. A. Campbell, "Fabrication Engineering at the Micro and Nanoscale". New York: Oxford UP, pp.321-355, (2008).

- [86] [https://www.lesker.com/newweb/deposition\\_materials/materialdepositionchart.cfm](https://www.lesker.com/newweb/deposition_materials/materialdepositionchart.cfm) (accessed on November 25, 2021.)
- [87] J. L. Vossen, and K. Werner, "Thin Film Processes II". Boston: Academic, pp. 177-204, (1991).
- [88] B. Dick, M. J. Brett, and T. Smy, "Controlled Growth of Periodic Pillars by Glancing Angle Deposition," *J. Vac. Sci. Technol. B Journal of Vacuum Science & Technology B: Microelectronics and Nanometer Structures* 21.1, pp. 26, (2003).
- [89] T. Sumigawa, H. Tanie, A. Sakurai, K. Iwata, S. Chen, and T. Kitamura, "Substrate Temperature Control for the Formation of Metal Nanohelices by Glancing Angle Deposition", *Journal of Vacuum Science & Technology A: Vacuum, Surfaces, and Films*, vol. 33, no. 6, pp. 060609-1-5, (2015).
- [90] J. M. Nieuwenhuizen, and H. B. Haanstra, "Microfractography of thin films", *Philips Technical Review*, 27, pp. 89, (1966).
- [91] R. Tait, T. Smy, and M. Brett, "Modelling and characterization of columnar growth in evaporated films", *Thin Solid Films*, 226(2), pp. 198, (1993).
- [92] J. Lintymer, J. Gavaille, N., Martin, and J. Takadoum, J. "Glancing angle deposition to modify microstructure and properties of sputter deposited chromium thin films", *Surface and Coatings Technology*, 174-175, pp. 316, (2003).
- [93] M. Morgan, G. Jakovidis, and I. Mcleod, 1994. An experiment to measure the I-V characteristics of a silicon solar cell, *Physics Education*, vol. 29, no. 4, 252–254.
- [94] A. M. Wahl, *Mechanical Springs*, 2nd edition, McGraw-Hill, (1963).
- [95] C. J. Ancker and JN Goodier, "Pitch and curvature corrections for helical springs", *Journal of Applied Mechanics*, 1958, 466-470.
- [96] S. Timoshenko, and S. Woinowsky-Krieger, "Theory of Plates and Shells, 2nd edition", McGraw-Hill, pp. 418, (1959).
- [97] M. A. Biot, and M. Cambridge, "Bending of an infinite beam on an elastic foundation", *Journal of Applied Mechanics for March*, 203, pp. 1-7, (1936).
- [98] E. Lejeune, A. Javili, J. Weickenmeier, E. Kuhl, and C. Linder, "Tri-layer wrinkling as a mechanism for anchoring center initiation in the developing cerebellum", *Soft Matter*, 12(25), pp. 5613-5620, (2016).
- [99] J. M. Gere, James Monroe, and B. J. Goodno, "Mechanics of Materials", Cengage Learning, (2018).
- [100] L. A. Carlsson, and G. A. Kardomateas, "Structural and Failure Mechanics of Sandwich Composites", Springer, pp. 365, (2011).
- [101] H. M. Ledbetter, and E. R. Naimon, "Elastic Properties of Metals and Alloys. II", *Copper. Journal of Physical and Chemical Reference Data*, 3(4), pp. 897-935, (1974).
- [102] G. V. Samsonov, "Handbook of the physicochemical properties of the elements", Springer-Verlag US 1968, pp. 392, (1968).

- [103] A. Müller, M. Wapler, and U. Wallrabe, “A quick and accurate method to determine the Poissons ratio and the coefficient of thermal expansion of PDMS”, *Soft Matter*, 15(4), pp. 779-784, (2019).
- [104] R. H. Pritchard, P., Lava, D. Debruyne, and E. M. Terentjev, “Precise determination of the Poisson ratio in soft materials with 2D digital image correlation”, *Soft Matter*, 9(26), pp. 6037-6045, (2013).
- [105] Z. Zhou, Y. Zhou, C. Yang, J. Chen, W. Ding, and G. Ding, “The evaluation of Youngs modulus and residual stress of copper films by microbridge testing”, *Sensors and Actuators A: Physical*, 127(2), pp. 392-397, (2006).
- [106] <https://www.prepregs.com/da-409ug35-150> (accessed on November 27, 2021.)
- [107] N. Evans, C. Minelli, E. Gentleman, V. Lapointe, S. Patankar, M. Kallivretaki, X. Chen, C. J. Robert, and M. Stevens, “Substrate stiffness affects early differentiation events in embryonic stem cells”, *European Cells and Materials*, 18, pp. 1-14, (2009).
- [108] X. Q. Brown, K. Ookawa, and J.Y. Wong, “Evaluation of polydimethylsiloxane scaffolds with physiologically-relevant elastic moduli: interplay of substrate mechanics and surface chemistry effects on vascular smooth muscle cell response”, *Biomaterials*, 26(16), pp. 3123-3129, (2005).
- [109] F. Schneider, J. Draheim, R. Kamberger, and U. Wallrabe, “Process and material properties of polydimethylsiloxane (PDMS) for Optical MEMS”, *Sensors and Actuators A: Physical*, 151(2), pp. 95-99, (2009).
- [110] M. Murrell, R. Kamm, and P. Matsudaira, “Substrate Viscosity Enhances Correlation in Epithelial Sheet Movement”, *Biophysical Journal*, 101(2), pp. 297-306, (2011).
- [111] H. Gleskova, I. C. Cheng, S. Wagner, J. C. Sturm, and Z. Suo, “Mechanics of thin-film transistors and solar cells on flexible substrates”, *Solar Energy*, 80(6), pp.687-693, (2006).
- [112] <https://www.jeol.co.jp/en/products/detail/JBX-6300FS.html> (accessed on November 27, 2021.)
- [113] J. Y. Chung, A. J. Nolte, and C. M. Stafford, “Surface Wrinkling: A Versatile Platform for Measuring Thin-Film Properties”, *Advanced Materials*, 23(3), pp. 349-368, (2010).
- [114] B. A. Jayne, and M. O. Huny, “Plane stress and plane strain in orthotropic and anisotropic media”, *Wood and Fiber*, V.1, n.2, pp. 236-247, (1969).
- [115] [https://www.rockwestcomposites.com/media/wysiwyg/Hyosung\\_H2550-12K\\_Data.pdf](https://www.rockwestcomposites.com/media/wysiwyg/Hyosung_H2550-12K_Data.pdf) (accessed on November 27, 2021.)
- [116] <https://tcrcomposites.com/lib/TDS-RD-0010-R012-TDS-RD-0010-R012-UF3376.pdf> (accessed on November 27, 2021.)
- [117] H. Miyagawa, C. Sato, T. Mase, E. Drown, L. T. Drzal, and K. Ikegami, “Transverse elastic modulus of carbon fibers measured by Raman spectroscopy”, *Materials Science and Engineering: A*, 412(1-2), pp. 88-92, (2005).